UNIVERSITY OF OKLAHOMA

GRADUATE COLLEGE

OBSERVATIONAL EVIDENCE OF TROPICAL CYCLONE VORTEX ROSSBY WAVES AND THEIR ROLE IN INNER CORE RAINBANDS

A THESIS

SUBMITTED TO THE GRADUATE FACULTY

in partial fulfillment of the requirements for the

Degree of

MASTER OF SCIENCE IN METEOROLOGY

By

AUSTIN ADDISON ALFORD
Norman, Oklahoma
2016

Downloaded from SHAREOK. Persistent Handle URL: https://hdl.handle.net/11244/45035

OBSERVATIONAL EVIDENCE OF TROPICAL CYCLONE VORTEX ROSSBY WAVES AND THEIR ROLE IN INNER CORE RAINBANDS

A THESIS APPROVED FOR THE
SCHOOL OF METEOROLOGY

BY

_____
Dr. Michael Biggerstaff, Chair

_____
Dr. Lance Leslie

_____
Dr. Xugaung Wang

© Copyright by AUSTIN ADDISON ALFORD 2016
All Rights Reserved.

Acknowledgements

First and foremost, I would like to thank my advisor, Dr. Mike Biggerstaff, for his guidance, support, and friendship from my undergraduate career, through my graduate studies, and onward into my continued research. The countless hours spent in deep discussions regarding meteorology, field work, the future of our field, and personal matters have made me a better researcher, a better scientist, and a better person.

I would also like to thank my committee members, Dr. Xuguang Wang and Dr. Lance Leslie, for their continued discussion and encouragement regarding this project. In addition, I offer my sincere gratitude to my friend and fellow student, Daniel Betten, for his countless hours spent aiding in the preparation of the software that made this study possible and for his advice throughout my undergraduate and graduate careers. Also, many thanks to my coworker and friend, Gordon Carrie, for his assistance with the computing resources necessary to finish this work. I would also like to acknowledge my friend and colleague, Corey Simma, for his aid in the preparation of the dataset collected during Hurricane Irene, as well as all of those (too numerous to mention) who aided in collecting data during Hurricanes Isabel, Frances, and Irene.

Finally, I must thank my friends and family for their love and support throughout my life. None of this work would have been possible without the love and encouragement of my mother and father. Mom and Dad have always supported my love of science and nature and have given me everything to make my ambitions a reality. In addition, I am forever grateful to my lifelong mentor and friend, Miss Sarah Belle Day, for her advice, teaching, and kindness throughout my life. My colleague and friend, Mr.

Samuel Williamson, was also instrumental in my placement at the University of Oklahoma and encouraged and mentored me throughout my studies. Finally, my friends Andy Wade, Heather Wade, Andrew Rickels, Kristen Perez-Rickels, Rachel Miller, Kate-Lynn Walsh, Liz DiGangi, Zack Zounes, Wesley Howell, Shelby Reeves, Madeline Shelton, Kyle Thiem, Pat Hyland, and Stacey Hitchcock have always supported me and have made my time at the University of Oklahoma a great and unforgettable pleasure.

Table of Contents

Acknowledgements iv

List of Tables viii

List of Figures ix

Abstract xv

Chapter 1: Introduction 1

Chapter 2: Background 4

2.1 Vortex Rossby Waves 4

2.2 Gravity Waves and Advection 9

Chapter 3: SMART Radar Data 10

3.1 SMART Radar Overview 10

3.2 SMART Radar Deployments 11

3.3 Analysis Technique 11

Chapter 4: Hurricane Overviews 13

4.1 Hurricane Isabel (2003) 13

4.2 Hurricane Frances (2004) 14

4.3 Hurricane Irene (2011) 15

Chapter 5: Dual-Doppler Analysis Results 16

5.1 Hurricane Isabel 16

5.1.1 Mesoscale Context 16

5.1.2 Kinematic Structure 18

5.1.3 Rainband Comparison to Theory 24

5.2 Hurricane Frances 26

5.2.1 Mesoscale Context 26
5.2.2 Kinematic Structure 26
5.3 Hurricane Irene 28
5.3.1 Mesoscale Context 28
5.3.2 Kinematic Structure 29
Chapter 6: Rainfall from Rainbands 32
6.1 Inner Core Rainfall 32
6.2 Precipitation Classification 33
Chapter 7: Discussion and Conclusions 35
7.1 Rainband Kinematics 35
7.2 Inner Core Precipitation 38
7.3 Conceptual Models 40
7.4 Future Work 43
References 82

List of Tables

Table 1. SMART radar details are listed below including the frequency, antenna diameter, half-power beam width, peak power, and moments collected. 45

Table 2. SMART radar and WSR-88D scan strategy details in Hurricanes Isabel, Frances, and Irene. The strategy name is listed with a hurricane descriptor (Isabel = IS, Frances = FR, and Irene = IR), a volume type (360° Volume = 360, Sector Volume = Sector), and a radar (SMART radar 1 or 2 = S, WSR-88D = W). Elevation angles are listed with elevations in parentheses indicating those that were different in the SMART radar 2 scanning strategy. Finally, the effective Nyquist Velocity and gate spacing are listed for each strategy. WSR-88D Nyquist velocities are listed for the lowest elevation only. 46

Table 3. Dual-Doppler domain details and radar pairs used in each hurricane case. The radar used as the origin of the domain is listed under "Radar 1" with the other radar listed under "Radar 2." In addition, the grid specifications including size and shape are listed. Finally, the baseline distance between the dual-Doppler pairs is listed. 47

List of Figures

Fig. 1. Dual-Doppler domains for each SMART radar deployment. The hatched white area in each figure represents the 30° lobe. Radar positions are labeled in red. Dual-Doppler pairs include SMART radars 1 and 2 during Hurricane Isabel (a), SMART radar 2 and KMLB during Hurricane Frances (b), and SMART radar 2 and KMHX during Hurricane Irene (c). 48

Fig. 2. Time series of KMHX 0.5° Z_H during Hurricane Isabel. The filled contours represent radar reflectivity in dBZ, the solid black line represents the 30° dual-Doppler lobes, and locations of SMART radars 1 and 2 are indicated by the blue dots. KMHX is located at the origin. The arrows identify a rainband's origin near the eyewall, propagating outward into the inner core..... 49

Fig. 3. As in Fig. 2, but for the landfall of Hurricane Frances. The radar at the origin is KMLB..... 50

Fig. 4. As in Fig. 3, but for the landfall of Hurricane Irene. The radar centered at the origin is KMHX..... 51

Fig. 5. Plan view of Z_H from KMHX (located at the origin). The black lines are as in Fig. 2 with the locations of the SMART radars indicated by the blue points labeled "SR1" and "SR2." 52

Fig. 6. Shear magnitude (colored contours) and direction (arrows), showing the 4 day mean 200-850 hPa shear beginning six days prior to hurricane landfall through two days prior to landfall. Plots are shown individually for Hurricanes Isabel (a), Frances (b), and Irene (c)..... 53

Fig. 7. Vertical cross section through the 1456 UTC dual-Doppler analysis of Hurricane Isabel. (a) Reflectivity is color contoured and the blue line labeled “A” and “B” at both ends represents the region through which the vertical cross section in (b) is taken. (b) Reflectivity is contoured along the cross section and height plane. Vertical velocity is contoured every 1 m s^{-1} with the 0 m s^{-1} represented by the first solid contour. Positive values are solid lines and negative values are dashed. 54

Fig. 8. Fourier decomposition of Z_H. (a) The total reflectivity is color contoured with sum of WN1 and WN2 components overlaid every 2 dB beginning with 20 dBZ. (b) The symmetric component of Z_H (WN0) is shown. (c) The sum of the WN1 and WN2 components of Z_H is displayed. (d) As in (c), but for the sum of WN3 and WN4 components. (e) As in (c), but for the WN5 through WN10 components. (f) As in (c), but for the WN11-WN20 components. 55

Fig. 9. Dual-Doppler analyses between 1440 UTC and 1500 UTC. Individual analysis times are shown above each plot. The filled contours represent the maximum radar reflectivity at the z = 3.5 km ARL analysis level. The black contours represent vertical velocity w every 0.5 m s^{-1}. The dashed contours represent $w <$ 0 m s^{-1}, and the solid contours represent $w \geq 0$ m s^{-1}..... 56

Fig. 10. As in Fig. 9, but the black contours are ζ’ every 4 $\times 10^{-4}$ s^{-1}. In this figure, the 0 s^{-1} line is omitted. 57

Fig. 11. As in Fig. 10, but for the 1.5 km ARL analysis level..... 58

Fig. 12. As in Fig. 9, but for the 1.5 km ARL analysis level. 59

Fig. 13. The vertical cross section indicated by the line L1-L2 in (a) is shown for the 1442 UTC DDA. (a) Z_H is contoured at the 1.5 km ARL level with the blue line indicating the position of the vertical cross section. (b) Reflectivity is contoured in the vertical cross section, and contours (black) of vertical velocity are shown every 1 m s^{-1} with the first solid line being 0 m s^{-1}. (c) As in (b), but the filled contours display vertical vorticity ζ. (d) As in (c), but the filled contours indicate the magnitude of horizontal divergence δ_{2D}. 60

Fig. 14. As in Fig. 13, but for the 1452 UTC DDA through the line L3-L4. 61

Fig. 15. Shown is a diagram similar to a Hovmoller diagram, except time is increasing in the positive y-direction. The filled contours represent the mean vertical vorticity in azimuth as a function of radius from the center of circulation. The dashed lines represent a hypothetical phase speed of 1.5 m s^{-1}. 62

Fig. 16. Shown is an azimuth-time plot of vertical vorticity at a radius of 118 km from the center of Hurricane Isabel. The filled contours represent the azimuthal vorticity averaged over a 5 km radial window. The dashed line is the mean tangential wind of 36 m s^{-1} at the 118 km radius. The tangential wind is derived from the radial composite tangential winds generated from the DDAs performed in the inner core. 63

Fig. 17. As in Fig. 5, but for the inner core of Hurricane Frances with KMLB at the center of the domain. 64

Fig. 18. As in Fig. 13, but for 1316 UTC analysis of Hurricane Frances through the line L5-L6. 65

Fig. 19. As in Fig. 5, but for the landfall of Hurricane Irene. The center of the domain is KMHX. 66

Fig. 20. As in Fig. 10, but for the 0936-1045 UTC DDAs in Hurricane Irene. 67

Fig. 21. As in Fig. 13, but for the 1016 UTC DDA in Hurricane Irene. 68

Fig. 22. As in Fig. 13, but for 1116 UTC analysis of Hurricane Irene through the line L9-L10. 69

Fig. 23. As in Fig. 13, but for 1116 UTC analysis of Hurricane Irene through the line L11-L12. 70

Fig. 24. CFAD courtesy of Houze (2010; see his Fig. 32b). 71

Fig. 25. (a) Radar reflecitivity from SMART radar 2 is gridded in dBZ at 1036 UTC during Hurricane Irene at z=0.5 km. (b) Rain rate (mm hr^{-1}) is derived using a Z-R relation of $Z_h = 250R^{1.2}$. 72

Fig. 26. Contoured frequency altitude diagrams for (a) Hurricane Isabel, (b) Hurricane Frances, (c) Hurricane Irene, and (d) a composite of all three cases. The filled contours represent the frequency of data per reflectivity bin (1 dBZ) per kilometer. So, the frequency can be read as 0.01 (or 1%) dBZ^{-1} km^{-1}. 73

Fig. 27. Results of the stratiform-convective classification algorithm in the inner core of Hurricane Isabel at 1447 UTC. (a) Z_H is displayed at the 1.50 km altitude. (b) The echo classification is displayed with brown conveying convective echoes, tan showing stratiform echoes, and blue indicating an unknown classification. 74

Fig. 28. As in Fig. 27, but for the 1252 UTC analysis of Hurricane Frances. 75

Fig. 29. As in Fig. 27, but for the 1006 UTC analysis of Hurricane Irene. 76

Fig. 30. An example of the vertical profile of vertical velocity in convective and non-convective echoes prior to the reclassification of the inner core to all convective echoes is shown for the 1026 UTC DDA of Hurricane Irene. (a) Z_H is contoured and filled in 5 dBZ increments and the echoes that were classified as stratiform are contoured in black. (b) The mean vertical velocity of convective and stratiform (i.e. non-convective) echoes is shown. 77

Fig. 31. Shown is a vertical velocity profile taken within a rainband [in red box in (a)] in the DDA at 1456 UTC in Hurricane Isabel. (a) Reflectivity is shaded every 5 dBZ with vertical velocity contoured every 2 m s^{-1}. The red box shows the area in which the vertical velocity statistics are calculated (b). (b) Mean vertical velocity is shown in the black line with height (y-axis) with one standard deviation indicated by the error bars. The green line indicates 0 m s^{-1}. 77

Fig. 32. As in Fig. 31, but for a non-rainband region of the 1456 UTC analysis. The red box in (a) indicates region over which the statistics in (b) are calculated. 78

Fig. 33. As in Fig. 8, but (c) is WN1 only, (d) is WN2 only, (e) is WN3-WN4, and (f) is WN5-WN10. 79

Fig. 34. Fig. 9 of (Marks and Houze 1987), showing a conceptual model the inner core stratiform structure of a mature TC. 80

Fig. 35. A conceptual model of the inner core of a TC generated from observations presented herein. The dark grey annulus represents the eyewall, the blue structures represent VRWs beginning in the eyewall, extending radially outward into the inner core, and the red structures are the rising motion associated with the VRW. In the cross section through the VRW, radar reflectivity is shaded at

intervals of 10 dBZ (blue), 20 dBZ (green), 35 dBZ (yellow), and 45 dBZ (orange). The VRWs are represented by the pink, translucent shading. The hollow black arrows show the rainband-relative flow. In addition, likely hydrometeor paths are indicated, showing the generation of particles in the convective updrafts and droplet fallout in the deep subsidence between the rainbands..... 81

Abstract

Vortex Rossby Waves (VRWs) are hypothesized to exist in tropical cyclones (TCs), acting as an axisymmetrizing mechanism to the inner core TC flow and restored by the radial gradient of storm vorticity. In addition, they have been hypothesized to be a leading mechanism of inner core spiral rainband formation and a mechanism by which the symmetric flow may be enhanced. The majority of the knowledge of VRWs comes from numerical modeling. Only two observational studies performed at coarse temporal and spatial resolutions have previously been published. Since VRWs may influence the structure of the inner core of TCs, additional observations are essential to their understanding.

The Shared Mobile Atmospheric Research and Teaching (SMART) radars have sampled multiple landfalling TCs in the United States including Hurricanes Isabel (2003), Frances (2004), and Irene (2011), among others. The data collected over the inner core environments of these three TCs provided the opportunity to examine the inner core structure of TCs outside of the eyewall, including VRW-induced spiral rainbands. Three-dimensional radar wind retrievals indicate that the structure of spiral rainbands was similar to that of numerically simulated VRWs. In Hurricane Isabel, which was particularly well sampled, the measured azimuthal and radial phase speeds were compared to that of VRW theory and were found to be consistent with the theoretical phase speeds.

While other mechanisms may produce rainband-like features, the rainbands observed by the SMART radars in three TCs were induced by VRWs. Moreover, the VRW-induced bands were key in producing a significant portion of rainfall within the

inner core of TCs. Thus, the current stratiform conceptual model of the inner core does not adequately identify the roles of VRWs. A new conceptual model of the inner core and its associated rainbands is presented to reflect these new observations of the inner core.

Chapter 1: Introduction

Landfalling tropical cyclones (TCs) are known to take a majority of lives through storm surge and inland flooding and can cause immense devastation to property through strong winds, floods, and storm surge (Rappaport 2014). In recent years, the shortcomings of TC forecasting and modeling has been emphasized (Cavallo et al. 2012) specifically relating poor TC intensity forecasts to a lack of high-resolution observations of the inner core environment of TCs (Hogsett and Zhang 2009). Thus, the energy cascade between physical scales of motion is poorly understood (Rogers et al. 2012; Montgomery and Smith 2016).

Rogers et al. (2012) noted that there is strong variance of vertical velocities and subsequent mass transport in the region radially outward of the positive vertical mass flux of the eyewall. This variance is indicative of rainbands within an otherwise stratiform region of precipitation, and is often referred to as the inner core region (e.g. Didlake and Houze 2013). Generally, the inner core is an annulus with an outer radial extent three times that of the RMW and the inner edge at the RMW (Montgomery et al. 1997; hereafter, MK97). Within this region, rainbands of radial wavelengths on the order of 10 km exist, surrounded by stratiform precipitation; however, their generation mechanism is unknown (Houze 2010). Three dominant hypotheses of inner core spiral rainband formation include: inertia-gravity waves (e.g. Anthes 1972; Willoughby 1977; Chow et al. 2002), vortex Rossby waves (hereafter, VRWs; e.g. MK97; McWilliams et al. 2003), and non-linear advection (e.g. Moon and Nolan 2015). It is generally thought that inertia-gravity waves remove momentum from the symmetric component of the TC vortex, weakening the overall intensity, but at a negligible rate according to Moon and

Nolan (2010). However, VRW theory indicates that the inward transport of angular momentum by VRWs can intensify a TC (e.g. Carr and Williams 1989; MK97; Franklin et al. 2006; Menelaou and Yau 2014). Only one study has shown weakening of a TC by VRW-mean flow interactions (Wang 2002a). However, Moon and Nolan (2015) indicated that rainbands result from the advection of convective clouds and hydrometeors by the tangential winds of a TC that resulted in spiral band-like shapes. The effect of these bands on TC structure and intensity was not examined in their study.

In addition to the intensity feedbacks inner core spiral rainbands may yield, their contribution to rainfall is also in question. For example, in a numerical modeling study of Typhoon Morakat (2009), Hall et al. (2013) showed that VRW-induced inner core spiral rainbands interacted with orography such that they produced extreme rainfall over Taiwan. While the study concluded that the extreme rainfall totals were a result of orographic enhancement, azimuthal wavenumber (WN) 1, 2, and 3 VRWs were the initial mechanism for convective rainfall within the inner core. Ignoring the mechanism for spiral rainband formation, the results of Hall et al. (2013) demonstrate that inner core spiral rainbands can contribute significantly to total rainfall within the inner core. In a summary of TC clouds, Houze (2010) notes that the inner core region of TCs is generally considered stratiform with the primary source of rainfall being produced by the ejection of ice crystals from the deep convection of the eyewall. The radial advection of ice crystals into the inner core region gives the inner core region the stratiform characteristics similar to that of the stratiform region of a mature mesoscale convective system (Biggerstaff and Houze 1991). In other words, the inner core region is seeded by the deep convection of the eyewall. However, the result of Hall et al.

(2013) suggests convection of inner core spiral rainbands may result in significant precipitation within the inner core.

Herein, the mechanism for inner core rainbands is examined utilizing high-resolution observations from the ground-based Shared Mobile Atmospheric Research and Teaching (SMART) radars (Biggerstaff et al. 2005) and the Weather Surveillance Radars-1988 Doppler (hereafter, WSR-88Ds; Crum and Alberty 1993; Doviak et al. 2000). Observations of the kinematic structure of inner core spiral rainbands (hereafter referred to as rainbands) are presented. As this study will focus on radar analyses outside of the eyewall, the feedback of rainbands to the intensity of TCs cannot be explicitly examined. Nevertheless, the generation mechanism for spiral rainbands observed by the SMART radars and the WSR-88Ds were elucidated. In addition, the contribution of rainbands to the inner core precipitation structure was evaluated. Utilizing observations collected during Hurricane Isabel (2003), Hurricane Frances (2004), and Hurricane Irene (2011), it will be shown that the rainbands observed by the SMART radars and the WSR-88Ds are most similar to that of VRWs. In addition, the observations VRW-induced rainbands indicate that rainbands contribute a significant portion of inner core rainfall as a result of deep convection within the inner core, a deviation of the stratiform conceptual model of the inner core region. As a result of these observations, a new conceptual model of the inner core is developed.

This work is organized as follows: Chapter 2 will summarize previous modeling and observational works of spiral rainbands. Chapter 3 overviews the observational dataset used in this study with an explanation of quality control methods and the analysis techniques utilized. Chapter 4 will present summaries of the TCs examined

herein. Chapter 5 presents the results of dual-Doppler analyses performed within the TCs examined. Chapter 6 will show the results of the rainfall analysis of the inner core region. Finally, Chapter 7 discusses the results of Chapters 5 and 6, their implications to current TC conceptual models, and draw conclusions based on the analyses presented.

Chapter 2: Background

2.1 Vortex Rossby Waves

First mentioned by MacDonald (1968) and Guinn and Schubert (1993), Rossby-type waves were through to be active in TCs and be associated with rainbands. Macdonald (1968) attributed the upwind propagation of rainbands against the mean tangential flow in TCs to Rossby wave-like dynamics, similar to that of a planetary Rossby wave. He also noted the outward radial propagation of the waves, but did not quantify the speed at which the bands moved radially outward. Extending the suggestion made by MacDonald (1968), Guinn and Schubert (1993) hypothesized that the well-established radial potential vorticity (PV) gradient in TCs could act as a waveguide and support the existence of Rossby waves in TCs. The modeling experiments performed by Guinn and Schubert revealed that an asymmetric PV core of a hypothetical TC could yield elongated PV structures that move outward from their asymmetric sources near the eyewall. They concluded these structures could be associated with inner core convective rainbands. However, it was not until MK97 that the term "vortex Rossby wave" was coined. Utilizing a Wenzel-Kramers-Brillouin analysis, MK97 showed that VRWs could exist arising from asymmetries in an asymmetric, barotropic vortex. The expulsion of high PV air radially outward from the

PV core was shown to be an axisymmetrizing mechanism of the TC vortex. The VRWs also tended to cease their radial propagation near a stagnation radius (approximately 2-3 times the RMW) due to the reduction of the radial PV gradient upon which the VRWs had been propagating. Furthermore, MK97 derived a dispersion relation (Equation 1) for VRWs, suggesting that the outward radial propagation (radial phase speed) of VRWs is on the order of 2-4 m s^{-1} and the azimuthal propagation of VRWs is slower than that of the mean flow of a TC. In Eqn. 1, n is the azimuthal wavenumber, Ω is the angular velocity at radius R, ξ is the inertia parameter (Eqn. 2; f is the Coriolis parameter), dq/dR is the radial gradient of the potential vorticity q (Eqn. 3; Φ is the geopotential of the analysis level) at radius R (see Eqn. 4; v is the tangential wind), and k is the time-dependent radial wavenumber (Eqn. 5) based on the initial radial wavenumber k_0 and with t being time.

$$\omega = n\Omega + \frac{n\xi \dfrac{dq}{dR}}{Rq\left(k^2 + \dfrac{n^2}{R^2} + \gamma^2\right)} \qquad (1)$$

$$\xi = f + 2\Omega \qquad (2)$$

$$q = \eta / \Phi \qquad (3)$$

$$\eta = f + \frac{1}{R}\frac{d\left(Rv\right)}{dR} \qquad (4)$$

$$k = k_o + nt\frac{d\Omega}{dR} \qquad (5)$$

MK97 concluded that VRWs are likely associated with the outward propagating spiral rainbands of the inner core. The work of MK97 was later generalized by McWilliams et al. (2003) for a vortex in gradient wind balance.

Since MK97, numerous modeling studies have focused on VRWs and their associated spiral rainbands (Chen and Yau 2001; Wang 2002a,b; Braun et al. 2006; Franklin et al. 2006; Wang 2008; Wei et al. 2010; Li and Wang 2012; Wang et al. 2012; Hall et al. 2013; Menelaou and Yau 2014; Moon and Nolan 2015). The radial kinematic structure of VRWs was hypothesized in several of these studies. For example, Chen and Yau (2001) examined inner core rainbands in a full physics simulation of an idealized TC. The inner core rainbands were associated with outward propagating VRWs. They showed that VRWs were most active below the maximum in the rainband-induced diabatic heating in the mid-troposphere, suggesting that VRWs are low and mid-level phenomena. Below the diabatic heating maximum, Ekman pumping associated with the VRWs was responsible for initiating the deep convection on the order of 7 km deep. Similarly, Wang (2002a,b) found rainbands were associated with VRWs, seen as WN1 and WN2 maxima in PV propagating radially outward from the eyewall. Rising motion was found near one quarter of a wavelength ahead of the cyclonic vorticity maxima identified as VRWs. Similarly, Li and Wang (2012) associated the radially outward updraft relative to the PV maximum with convergence within the boundary layer. The radially inward-directed boundary layer flow interacted with the PV structure such that convergence was produced on the radially outward side of the PV band, supporting the radially-outward updraft maximum. In addition, the updrafts were further enhanced by strong divergence aloft. This feature was similar to the studies of Chen and Yau (2001) and Wang (2002a,b, 2008), which showed divergence above the level of maximum diabatic heating.

The azimuthal structure of simulated VRW-induced rainbands was also examined. (Wang 2002b) found that WN2 VRW updrafts leaned anticyclonically (relative to the TC center) with increasing height. However, WN1 VRW updrafts were found to lean downwind, with the exception of those near/in the eyewall. Li and Wang (2012) found similar divergence patterns in azimuth. WN2 divergence and vertical vorticity appeared similar to that of Wang (2002a,b), which showed an upwind tilt of both divergence and vertical vorticity along WN2 VRW structures.

The verification of VRWs was also employed in several studies, comparing the speed of VRWs to the theory of MK97. For example, Franklin et al. (2006) concluded that the rainbands associated with VRWs agreed well with the dispersion relation of MK97. The radial phase speeds of their simulated VRWs were on the order of 4 m s^{-1}, similar to the range of phase speeds predicted by MK97. Similarly, in azimuth Wang (2002b) and Franklin et al. (2006) showed that the azimuthal propagation of VRW rainbands was slower than that of the tangential wind.

While the studies above focused primarily on WN1 and WN2 VRWs, Wang (2008) deduced that WN > 4 asymmetries are suppressed within the inner core. Wang demonstrated the strain-flow-dominated region of the inner core sheared spiral rainbands more rapidly than convective overturning. This is consistent with the original theory of MK97, which displayed the shearing of VRWs by the horizontal wind as they propagated outward.

In the current study, VRWs generated near/in the eyewall are shown propagate outward and produce rainbands. The verification of VRWs in the inner core region gives evidence to eyewall VRWs, without which VRWs in the inner core could

arguably not exist. Indeed, studies such as Braun et al. (2006) and Menelaou and Yau (2014) examined eyewall asymmetries in PV and concluded that the associated asymmetric convection of the eyewall is associated with VRWs. The observational study of Reasor et al. (2000) suggested that these types of structures were closely tied with the expulsion of high PV air radially outward from asymmetries in the eyewall that formed rainbands in the inner core. The inward-directed advection of angular momentum associated with eyewall/near-eyewall VRWs may then act to accelerate the mean flow of the TC, while the axisymmetrization process is associated with outward-directed PV waves or convectively-coupled and sheared VRWs (e.g. MK97; Franklin et al. 2006; Li and Wang 2012).

Although there are multiple studies of VRW in a modeling framework, only two observational studies explicitly examine VRWs. The first was Reasor et al. (2000) in which observations of Hurricane Olivia (1994) from two National Oceanic and Atmospheric Administration (NOAA) WP-3D aircraft C-band Doppler radars were employed. They observed the expulsion of high vorticity filaments from the eye in what they concluded were convectively-coupled VRWs. They noted that Hurricane Olivia's PV structure became very "ringlike" in nature, suggesting that the symmetrization process of VRWs may be important in the intensification process. An important limitation of their observational study is that wind field composites from the aircraft were only available every 30 min. Thus, the flux of momentum and the role of asymmetric dynamics could not be quantified. However, the expulsion of high PV filaments (VRWs) in the inner core was closely tied to reflectivity bands of similar

radial wavelength (5-10 km), suggest a coupling of VRW structures and convection in the inner core.

The second observational study available is that of Corbosiero et al. (2006) which focuses on Hurricane Elena (1985). A Weather Surveillance Radar-1957 (WSR-57) was used to examine the reflectivity structure of Hurricane Elena at a high resolution of 750 m every 5 min. However, only the 0.4° elevation was used, limiting their spatial analysis to the low-levels. Furthermore, no radial velocity data were available. The authors did find that the reflectivity structures of spiral rainbands exhibited phase speeds consistent with those theorized in MK97 and the asymmetric contribution to reflectivity was primarily explained by WN2 energy. Hence, it was concluded that the spiral rainbands were likely tied to WN2 VRWs.

2.2 Gravity Waves and Advection

Additional hypotheses for spiral rainband formation have been proposed. For example, Abdullah (1966) hypothesized inertia-gravity waves could be responsible for the initiation of spiral rainbands in TCs. However, as noted in Willoughby (1977), outward-propagating inertia-gravity waves are unlikely in many TCs. Willoughby concluded inertia-gravity waves would exhibit a propagation speed faster than the mean wind, which was shown to be dissimilar to that of observed traits of spiral rainbands. Instead, Willoughby proposed inward-propagating inertia-gravity waves were responsible. In his model, it appeared possible that inertia-gravity waves excited near the edge of a TC could propagate inward, contributing to spiral rainband formation. More recently, Chow et al. (2002) argued that fluctuations in vorticity could excite

gravity waves within a TC. As these gravity waves propagated, they seemed to be responsible for initiating spiral rainbands. Their definition of rainbands included only those moving around the TC center [i.e. excluding stationary structures such as in (Didlake and Houze 2013b)]. This included bands both in the inner and outer cores. Within this current study, outer core rainbands are not examined.

A more recent hypothesis suggests that rainbands are not coupled with VRWs and are the result of non-linear advection of hydrometeors by TC winds (Moon and Nolan 2015). This was illustrated in in their study by showing that a passive tracer placed within the TC flow could be easily filamented and represent the shape of a spiral rainband. Furthermore, the simulated rainband that motivated their study displayed no resemblance to VRWs. They used a Fourier decomposition and showed that there were no WN2 cyclonic PV maxima associated with the rainband in question. Thus, they concluded that the inner core rainbands are associated with the non-linear advection of convective clouds by the tangential wind. However, the source of this convection was not explicitly explored.

Chapter 3: SMART Radar Data

3.1 SMART Radar Overview

The characteristics of the SMART radars were seen in Biggerstaff et al. (2005). It should be noted that SMART radar 2 was upgraded to dual-polarimetric capability in 2010. Both radars have a half-power beam width of 1.5° and have a unique capability to sample landfalling TCs at high resolution without suffering severe attenuation. Before 2010 both SMART radars operated at a linear, horizontal polarization with a 250 kW

magnetron transmitter. Data collected by the radars are reflectivity Z_H, Doppler velocity V_R, and spectrum width σ. After 2010, SMART radar 2 also collected polarimetric variables including differential phase ϕ_{DP}, differential reflectivity Z_{DR}, and correlation coefficient ρ_{HV}. Further technical information for the SMART radars is given in Table 1.

3.2 SMART Radar Deployments

During Hurricanes Isabel, Frances, and Irene, the SMART radars used various methods of data collection to address a variety of different objectives (e.g. Hirth et al. 2012). 360° and sector volume scans that sampled a majority of the depth of the troposphere are most useful to this study and are summarized in Table 2. In addition to the SMART radars, the WSR-88Ds at Melbourne, FL (KMLB) and at Morehead City, NC (KMHX) were used in the dual-Doppler retrievals in Hurricane Frances and Hurricane Irene, respectively. Although SMART radar 1 was available in Hurricane Frances, the SMART radar 2-KMLB baseline offered a much larger dual-Doppler domain, suitable for rainband study. SMART radar 1 was not available during Hurricane Irene. See Fig. 1 for radar locations during each deployment.

3.3 Analysis Technique

SMART radar and WSR-88D data gathered from the National Centers for Environmental Information (NCEI) were processed objectively through the Py-ART Toolkit available from the Atmospheric Radiation Measurement (ARM) Climate Research Facility (Collins et al. 2012). Py-ART objectively dealiases the V_R field, while

also mitigating noise and incoherent second trip echoes. The data were also examined subjectively to correct aliasing not captured by the algorithm. Regions where Py-ART performed poorly were manually corrected using SoloII (Oye et al. 1995).

After editing, data were interpolated to a Cartesian grid using a Natural Neighbor interpolation technique (Sibson 1981). Data from Hurricane Isabel and Hurricane Frances were interpolated to a 1 km spaced grid in the horizontal and the vertical, and data in Hurricane Irene were interpolated to a 500 m grid in the horizontal and the vertical. Radial velocity data were smoothed with a Gaussian filter with a sigma of 1. Additionally, an advection correction was applied to the V_R and Z_H fields by calculating a mean ground-relative storm motion, focusing on the features of interest to be passed into the dual-Doppler analysis. Because the dual-Doppler domain is very small compared to that of the hurricane, spatial variability in the horizontal wind likely induced minimal error in the advection correction. Additional information regarding the Cartesian grid domain is given in Table 3.

Gridded data were passed into a three-dimensional variational data assimilation (3DVAR) dual-Doppler wind retrieval algorithm (hereafter, DDA; Potvin et al. 2012a). This DDA technique has been shown to be more robust in retrieving the three-dimensional wind, especially when storm-topping ground-based radar observations are unavailable (Potvin et al. 2012b). The DDA technique here is thought to be superior to standard retrieval methods (e.g. Biggerstaff and Houze 1991), since the explicit integration of the mass continuity equation is not the only constraint on the retrieved flow. The solution is constrained by both mass continuity and by the measured radial velocity field. The residual between the derived three-dimensional wind and the radial

velocity observations of both radars used in the DDA is minimized. Only the region in which there was a minimum 30° crossbeam angle between both radars was used in each hurricane case.

Chapter 4: Hurricane Overviews

All three hurricanes used in this study are briefly described in this section. In addition, mesoscale summaries of hurricanes near the time of analysis are also provided, focusing on features to be analyzed by DDA. Summaries are extracted from National Hurricane Center Tropical Cyclone Reports by Beven and Cobb (2003), Beven (2004), and Avila and Cangialosi (2012) and can be referred to for more complete information.

4.1 Hurricane Isabel (2003)

Hurricane Isabel formed from a westward propagating tropical wave that had moved off of the coast of Africa. Isabel initially formed as a Dvorak-estimated tropical storm on 6 September, and strengthened to a maximum intensity on 11 September with winds of 75 m s^{-1} (145 kt). It moved northeastward from the central Atlantic Ocean, making landfall near Drum Inlet, NC at 1700 UTC on 18 September as a Category 2 hurricane (42.7-48.9 m s^{-1}). During the time leading up to landfall, Isabel exhibited a double eyewall structure and underwent a failed eyewall replacement cycle. Near the time of landfall, Isabel's double eyewall structure was evident (Fig. 2) and a wind maximum in the outer eyewall (approximately 90 km from storm center). Additionally, the wind field of Hurricane Isabel grew significantly over 17-18 September. Hurricane force winds extended as far as the Virginia border near landfall, suggesting the

hurricane wind field extended 150-200 km from the center of circulation. Fig. 2 shows an asymmetric precipitation structure with the majority of heavy precipitation on the northwest side of Isabel. Multiple spiral rainbands with $Z_H > 40$ dBZ were radially outward from the eyewall. Many of these bands on the order of 5-10 km in radial extent moved through the dual-Doppler domain between SMART radar 1 and 2 (Fig. 2a) between 1200 UTC to near landfall. The rainbands appeared to spiral inwards toward the eyewall. However, they moved outward in time, as demonstrated by the black arrow in Fig. 2 following one rainband through time.

4.2 Hurricane Frances (2004)

Like Hurricane Isabel, Hurricane Frances developed near 0000 UTC on 25 August from a tropical wave off of the African coast and moved generally northwest across the Atlantic Ocean. Its maximum intensity came on 31 August when it reached Category 4 status (59-69 m s^{-1}). After passing through the central Bahaman Islands as a Category 3 hurricane, Frances weakened to a Category 2 storm as a result of increased environmental wind shear before making landfall near the southern tip of Hutchinson Island, FL around 0430 UTC on 5 September. The hurricane wind field extended approximately 100-120 km from the center of circulation. In fact, SMART radar 1 (not used in the Frances analysis) sustained complete failure after losing antenna control in a strong gust, likely upwards of 50 m s^{-1}. SMART radar 1 was located approximately 100 km from the center at this time. A PPI from KMLB near 1116 UTC (Fig. 3) shows a relatively compact eye with a radius of approximately 45 km. The heaviest rainfall was found on the northeast side of the eye with the edge of the inner core passing through

the eastern SMART radar 2-KMLB dual-Doppler lobe. Thus, the inner core rainbands that apparently cease radial propagation can be assessed. The hurricane moved slowly and weakened during this period across central Florida before moving out over the Gulf of Mexico early on 6 September. With its slow movement and asymmetric precipitation structure, rainfall totals exceeded 35 cm on the northwest side of Frances in north-central Florida to the northeast of the SMART radars. Frances also went on to produce heavy rain as an extra-tropical system in the Carolinas with the storm-maximum rainfall near the eastern slopes of the Appalachian Mountains.

4.3 Hurricane Irene (2011)

Hurricane Irene formed into a tropical storm near 0000 UTC on 21 August from a tropical wave. It moved west-northwest across the Atlantic Ocean, interacting with Hispanola on 23 August before strengthening in a weakly sheared environment on 24 August. With an intensity of 105 knots and a minimum central pressure of 957 hPa, Irene moved through the Bahamas on 24 August subjecting residents to Category 3 winds. As it moved toward the East Coast, it began interacting with an upper level trough situated across the eastern United States, which prevented Irene from making landfall in Florida or Georgia. After weakening after this interaction and undergoing an eyewall replacement cycle, Irene moved north-northwest toward Cape Lookout, NC on 27 August at 1200 UTC. Irene's wind field was very compact with hurricane force winds generally remaining confined between the Outer Banks of North Carolina and the continental coast. Irene’s center passed to the east of the KMHX-SMART radar 2 dual-Doppler lobe (Fig. 4). However, as it approached several inner core spiral rainbands

moved through the dual-Doppler domain. Due to limited site selection, SMART radar 2 was positioned on a nearly west-east oriented baseline only 20.1 km from KMHX. Like Hurricane Frances, Irene exhibited a northward biased asymmetric precipitation structure with a majority of heavier rainfall on the north side of the eye. Several rainbands moved into the dual-Doppler domain. One notable event occurred at 1116 UTC (Fig. 4c) when a rainband spiraling inward to the eyewall began propagating through the domain. Flooding was the dominant impact of Irene with a maximum in rainfall observed near Bayboro, NC (40.0 cm). Additional impacts were felt in New England where extreme rainfall devastated parts of the region, notably in river valleys.

Chapter 5: Dual-Doppler Analysis Results

The SMART radar deployments in each hurricane provided an opportunity to sample the kinematic structure of inner core spiral rainbands. The Hurricane Isabel dataset also provided the temporal and spatial resolution to examine the azimuthal and radial propagation of the spiral rainbands. These three hurricane datasets yield a greater opportunity for comprehensive observational analysis of the structure of inner core spiral rainbands than has previously been possible.

5.1 Hurricane Isabel

5.1.1 Mesoscale Context

Within the dual-Doppler domain, two primary rainbands are examined for Hurricane Isabel. The first is located near x=0, y=75 in Fig. 5 (hereafter, the northwest rainband) and the second is located near x=60, y=50 in Fig. 5 (hereafter, the eastern

rainband). It can be seen that the eastern rainband is separated from the eyewall (near x=75, y=25) by about 20 km in radial distance. Counter-clockwise along the rainband, the radial separation of the band and the eyewall becomes smaller, suggesting that the rainband was not oriented along a constant radius relative to the center of circulation. The northeastern rainband appears to be intersecting another rainband near x=-40, y=25 (hereafter, the western rainband). There also appear to be weaker rainbands and spurious maxima in Z_H in the vicinity of the primary rainbands upon which the dual-Doppler analyses will focus. The western and northwestern rainbands appear to be separated by about 10 km, but the northwestern rainband and the eastern rainband appear to be separated by nearer 40 km distance. Thus, it appears that the rainbands in Hurricane Isabel decrease their radial separation as they move away from the eyewall.

As can be seen in Fig. 2, rainbands in this region appear to dissipate as they rotate to the southwest quadrant of Hurricane Isabel. This is likely due to the environmental shear acting upon the TC. The 850-200 hPa shear was relatively weak across the area according to the National Center for Environmental Prediction's reanalysis dataset (4-6 m s^{-1} directed toward the north northwest). Thus, the rainbands in question were positioned in the downshear-left quadrant of the TC, an area that has been shown to be favored for convection (e.g. Corbosiero and Molinari 2002) due to the shear-driven upper-level divergence in the downshear region of TCs (e.g. Jones 1995).

On the mesoscale, the vertical cross section through the inner core region of Hurricane Isabel (Fig. 7) shows the rainbands discussed above. Within the environment of these rainbands, waves in vertical velocity appear to exist with deep downdrafts analyzed outside of the rainbands and deep updrafts nearer the rainbands. This implies

that the mesoscale area is characterized by multiple waves (possibly VRWs or inertia gravity waves) that appear to be the associated with these rainbands.

5.1.2 Kinematic Structure

The SMART radars collected data from the inner core of Hurricane Isabel from 0930 - 2200 UTC on 18 September 2003. As noted in Chapter 3, the region of hurricane-force winds was quite extensive, yielding an extensive time interval in which to sample the inner core. Here, the 1440 - 1500 UTC time frame of is presented, examining two of the most prominent rainbands seen in the DDA domain. The approximate temporal resolution between volumes was an average of three minutes, much higher than Reasor et al. (2000). Furthermore, three-dimensional wind retrievals were possible, extending the analysis space significantly over that of Corbosiero et al. (2006) and a much greater resolution than Reasor et al. (2000). Instead of focusing on individual WN components of PV as in some past studies, the full three-dimensional wind field will be used, similar to Chen and Yau (2001) and Li and Wang (2012). However, Fourier analysis of the inner core reflectivity structure was possible.

Fig. 2 displays a time series of 0.5° Z_H from KMHX (south of the SMART radars at the domain origin). At 1405:07 UTC (Fig. 2a), the eyewall of Hurricane Isabel was clearly asymmetric in Z_H with local maxima on the northwest and southeast sides of the TC. Furthermore, inner core spiral rainbands appear to initiate near Z_H maxima and slowly propagate outward radially (indicated by the arrows in the figure). In addition to the specific rainband indicated by the arrow in Fig. 2, additional rainbands can be seen within the SMART radar DDA domain. The portion of the bands in the

domain (black contours in Fig. 2) appear nearly concentric with respect to that of the eyewall. As predicted by MK97, the radial expulsion of wave energy from vortex Rossby waves within the eyewall will undergo filamentation (Wang 2008) and become elongated. This is a trait seen in Z_H with the distance between rainbands decreasing clockwise along the rainband.

MK97 and Wang (2008) suggested that most VRWs within the eyewall will have an azimuthal WN1 or WN2 asymmetric vorticity structure. To determine the WN structure of the rainbands, the Z_H field sampled by KMHX is decomposed via Fourier analysis to approximate the azimuthal WN structure of the rainbands of Isabel. While the Fourier components of asymmetric reflectivity are not necessarily representative of the Fourier components of PV, Corbosiero et al. (2006) demonstrated that the reflectivity of rainbands in Hurricane Elena were dominated by WN2 components of Z_H and that the rainbands were consistent with VRW theory. Using Fourier decomposition of the 2.50 km ARL Z_H field demonstrates that the first two asymmetric components of Z_H (the sum of WN1 and WN2) contribute significantly to the rainband near x=75 and y=50 (Fig. 8a), for example. The magnitude of the sum of WN1 and WN2 components (shown in Fig. 8c) is near 34-36 dBZ. Fig. 8d shows the sum of the WN3 and WN4 components of Z_H. The contribution near x=75 and y=50 is nearer 32-34 dBZ on the azimuthally clockwise (i.e. upwind) portion of the band. Higher order WNs (sum of WN5-WN10 and sum of WN11-WN20; Fig. 8e-f) appear to be suppressed in the region of the rainband, suggesting that Z_H is dominated primarily by WN1 and WN2 components with weaker contributions by WN3 and WN4.

A similar feature is seen in the rainband beginning near x=25 and y=-125 extending cyclonically to x=0 and y=75. Along the majority of this large rainband, the WN1 and WN2 sum ranges from 32-38 dBZ. Near the upwind portion of the band, WN3 and WN4 componets near the same magnitude. However, it appears that the rainbands shown here are primarily WN1 and WN2 dominant in reflectivity. While it can be concluded that the rainbands seen in Isabel resemble WN1 and WN2 type asymmetries for the most part, small deviations of rainbands from orientations concentric with respect to the eyewall may cause inaccurate Fourier decomposition of the rainbands themselves.

DDAs from 1442:00 through 1456:00 UTC show two distinct rainbands within the dual-Doppler domain (Fig. 9) at 3.5 km ARL. These bands are characterized by $Z_H >$ 40 dBZ, with values higher than 50 dBZ below 2 km above radar level (ARL). In the radial direction (relative to the TC center), the bands display a single peak in Z_H, but in the azimuthal direction there is more complexity in the reflectivity structure. The azimuthal complexity can be seen additionally in Figs. 8e-f, where individual maxima in the higher order Fourier components can be seen inlaid within the more uniform WN1 and WN2 rainband. While these inhomogeneities may be partially due to variations in thermodynamic forcing, the kinematic forcing can be assessed via DDA.

The vertical velocity field of these rainbands exhibits characteristics similar to that of the reflectivity structure. A generally uniform, single updraft was slightly lagging the Z_H maxima and a downdraft was leading the Z_H maxima in the radial direction (i.e. radial WN1 asymmetry in *w*), but multiple maxima and minima in *w* azimuthally were apparent. Take, for example, the rainbands in the northeast corner

(x=35, y=40 in Fig. 9a) and the eastern portion of the domain (x=65, y=20 in Fig. 9e) at 1442 -1447 UTC and 1452-1456 UTC respectively (Fig. 9). Vertical velocities are maximized at 4-5 m s^{-1} in the northeast rainband and 2-3 m s^{-1} in the eastern rainband at the 3.5 km analysis level.

Utilizing the horizontal wind components, the vertical vorticity ζ was computed (using a finite center difference) and the mean vertical vorticity $\overline{\zeta}$ of each analysis level was subtracted, yielding the perturbation vertical vorticity ζ' (Fig. 10; z = 3.5 km ARL). Examining the same rainbands as above, they appear to be associated with elongated positive vorticity perturbations with maxima of 1.6×10^{-3} s^{-1} and 2×10^{-3} s^{-1} respectively. The maxima appear to lag both the Z_H maxima and the *w* maxima. In fact, the vorticity bands lag the vertical velocity bands near one-quarter of a wavelength, as predicted by the modeling studies of Wang (2002a,b). More importantly, it appears that the radial extent of the northwest vorticity band (extending from x=25, y=30 to x=45, y=50 in Fig. 10a) versus the eastern vorticity band (extending from x=60, y=10 to x=80, y=25 in Fig. 10e) is smaller with an approximate radial extent of the northwest band on the order of 5 km and the southeast band on the order of 7-10 km. Thus, these observations suggest that the radial extent of the vorticity maxima associated with these rainbands increases with increasing radial distance from the TC center. This is indicative of the shearing of the VRWs prescribed by MK97 and Wang (2008).

At the 1.5 km ARL analysis level, the vorticity structures continue to be apparent, but appear to be oriented azimuthally counterclockwise (i.e. downwind) of the 3.5 km maxima (Fig. 11). Although difficult to discern due to weakening velocities nearer the surface, the slight outward radial tilt and the downwind shift of the updrafts

appears to be consistent with the vorticity structure (Fig. 12). This downwind shift with decreasing altitude of the vorticity and updraft bands was predicted in numerical simulations of WN2 VRWs (Wang 2002b; Li and Wang 2012) and is consistent with the structure of VRWs seen in Franklin et al. (2006). However, the outward radial tilt of the observed waves is not nearly as severe as in either study. This is likely due analyses in these studies being performed nearer the radius of maximum winds, where tilting of waves may be more extreme than further outward from the TC center (see Chapter 5.3 for an analysis of a rainband near the RMW).

As seen in Figs. 9-12, the azimuthal structure of the rainbands is quasi two-dimensional. The filamented structure of the rainbands can be examined by taking vertical cross sections. Fig. 13 and Fig. 14 are representative of normal cross-sections through two different rainbands. Cross-sections L1-L2 (Fig. 13) and L3-L4 (Fig. 14) are presented at 1442 and 1452 UTC respectively. A plan view in Figs. 13a and 14a shows the location of each cross-section. Contours of w overlaid on the vertical Z_H field show that updrafts extend to the top of the analysis domain (9.5 km) and are located radially inwards of the Z_H maxima. In this hurricane, the updrafts are nearly tropospherically deep. Furthermore, it is confirmed that the updraft leans slightly outward radially, but not to the extent of Li and Wang (2012).

The vertical structure of ζ indicates that the maximum in the positive ζ lags the maximum in the rising motion (Figs. 13c and 14c), though less than the one-quarter wavelength hypothesized by Wang (2002a). The vorticity pattern was likely affected by amplification by stretching in the weak convective updrafts. This appears to be particularly true for L1-L2 (Fig. 13). Indeed, convergence was found from the surface to

3 km, likely enhancing the vorticity field and producing a structure with less distance between the ζ and the *w* maxima than theoretically predicted. In contrast, the rainband examined in L3-L4 (Fig. 14) had weak divergence near its vorticity maximum and the separation between ζ and *w* maxima were close to the theoretical expectation.

Like Li and Wang (2012), strong low-level convergence (near -1.8×10^{-3} s^{-1}) is seen below 3 km in both cases beneath the updraft, which has its maximum near 5 km altitude. Chen and Yau (2001) suggested that frictional convergence was generated radially outward of outward-propagating PV waves. Hence, the vorticity bands themselves helped to produce convergence in the boundary layer, which helps sustain the convective updrafts. Diabatic heating further enhances the updrafts, which can amplify the vorticity field, creating a positive feedback mechanism. While the results of the 1442 and 1452 UTC analyses are similar, the reader is cautioned that the lowest 1-3 km of the atmosphere were under-sampled in the cross-section at 1452 UTC due to low-level beam blockage. However, the divergence structure is similar to that of the 1442 analysis above 3 km, suggesting that the rainbands were likely similar in the low-levels as well.

Although it can be inferred from the radial WN1 vertical velocity structure, the divergence structure indicates a vertical, closed circulation across the rainband. Thus, flow is directed from the updraft, radially outward toward the downdraft aloft and from the downdraft toward the base of the updraft near the surface. This idea is consistent with the structure of Z_H maximum located between the updraft and downdraft. Thus, hydrometeors likely are falling out on the periphery of the updraft as their terminal velocity overcomes the vertical velocity.

5.1.3 Rainband Comparison to Theory

To determine if the rainbands in Hurricane Isabel follow the dispersion relation presented in MK97, the radial and azimuthal propagation is compared to theory. Since the DDAs were available in not only the inner core, but also near the eyewall, a composite profile of tangential wind relative to Isabel's center of circulation was computed. To define the center of circulation objectively, a Ground Based Velocity Track Display method was used (Lee et al. 1999; Lee and Marks 2000). The analysis was performed on constant altitude plan-position indicators (CAPPIs) derived from KMHX, which had a much larger unambiguous range than either of the SMART radars. The dependence of the radial phase speed (given by dividing Eq. 1 by the radial wavenumber k) on the radius of wave origin was difficult to assess. Hence, the origin radius is taken to be the RMW (i.e near the eyewall) where the single-Doppler plots (Fig. 2) suggested the origin for the rainbands presented. k is the time-dependent radial wavenumber, but here the initial wavenumber $k = k_0 = 2\pi / r_{wave}$ with $r_{wave} = 10$ km is used as an approximation. Ten km was chosen as initial radial extent of waves, based on the observations of spiral rainbands propagating directly off of the eyewall in Fig. 2. The calculation of the phase speed is inversely proportional to the radial wavenumber. Using an overestimation of $r_{wave} = 20$ km, the phase speed of waves generated near the RMW is nearer 2.4 m s^{-1}. An underestimation of the initial radial wavelength ($r_{wave} = 5$ km) results in a slower phase speed of near 0.6 m s^{-1}. While Franklin et al. (2006) used Ertel's potential vorticity in their calculations, thermodynamic data were unavailable from the DDAs. Hence, a barotropic form of PV is used as an estimate (see the discussion of Eq. 1 in Chapter 2.1).

Utilizing the estimate of a 10 km radial wavelength, results indicate that waves generated near the RMW should propagate radially outward near 1.5 m s^{-1} with a stagnation radius on the order of 200 km, given that the RMW is near 90 km. This computation is valid for n = 2 VRWs (i.e. WN2), which is supported by the DDA results presented in Chapter 5.1.2. Fig. 2 qualitatively supports a stagnation radius of near 200 km, with the majority of inner core rainbands being within 250 km of the center and very few outside this region. Fig. 15 shows the azimuthal mean vorticity as a function of radius at the 2.5 km analysis level. The 2.5 km altitude was chosen as the level at which the vorticity anomalies are most prominent and the lowest resolvable analysis level at distances far from the DDA baseline. While not perfect, the azimuthal propagation of the waves appears to meet the estimate of 1.5 m s^{-1} to a reasonable degree of accuracy. As individual maxima propagate through the domain, their radial phase speeds seem to closely match the calculated phase speed (i.e. see the wave between 160-170 km in Fig. 15). Furthermore, the maxima appear to decrease in radial extent, suggesting the radial WN of vorticity increases with increasing radius from the TC center.

In azimuth, WN2 VRWs seem to propagate slower than that of the mean tangential wind. To illustrate this, Fig. 13 displays the propagation of the vorticity field at 118 km in radius, coincident with a possible VRW in Fig. 16. The dashed line in Fig. 16 shows the mean tangential wind derived from the composite wind field at 118 km from the center of circulation. The wave between 1450 and 1456 UTC appears to propagate much slower than 36 m s^{-1}, suggesting a Rossby-type wave, as opposed to a gravity wave.

5.2 Hurricane Frances

5.2.1 Mesoscale Context

The rainband that will be focused on for Frances is pictured in Fig. 17 near x=50, y=25. This rainband was characterized by high reflectivities and can be seen on the edge of the inner core. The eyewall at this time was being affected by the Florida Peninsula and had become broken. However, the remnant eyewall was situated near x=0, y=-70 in the figure. Between these two regions, there were two other prominent rainbands. The first is located near x=40, y=0, just inside the dual-Doppler domain. The second, weaker rainband is near x=50, y=10 in the figure. Similar to the rainbands of Hurricane Isabel, the radial separation of these rainbands appears to decrease as the rainbands near the edge of the inner core. The first rainband is separated from the second by about 25 km, but the second rainband is separated from the rainband on the inner core edge by about 20 km.

Again, similar to Isabel, the rainbands are found in the downshear-left quadrant with the shear vector oriented toward the northeast with a magnitude near 4 m s^{-1} (see Fig. 6b). It is apparent that the rainbands' Z_H decreases clockwise in Fig. 17, suggesting that the rainband genesis region is in the downshear-right quadrant and the mature rainband region is in the downshear-left quadrant. This can also be seen in Fig. 3.

5.2.2 Kinematic Structure

The DDAs from Hurricane Frances offer the advantage of viewing VRW structure near the theoretical stagnation radius (the edge of the inner core). While the phase speed of the rainbands cannot be elucidated due to temporal sampling in

Hurricane Frances, the kinematic structure can be examined. Fig. 18 shows a vertical cross section (line L5-L6 in .Fig. 18a) through a spiral rainband that contains multiple stronger convective cells lagging the initial rainband. The intent here is to examine the overall structure of a rainband that is more "broken" in nature.

Several vorticity maxima are seen along the L5-L6 segment centered at 11 km and at 16 km with the first maximum situated in the upper troposphere and the second maximum seen below 2 km height (Fig. 18c). While they are not outward leaning for the most part, they do appear to be associated with updrafts on the order of 1-3 m s^{-1} The updraft structure exhibits more of a WN2 radial structure than WN1 in vertical velocity across the rainband. The radially inward vorticity maximum (near 11 km) exhibits a radially lagged position behind the updraft (near 13 km), but is situated above the low level updraft. Below 2 km altitude, the radially inward vorticity maximum is situated above near-surface convergence. Similarly, the vorticity maximum centered near 16 km range is radially inward of a region of convergence 2 km altitude (near 24 km) with a secondary, but weaker, maximum collocated within the updraft. It appears that vorticity maximum centered near 16 km range is similar to the VRWs in Hurricane Isabel, where the lag-separation between the updraft and vorticity maximum was reduced, likely due to the effects of stretching in the lower level updraft. It appears that the updraft tilted and stretched vorticity near 27 km range, but the updraft may be convectively coupled with the maximum nearer 16 km range, similar to Hurricane Isabel. The radially outward vorticity maximum appears nearer the theoretical one-quarter separation than does the radial inward feature. Regardless, both updrafts were associated with low-level convergence, mostly radially outward from the vorticity

maxima. As noted by Chen and Yau (2001), PV anomalies can induce low-level Ekman pumping. The convergence can then feed the updraft, reinforced by diabatic heating associated with latent heat release through condensation.

Compared to the vorticity structures seen in Isabel, these vorticity maxima appear to be less deep and may have vertically propagated into the mid to upper troposphere, consistent with vertically propagating VRWs (McWilliams et al. 2003). Furthermore, the radial separation between local vorticity maxima is smaller, implying the increase in radial WN of vorticity bands near the stagnation radius. Thus, the rainbands near the stagnation radius appear to become less uniform in azimuth.

5.3 Hurricane Irene

5.3.1 Mesoscale Context

The hurricane wind field, while small, still supported radially-outward propagating rainbands in Hurricane Irene. Fig. 19 illustrates several rainbands propagating off of the outer eyewall (near x=25, y=0) with the first rainband near x=10, y=10 and the second rainband near x=0, y=25. It is clear that the edge of the outer core is near x=0, y=50, where rainband structures are very diffuse. The second rainband appears to intersect the outer portion of the inner core near x=25, y= 60, and is much farther from the first rainband than it is from the inner core edge. In the southern portion of the second rainband, it appears the rainband is almost equidistant from the first rainband and the outer portion of the inner core.

Unfortunately, the rainbands appear to decay on their counter clockwise sides, which is likely due to the environmental shear. In Fig. 6c, the environmental shear

vector was nearly double than either Frances or Isabel (near 8 m s^{-1}) and was directed just north of northeast. Thus, the position of the dual-Doppler domain was on the counter-clockwise edge of the downshear-left quadrant. As seen in Fig. 4, rainbands appear to die quickly near this region, suggesting those that are generated in the downshear-left quadrant were decaying as they moved into the upshear-left quadrant (Jones 1995).

5.3.2 Kinematic Structure

DDAs from Hurricane Irene are presented in Fig. 20, showing the vertical vorticity perturbation magnitudes for each DDA time at a spatial resolution of 500 m. At this resolution, the vorticity structure shows more azimuthal variability as the vorticity field becomes noisier. However, as in Figs. 20b,c elongated vorticity maxima (x=15, y=5 in Fig. 20b and x=8, y=15 in Fig. 20c) are apparently tied to elongated convective rainbands within the center of the DDA domain. These structures are seen in the rear of the rainband in an azimuthal sense with the strongest vorticity maximum seen in the 1006 UTC analysis (Fig. 20b). As noted earlier, the rainbands appeared to be rotating into the upshear-left quadrant, where convection is less favored (Jones 1995). Nonetheless, this rainband is characterized by vorticity perturbations exceeding 1.6×10^{-3} s^{-1} and a radial vorticity extent near 5 km. While the rainband vorticity structure appears more diffuse at 1016 UTC (Fig. 20c) with a broken, complex structure in azimuth, the 1.0 km plot of radar reflectivity suggests the rainband was more two-dimensional (Fig. 21a).

In the vertical cross section (Fig. 21c), the low-level vorticity maximum associated with the VRW below 4 km was observed at a range of 6 km while the updraft core was observed at 10 km. The upper level structure of the TC was not well sampled at ranges closer than 10 km due to the limited elevation angles employed in the WSR-88D. Assuming that the distance between the updraft maxima and the weak downdraft at 16 km range represents half the VRW wavelength, the updraft between the vorticity maximum and the updraft maximum fits the theoretical one-quarter wavelength quite well. It should be noted that the VRW structure is well defined below 5 km altitude. Hence, unlike Isabel but more like Frances, the VRWs are not tropospherically deep. It should also be noted that the region through which these bands are propagating represents the outer edge of the inner core where the VRWs are arguably nearing their stagnation radius, similar to that seen in Frances. This, in conjunction with the shear likely degraded the rainbands rapidly in this region, causing their structures to become more diffuse and break apart.

An analysis at 1116 UTC is presented in Fig. 22, which shows a vertical cross section (L9-L10) of the kinematic structure of an inner core spiral rainband and the outer eyewall of Irene (see Fig. 4b). This example represents a rainband forming near the eyewall; however, because of the limited extent of the domain and the 10 minute separation between DDAs in Irene, this wave can only be examined at one instant in time. The vertical velocity field (in Fig. 22b) shows a similar structure to that of Hurricane Isabel, but Irene exhibited more outward tilt with height in the vertical velocity structure. The deep vertical vorticity associated with the RMW can be seen between L9 and 4 km range along the cross-section. A separate vorticity maximum is

located near the 7 km range at the surface and tilts outward to 14 km range at 7 km altitude. This vorticity structure is complex. Near the surface, the vorticity maximum is lagging the updraft core by about 2.5 km, which would be one-quarter of the distance between the midlevel (3-4 km altitude) downdrafts that define the developing VRW wavelength. Between 2 and 4 km altitude, the vorticity maximum is collocated with a deep layer of strong convergence that is feeding the outward extent of the main updraft. Above 4 km, the vorticity maximum is within a region of strong divergence and collocated with the updraft maximum. This 6 km deep updraft appears to be collocated with the developing VRW rainband beyond 10 km range in the cross-section. Hence, the developing VRW is heavily influenced by eyewall dynamics.

There is a WN1 asymmetry in the leading rainband (near 10 km range along L9-L10) and this structure can also be seen in the divergence field. Deep divergence above 3 km is apparent with the updraft, with a level of convergence seen below 3 km. Unlike the previous analyses, the convergence maximum appears to be close to 1 km altitude, suggesting the convergence of parcels near the top of the boundary layer. Thus, the flow in or near the boundary layer is in opposition to the radial inflow, similar to the results of Wang (2002a). Taking a cross-section parallel to the rainband and near 11 km range along L9-L10 within the region of rising motion (Fig. 23, line L11-L12), it is clear that the updraft is tilted upwind (toward L12). Upwind tilt with increasing altitude is consistent with numerical studies of VRWs such as (Wang 2002a) as well, especially for WN1 VRW structures near the eyewall.

Chapter 6: Rainfall from Rainbands

6.1 Inner Core Rainfall

As noted in Marks and Houze (1987), Houze (2010), and Rogers et al. (2012), the primary precipitation growth process within the inner core is from ice microphysical processes, similar to the production of the stratiform region in a mature mesoscale convective system (MCS; Biggerstaff and Houze 1991; Biggerstaff and Listemaa 2000). Aircraft observations of the inner core in Hurricane Norbert (1984) showed that the inner core region of that hurricane was dominated by stratiform processes with a majority of hydrometeors at flight level being small ice crystals. These ice crystals were advected radially outward by the secondary circulation of the TC, consistent with the conceptual model by Marks and Houze (1987; see their Fig. 5). Profiles of radar reflectivity from the Tropical Rainfall Measuring Mission's precipitation radar (TRMM PR; Kummerow et al. 1998) suggests the inner core of hurricanes is largely stratiform. For example, contoured frequency by altitude diagrams (CFADs) in Houze (2010; see Fig. 23) document the reflectivity structure in four intense TCs over the Gulf of Mexico (Dennis, Emily, Katrina, and Rita). Below 8 km, the most frequent reflectivities are less than 40 dBZ, suggesting a dearth of deep convection within this region. Moreover, the slope of the CFAD contours above the melting level is about 6.7 dB km^{-1}, which is consistent with stratiform microphysical processes (e.g. Braun and Houze 1994)

Unlike these previous observations, the results from Chapter 5 reveal deep, albeit weak, convective updrafts associated with rainbands. More importantly, maxima in the Z_H field are found below 4 km and often exceed 40 dBZ (Fig. 25), with the most frequent reflectivities near 35 dBZ in CFADs generated within the inner core regions of

each TC (Fig. 26). The slope of the CFAD contours above the melting level is about 5.6 dB km^{-1}. Both the upper level reflectivity slope and the lower level reflectivities are higher than the values observed by the TRMM PR in other storms. Differences may be related to differences in the horizontal resolution of the TRMM PR versus the ground-based radar data used to make the CFADs. It is likely that the rainbands observed in the inner core region of TC presented here adhere to a more convective reflectivity structure. Hence, the question of the contribution of rainbands to the inner core rainfall total and their classification (i.e. convective or stratiform) arises.

6.2 Precipitation Classification

In order to assess the classification of precipitation within the inner core, the method of (Biggerstaff and Listemaa 2000) was employed. This method expands the work of (Steiner et al. 1995) by classifying convective and stratiform regions of precipitation based on their three-dimensional structure. Examples of the results for the inner core of Hurricanes Isabel, Frances, and Irene (Figs. 27-29). Panel (a) in each figure shows multiple rainbands within the inner core regions of each TC with surrounding minima in reflectivity. Panel (b) in each figure displays the full results of the Biggerstaff and Listemaa (2000) classification, indicating that a vast majority of precipitation structures are classified as convective. This result is contrary to the conceptual model of the inner core region proposed by Marks and Houze (1987) and Houze (2010).

To validate the reflectivity-based classification vertical velocity from the DDAs are used. Since Biggerstaff and Listemaa (2000) use a windowing procedure as a final

step in the classification, validation was conduced before and after this procedure. The results prior to windowing contained more stratiform echoes than the final results, but were reclassified to convective due to their sporadic nature. Fig. 30 shows an example of this with the black dots in Fig. 30a representing regions that were not classified as convective (prior to the windowing procedure). The mean vertical velocity profiles (Fig. 30b) show that convective echoes (red line) exhibit mean positive vertical velocity from the surface to 5 km. The vertical velocity of non-convective echoes are more positive than the convective echoes and remain positive up to 7 km altitude, showing little resemblance to that of stratiform precipitation structures such as those in Biggerstaff and Listemma (2000).

Specific rainbands seen in Hurricane Isabel support this idea that even the low reflectivity regions that are between convective rainbands are classified as convective. Fig. 31 displays the vertical velocity profile (Fig. 31b) within a 3 km by 3 km region (red box in Fig. 31a) in the downwind portion of a rainband at 1456 UTC. The mean vertical velocity of the rainband reached a maximum near 1 m s^{-1} at an altitude of 4.5 km. Above this level, vertical velocity decreased to near 0 m s^{-1} up to near 8.5 km altitude before decreasing above 9.5 km. Although weak, it appears that the low-level profile of vertical velocity resembles that of convection and is similar qualitatively to the mean vertical velocity profile over the entire convective domain of the 1026 UTC analysis of Hurricane Irene (Fig. 30). Moreover, the vertical velocity profiles do not exhibit a mesoscale updraft over a mesoscale downdraft as proposed by Marks and Houze (1987) in their conceptual model of inner core structure. To further test the stratiform conceptual model, a region outside of a rainband (i.e. what might be

considered stratiform) was examined. The vertical velocity profile below 8.5 km is entirely negative (Fig. 32b) with increasing subsidence with height continuing well above the 5 km melting level. Both the stratiform regions of mature MCSs (Biggerstaff and Houze 1991) and the inner core stratiform region of Hurricane Alicia (Marks and Houze 1987; Fig. 23) display a mesoscale updraft above the melting level. Hence even the weakest reflectivity regions in the inner core of Isabel poorly fits the conceptual model of a stratiform region.

Chapter 7: Discussion and Conclusions

7.1 Rainband Kinematics

Unlike previous studies, a high temporal and spatial analysis of VRWs has been presented, assessing the kinematic structure of rainbands in Hurricanes Isabel, Frances, and Irene. The analysis of Hurricane Isabel was sufficient to examine the phase speed of the rainbands in azimuth and radius. The DDAs provided the means to elucidate several features of spiral rainbands that appear consistent across all TC cases and are similar to previous modeling work. Kinematically, Isabel and Irene yielded radial WN1 asymmetries in vertical velocity with an azimuthally oriented downdraft leading the azimuthally oriented updraft band. The analysis in Frances yielded more complex vertical velocity structures, likely associated with the stagnation of rainbands near a hypothetical stagnation radius. Generally situated approximately one quarter of a wavelength behind the updraft, all three cases displayed a vertical vorticity maximum that was azimuthally oriented along inner core spiral rainbands, similar to that of previous modeling works (Chen and Yau 2001; Wang 2002b,a; Franklin et al. 2006; Li

and Wang 2012) and observational work (Reasor et al. 2000). Convergence is seen leading the low-level vorticity maxima. At low levels, the convergence acted to enhance vorticity, which modified the VRW structures. In prior modeling studies, these vorticity filaments are convectively coupled to the spiral rainband convection. Vertical vorticity structures are found on the radially inward side of rainbands. The vorticity structures generally exist below 5-6 km (i.e. in the low and mid-troposophere) and were associated with bands of rising motion of a similar radial wavelength. While the vorticity structures were generally confined to the low and mid troposphere, the updrafts of the rainbands exhibited heights that extended upwards of 9 km, suggesting the presence of near-tropospherically deep convection. In a composite of aircraft observations of TCs, Rogers et al. (2012) demonstrated that the greatest variance in vertical mass transport is within the inner core. This composite observation is consistent with the deep vertical updraft-downdraft couplets sampled by the SMART radars and WSR-88Ds.

While the DDAs are useful for understanding the vorticity and vertical velocity structures of rainbands, the exact mechanism by which buoyant parcels are released is unclear. As shown in Hurricane Irene, the convergence between 0.5 and 3 km ARL and divergence above 3 km is driving the updraft. The updrafts were tilted both upwind in height and radially outward, consistent with azimuthal WN1 and WN2 VRWs. Chen and Yau (2001) and Wang (2002a) allude to frictional convergence and Ekman pumping in the boundary layer ahead of the PV maxima releasing buoyant parcels. Indeed, convergence is seen near the surface in all three cases within multiple rainbands, supporting their hypothesis. However, the boundary layer is not well resolved in any of the analyses presented. Thus, the presence of Ekman pumping cannot

be established. Mid-level divergence maxima associated with diabatic heating are seen in modeled rainbands (e.g. Li and Wang 2012), and divergence maxima are present in the observations presented here. Thus, it appears that a dynamic-thermodynamic feedback results in the vertical draft structure.

Nearly all of the VRWs seen here exhibit a radially outward tilt. Furthermore, the upwind-tilt of the rainbands seen in Hurricane Isabel is consistent with WN2 sheared VRWs, as in Reasor et al. (2000). However, WN1 VRWs exhibit a downwind tilted updraft in azimuth in the inner core (Wang 2002a). Near the eyewall, however, Wang (2002a) noted that WN1 VRWs exhibited the same upwind tilt as WN2 VRWs. The precipitation structure shown in Hurricane Irene in Fig. 4 is obviously WN1 in structure. A Fourier decomposition of reflectivity (Fig. 33) confirms this observation. Thus, the near-eyewall VRW examined in Chapter 5.3 exhibits the same characteristics as simulated by Wang (2002a). It is likely that the near eyewall VRWs affect the structure and intensity of TCs.

Overall, the kinematic structure of the rainbands observed here was consistent with that of previous modeling studies of VRWs. Thus, it appears that many of the inner core spiral rainbands were generated by VRWs. To further test this hypothesis, the propagation of these waves was compared to VRWs, inertia-gravity waves, and advection. The radial propagation of elongated vorticity maxima that were coupled with convective rainbands in Hurricane Isabel agreed well with the MK97 theoretical VRW phase speed. Moreover, the azimuthal propagation of vorticity bands was slower than that of the mean wind, confirming the low-level observations of Corbosiero et al. (2006). Although Moon and Nolan (2015) showed that VRWs may not be responsible

for the rainbands in their numerical simulations, the observations here show otherwise. Indeed, the Hovmoller diagram presented in Fig. 15 shows that the vorticity maxima are propagating radially outward slowly and were not being advected at the same rate as the tangential flow (Fig. 16). This observation eliminates the possibility that the rainbands were associated with inertia-gravity waves, either inward or outward propagating. Nevertheless, the existence of inertia-gravity waves or advection processes within the inner core is not being contested. Other mechanisms by themselves do not appear to be dominant forcing mechanisms for the inner rainbands observed in Isabel, Frances, or Irene. Instability may be released due to other types of waves (i.e. gravity waves) that are generated within the inner core environment. A combination of influences on the generation of spiral rainbands may exist in the same environment through which VRWs are propagating. In addition, the advection of convective clouds may also be possible, giving rise to rainband-like structures. However, the SMART radars within the inner core regions sampled did not observe these features.

7.2 Inner Core Precipitation

The analyses presented in Chapter 6 do not follow the accepted conceptual inner core model of stratiform precipitation structure. The classification of inner core reflectivity reveals that most echoes are convective, even in regions of weak low-level reflectivity. This strongly deviates from the current conceptual model in which the inner core region is supposedly seeded by hydrometeors advected radially outward from the eyewall.

The kinematic structure of VRWs indicates the presence rainbands associated with deep convective updrafts within the inner core of three landfalling TCs. These VRWs appear to be dominating the precipitation processes within the inner core region. The sharp decrease in reflectivity contours in CFADs (Fig. 26) indicative of stratiform precipitation is likely the result of the weakness of the vertical drafts associated with VRWs ($w < 5$ m s^{-1}). Graupel (i.e. rimed ice particles) can be generated by convection with vertical velocities of at least 2-3 m s^{-1}. At mid-levels, however, graupel fall speeds approach 5 m s^{-1} (Böhm 1989). As the updrafts in this study are at maximum 3-5 m s^{-1}, the majority of the updraft area cannot support graupel. Thus, reflectivities would be expected to be weak aloft given the lack of significant riming.

The DDA regions sampled within the inner core represent a limited extent of the entire inner core, and were much smaller than even the regions included in the CFADs. However, the DDAs verified to the results attained the reflectivity-based classification. Unlike stratiform regions that are characterized by a mesoscale downdraft near and beneath the radar bright band and a mesoscale updraft above the radar bright band (e.g. Biggerstaff and Houze 1991), the inner cores of the hurricanes examined here exhibited structure more consistent with just convection. Even the weaker reflectivity areas had sinking motion surrounding the tropospherically deep mesoscale updrafts associated with VRWs with no presence of a bright band (e.g. see the vertical cross-section in Fig. 13 which shows no resemblance of a bright band surrounding the VRW) or a mesoscale updraft aloft. Other TC inner cores with limited rainbands may more strongly resemble stratiform precipitation. However, for these three cases it is concluded that the inner core is predominantly convective.

Given this sharp deviation from a previously conceived stratiform inner core, the question arises whether latent heating profiles are being underestimated in TCs. For example, TRMM retrievals of latent heating rely on a 4.3 km horizontal resolution retrieval of rainfall (Kummerow et al. 1998). The analysis of VRW induced rainbands at 1 km (Isabel and Frances) and 0.5 km (Irene) reveal the complexity of the precipitation structure of rainbands. In addition, this analysis confirms the radial extent of these structures is on the order of 5-10 km, which TRMM instruments may have difficulty resolving in TCs. Given the prevailing stratiform model of the inner core, it is unlikely that the latent heating associated with VRW convection in the inner core is adequately represented. The latent heating associated with VRW induced rainbands may influence both the intensity and structure of mature TCs and should be examined in future work.

7.3 Conceptual Models

As the work presented in this study suggests significant variation from the currently prescribed conceptual model of the inner core of TCs, it is necessary to present a new conceptual model based on the findings herein. Fig. 34 shows Fig. 9 from Marks and Houze (1987), which is a conceptual model of the inner core region of Hurricane Alica (1983). The conceptual model demonstrates the stratiform nature of the inner core, and is supported by Houze (2010) and Rogers et al. (2012) as the current conceptual model of inner core precipitation. As convection in the eyewall generates ice particles above the freezing level, their terminal velocities are too weak to fall through the strong updrafts. Thus, they are size sorted and small ice particles are advected

radially outward from the eyewall by the secondary circulation of the TC. As they grow, they overcome the weak rising motion associated the mesoscale updraft above the melting level of the inner core. Thus, the model shows a stratiform region of precipitation is found in the inner core with little contribution to total rainfall from the collision-coalescence process in rainbands.

However, as shown from the kinematic structure of rainbands in the inner core of three tropical cyclones, asymmetries in vertical velocity are associated with deep convection, extending upwards of 9 km in some cases. The vertical drafts of this convection seem to be relatively weak (3-5 m s^{-1}), but support the growth of hydrometeors by collision-coalescence. As the reflectivity structure within rainbands exhibits little resemblance to a typical stratiform structure (i.e. the presence of a radar bright band), it can be inferred low-level precipitation maxima are likely grown by warm-rain processes (i.e. collision-coalescence). In Figs. 13, 14, 18, 21, 22, it is seen that the strongest horizontal divergence is just above the maximum in vertical velocity, which suggests the divergence of hydrometeors in this region (near the melting level). As demonstrated by the vertical, overturning circulation, a hydrometeor likely takes a path toward the radially outward downdraft as it moves tangentially along the rainband. As the hydrometeor moves across the gradient in vertical velocity between the updraft and downdraft, its terminal velocity exceeds the upward velocity and falls to the surface. As reflectivity increases downward between the updraft and the downdraft with little indication of a bright band, this indicates a convective, warm-rain process, rather than a stratiform, ice process.

As suggested by the plots of divergence, hydrometeors are diverging in the updraft, suggesting that some hydrometeors may be advected radially away from the band. This process likely is the result of small droplets or ice crystals grown near and above the freezing level grown in the deep, but weak, updraft. For example, a downdraft can been seen radially inward of the periphery of the rainband shown in Fig. 14 during the landfall of Hurricane Isabel. Deep divergence associated with the rainband updraft on the radially inward side of the rainband indicates that hydrometeors may be being advected radially inwards into the region surrounding the primary rainband. Thus, it appears plausible that VRW rainbands are at least partially responsible for the non-convective region with small ice crystals that are grown in the convective updrafts of the rainbands, but are too small to fall out within the convection itself. However, given the presence of the deep downdrafts surrounding radially inward and outward of rainbands, aggregates may not be given sufficient time in which to grow before melting such that a bright band signature is produced. This may explain the lack of a radar bright band in these regions.

Summarizing these new observations, a new conceptual model of VRW-induced rainbands is presented in Fig. 35. This model deviates from the current, leading conceptual model of the inner core, in that ground-based radar observations of three separate TCs indicate the presence of deep convection within the inner core. The propagation of VRWs into the inner core region likely acts to oppose the boundary layer inflow, initiating frictional convergence within the boundary layer of a TC. As the updraft initiated in the boundary layer grows, compensating downdrafts are induced radially inwards and outward of the updraft. Size sorting in the mid-troposphere grows

falling drops between the updraft and downdraft by collision-coalescence. The divergence of hydrometeors out of the updraft likely results in the fallout of remaining hydrometeors in the regions surrounding rainbands. Thus, these low reflectivity areas are the result of convection, rather than stratiform processes and are more closely tied to convectively coupled VRWs rather than the eyewall ejection of hydrometeors..

7.4 Future Work

Additional questions arise as a result of this study. The structure of rainbands appears consistent across multiple cases and are consistent with VRW theory. But, it is unclear how the environmental shear in which each TC was embedded affects the growth and decay of the rainbands. As shown in Li (2016), formation mechanisms of rainbands in the inner core may depend on their location relative to the TC shear vector. Their work demonstrated convection forced by downdrafts in the upshear region of TCs could be advected cyclonically around the TC, resulting in a rainband structure. This may be similar to the mechanism such as that shown by Moon and Nolan (2015), revealing the possibility that rainbands may be formed by mechanisms other than only VRWs.

While this study was able to assess the kinematic structure of VRW-induced rainbands, the thermodynamic structure of VRWs was not assessed. Future observations of the thermodynamics of rainbands may reveal the effects of baroclinicity upon rainband structure and evolution. Such baroclinic effects may be the result of the transition between sea and land. Curry (2010) showed that a baroclinic zone was present during the onshore transition of Hurricane Isabel, affecting its evolution and structure.

However, the effect of this boundary on rainbands was not assessed. Boundary layer differences across the land-sea interface (e.g. Knupp et al. 2006) may influence the structure and intensity of spiral rainbands, and may feedback on the TC as a whole as it makes landfall.

Furthermore, the role of VRWs in intensity changes has yet to be examined. As discussed in Chapter 1, the confirmation of VRWs in the inner core implies that substantial feedbacks on TC intensity may exist. The dynamic response of the TC to the presence of deep convection within the inner core needs to be examined in addition to the kinematic and thermodynamic structure of VRW-mean flow interactions near the RMW. This will be important in understanding the shortcomings of numerical modeling. Observations of this process may increase the confidence in intensity changes and the rapid intensification process (Rogers et al. 2012). As noted in Rogers et al., high resolution observations of the inner core are difficult to ascertain, but the SMART radars, other research grade radar observations, and in situ thermodynamic observations (Halverson et al. 2006; Naftel 2009) will be key in the future to deducing structure and intensity changes of TCs.

Table 1. SMART radar details are listed below including the frequency, antenna diameter, half-power beam width, peak power, and moments collected.

Radar	Frequency	Antenna Diameter	Beam Width	Peak Power	Moments
SMART Radar 1	5635 MHz	2.54 m	1.5°	250 kW	Z_H, V_R, SW
SMART Radar 2	5612.82 MHz	2.54 m	1.5°	250 kW	Z_H, V_R, SW
SMART Radar 2 (Polarimetric)	5624.57 MHz	2.54 m	1.5°	300 kW (150 each channel)	Z_H, V_R, SW, Z_{DR}, ϕ_{DP}, ρ_{HV}

Table 2. SMART radar and WSR-88D scan strategy details in Hurricanes Isabel, Frances, and Irene. The strategy name is listed with a hurricane descriptor (Isabel = IS, Frances = FR, and Irene = IR), a volume type (360° Volume = 360, Sector Volume = Sector), and a radar (SMART radar 1 or 2 = S, WSR-88D = W). Elevation angles are listed with elevations in parentheses indicating those that were different in the SMART radar 2 scanning strategy. Finally, the effective Nyquist Velocity and gate spacing are listed for each strategy. WSR-88D Nyquist velocities are listed for the lowest elevation only.

Hurricane	Strategy Name	Elevations (°)	Nyquist Velocity	Gate Spacing
Isabel	IS360S	0.8(1.0), 1.5, 2.3, 3.2, 4.3, 5.4, 6.8, 8.4, 10.2, 12.2, 14.5, 17.1, 20.2, 23.2, 26.9, 30.5, 34.6	±20.0 m s^{-1}	67 m
Isabel	ISSectorS	0.8(1.0), 1.5, 2.3, 3.2, 4.3, 5.4, 6.9, 8.7, 10.8, 13.2, 15.9, 18.9, 22.2, 25.7, 29.2, 32.7	±20.0 m s^{-1}	67 m
Frances	FR360S	0.8, 1.5, 2.2, 3.0, 4.0, 5.2, 6.5, 7.9, 9.5, 11.2, 13.1, 15.1, 17.5, 20.0, 23.0, 27.0, 32.0, 38.0	±34.0 m s^{-1}	67 m
Frances	FR360W	1.5, 2.4, 3.3, 4.3, 6.0, 9.9, 14.6, 19.5	±34.5 m s^{-1}	260 m
Irene	IR360S	0.8, 1.5, 2.2, 2.9, 3.6, 4.3, 5.3, 6.3, 7.3, 8.3, 9.5, 10.7, 12.0, 13.5, 15.0, 16.5, 18.0, 19.5	±48.0 m s^{-1}	75 m
Irene	IR360W	0.5, 0.9, 1.3, 1.8, 2.4, 3.1, 4.0, 5.1, 6.4, 8.0, 10.0, 12.5, 15.6, 19.5	±29.7 m s^{-1}	260 m

Table 3. Dual-Doppler domain details and radar pairs used in each hurricane case. The radar used as the origin of the domain is listed under "Radar 1" with the other radar listed under "Radar 2." In addition, the grid specifications including size and shape are listed. Finally, the baseline distance between the dual-Doppler pairs is listed.

Hurricane	Radar 1	Radar 2	Δx, Δz (km)	*xmin*, *ymin*, *zmin* (km)	x, y, & z Dimensions	Baseline (km)
Isabel	SMART Radar 2	SMART Radar 1	1.0, 1.0	0, -40, 0.5	100, 134, 15	52.2
Frances	KMLB	SMART Radar 2	1.0, 1.0	0, -50, 0.5	110, 110, 10	46.6
Irene	KMHX	SMART Radar 2	0.5, 0.5	-25, -5, 0.5	140, 140, 15	20.1

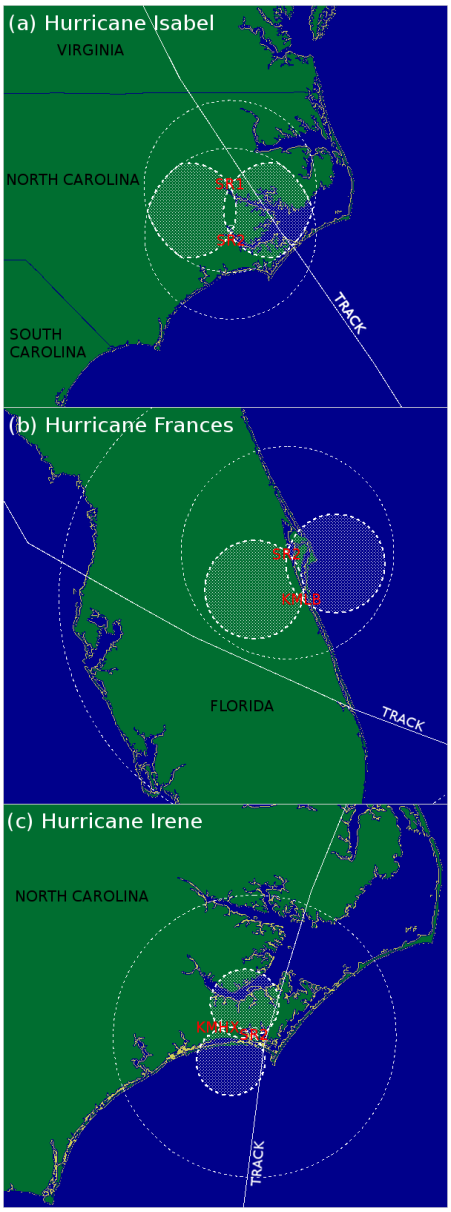


Fig. 1. Dual-Doppler domains for each SMART radar deployment. The hatched white area in each figure represents the 30° lobe. Radar positions are labeled in red. Dual-Doppler pairs include SMART radars 1 and 2 during Hurricane Isabel (a), SMART radar 2 and KMLB during Hurricane Frances (b), and SMART radar 2 and KMHX during Hurricane Irene (c).

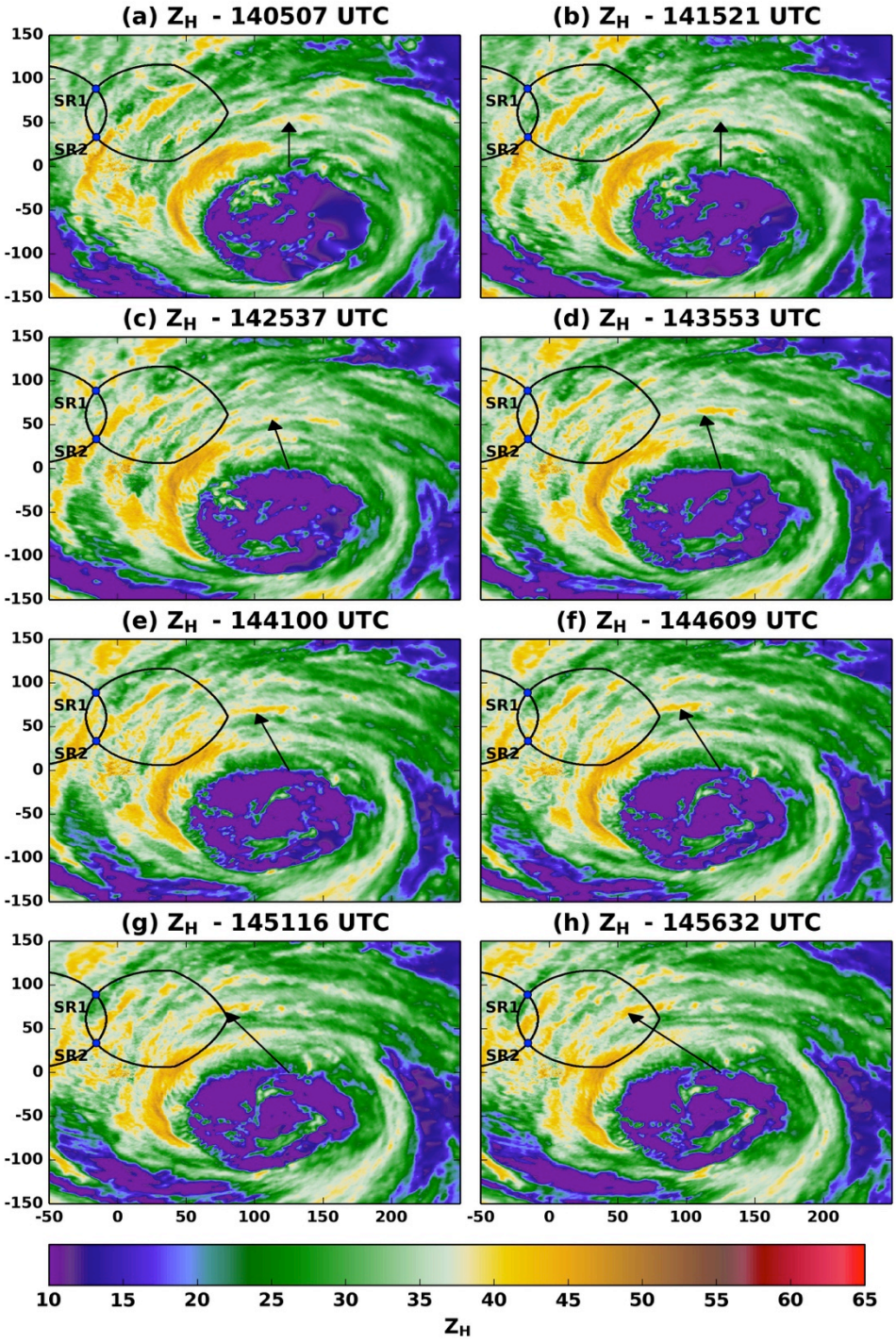


Fig. 2. Time series of KMHX 0.5° Z_H during Hurricane Isabel. The filled contours represent radar reflectivity in dBZ, the solid black line represents the 30° dual-Doppler lobes, and locations of SMART radars 1 and 2 are indicated by the blue dots. KMHX is located at the origin. The arrows identify a rainband's origin near the eyewall, propagating outward into the inner core.

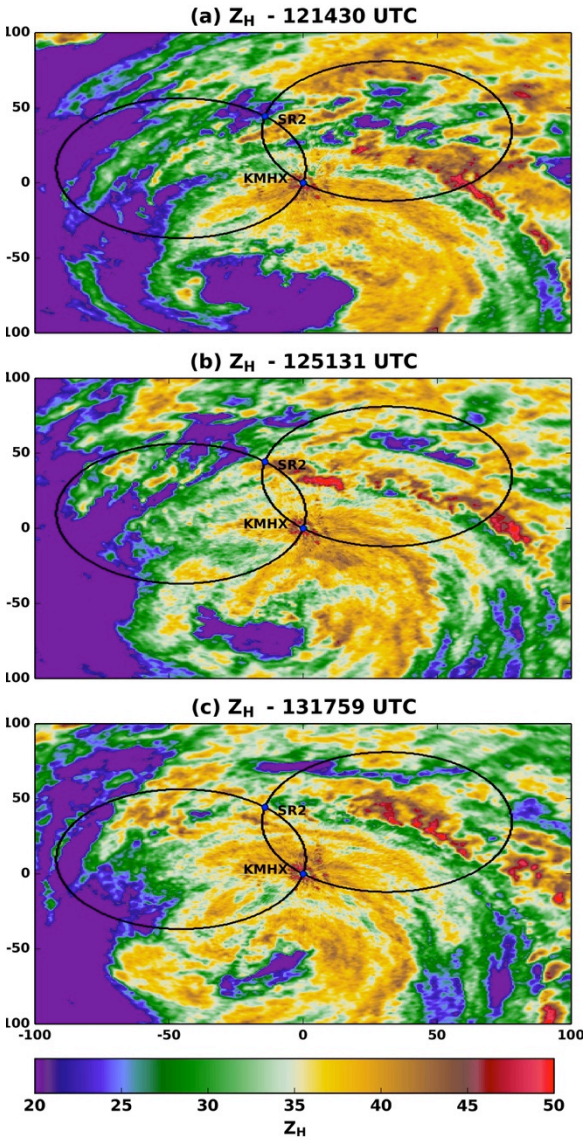


Fig. 3. As in Fig. 2, but for the landfall of Hurricane Frances. The radar at the origin is KMLB.

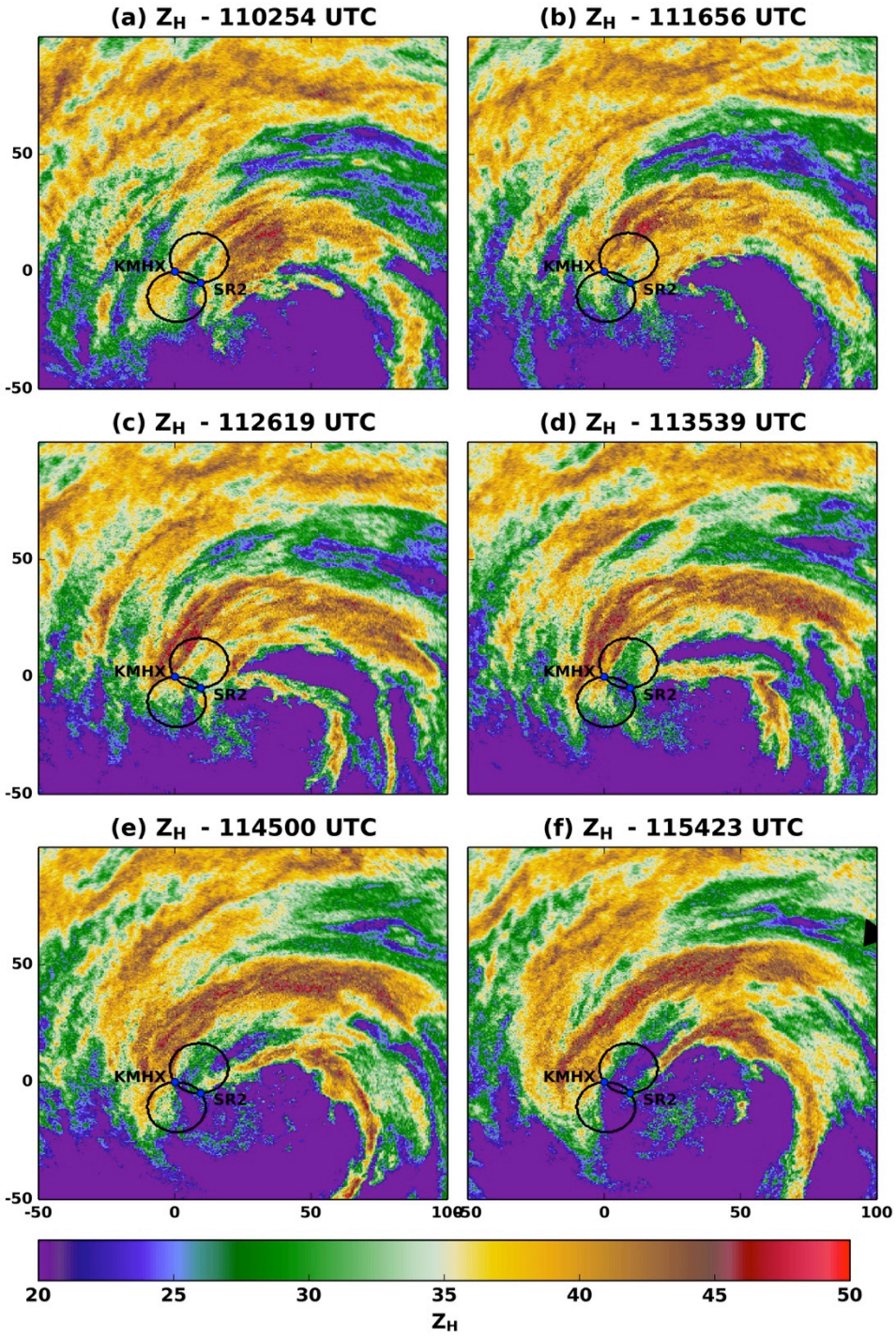


Fig. 4. As in Fig. 3, but for the landfall of Hurricane Irene. The radar centered at the origin is KMHX.

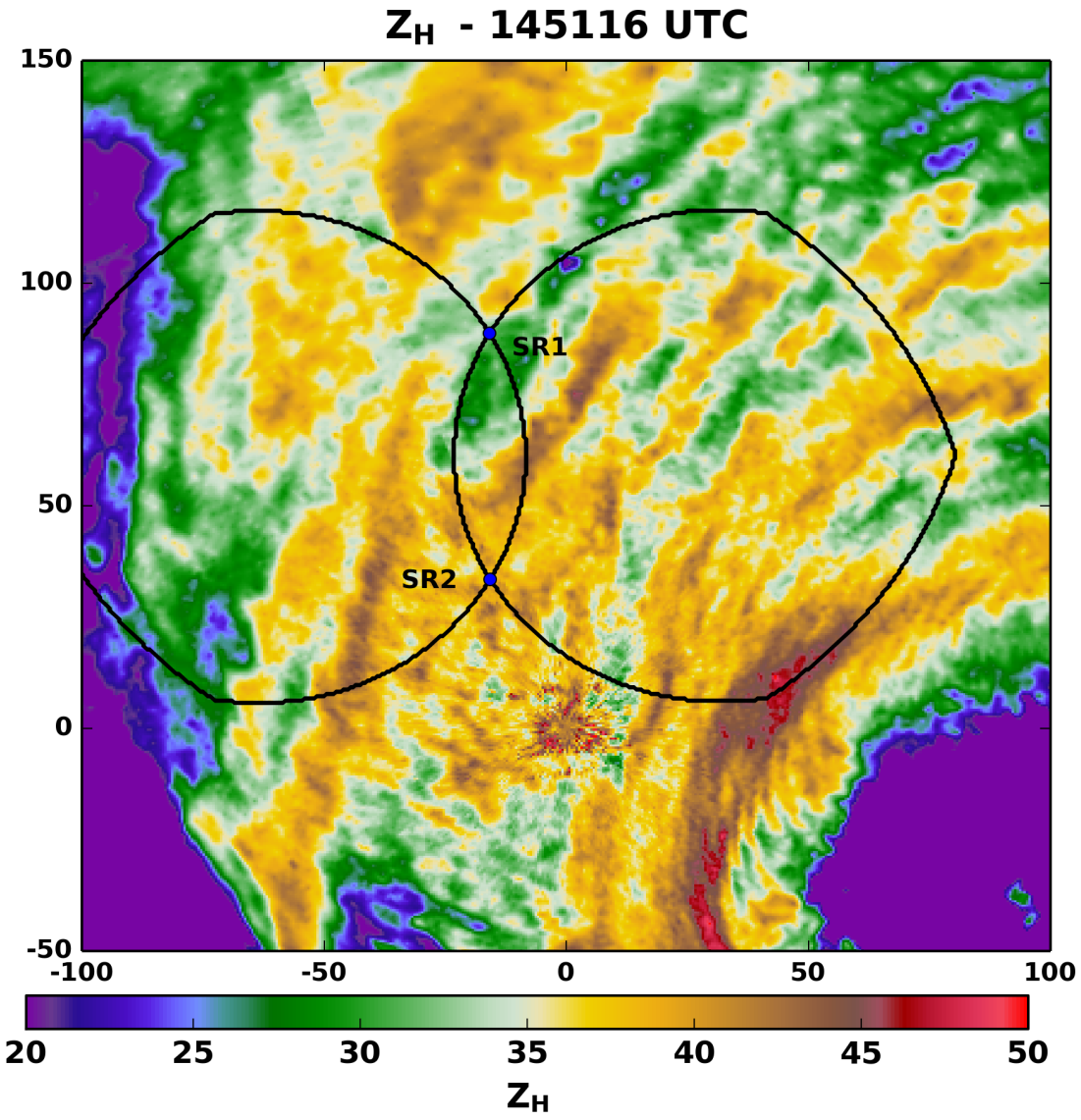


Fig. 5. Plan view of Z_H from KMHX (located at the origin). The black lines are as in Fig. 2 with the locations of the SMART radars indicated by the blue points labeled "SR1" and "SR2."

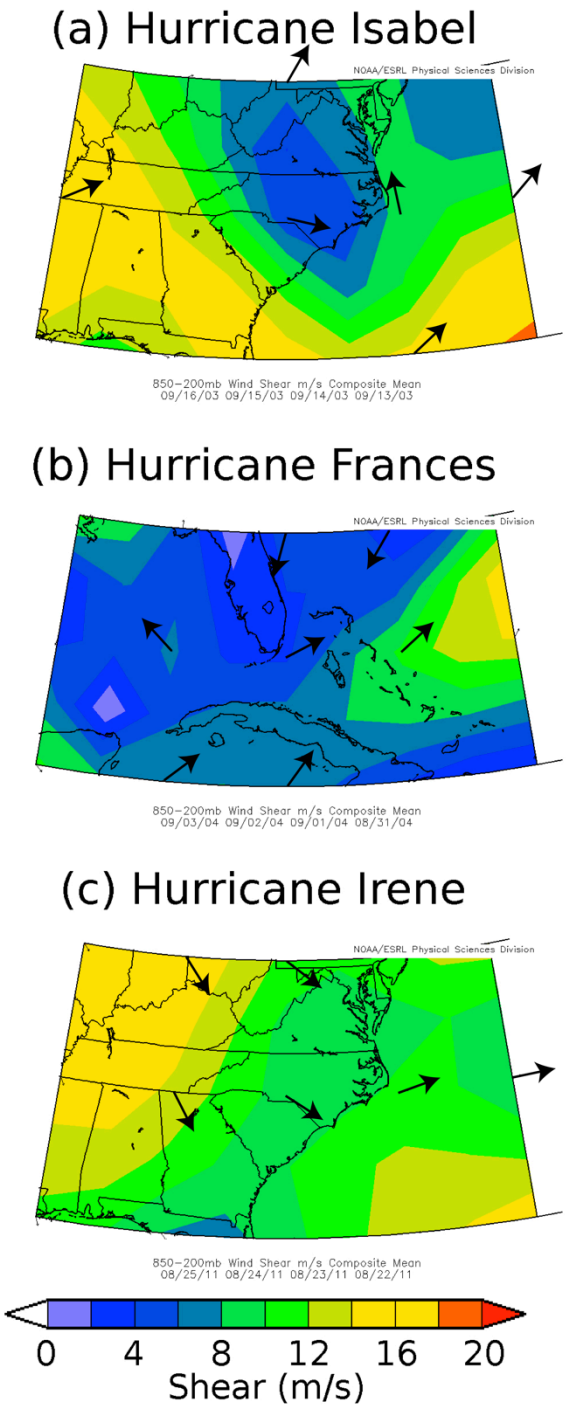


Fig. 6. Shear magnitude (colored contours) and direction (arrows), showing the 4 day mean 200-850 hPa shear beginning six days prior to hurricane landfall through two days prior to landfall. Plots are shown individually for Hurricanes Isabel (a), Frances (b), and Irene (c).

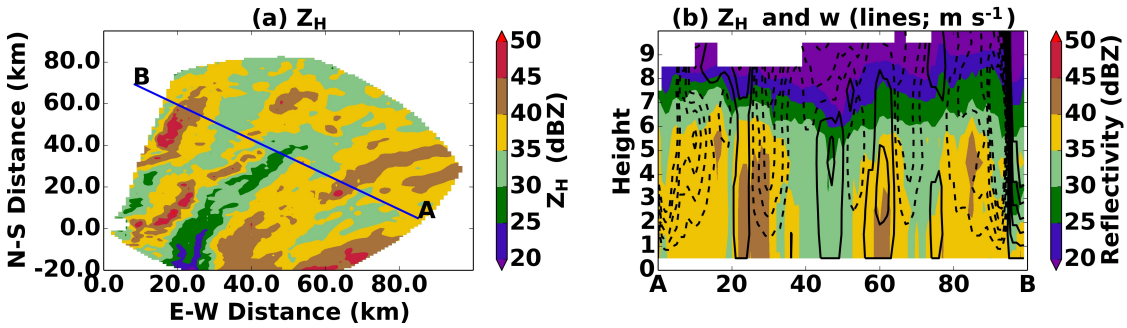


Fig. 7. Vertical cross section through the 1456 UTC dual-Doppler analysis of Hurricane Isabel. (a) Reflectivity is color contoured and the blue line labeled "A" and "B" at both ends represents the region through which the vertical cross section in (b) is taken. (b) Reflectivity is contoured along the cross section and height plane. Vertical velocity is contoured every 1 m s^{-1} with the 0 m s^{-1} represented by the first solid contour. Positive values are solid lines and negative values are dashed.

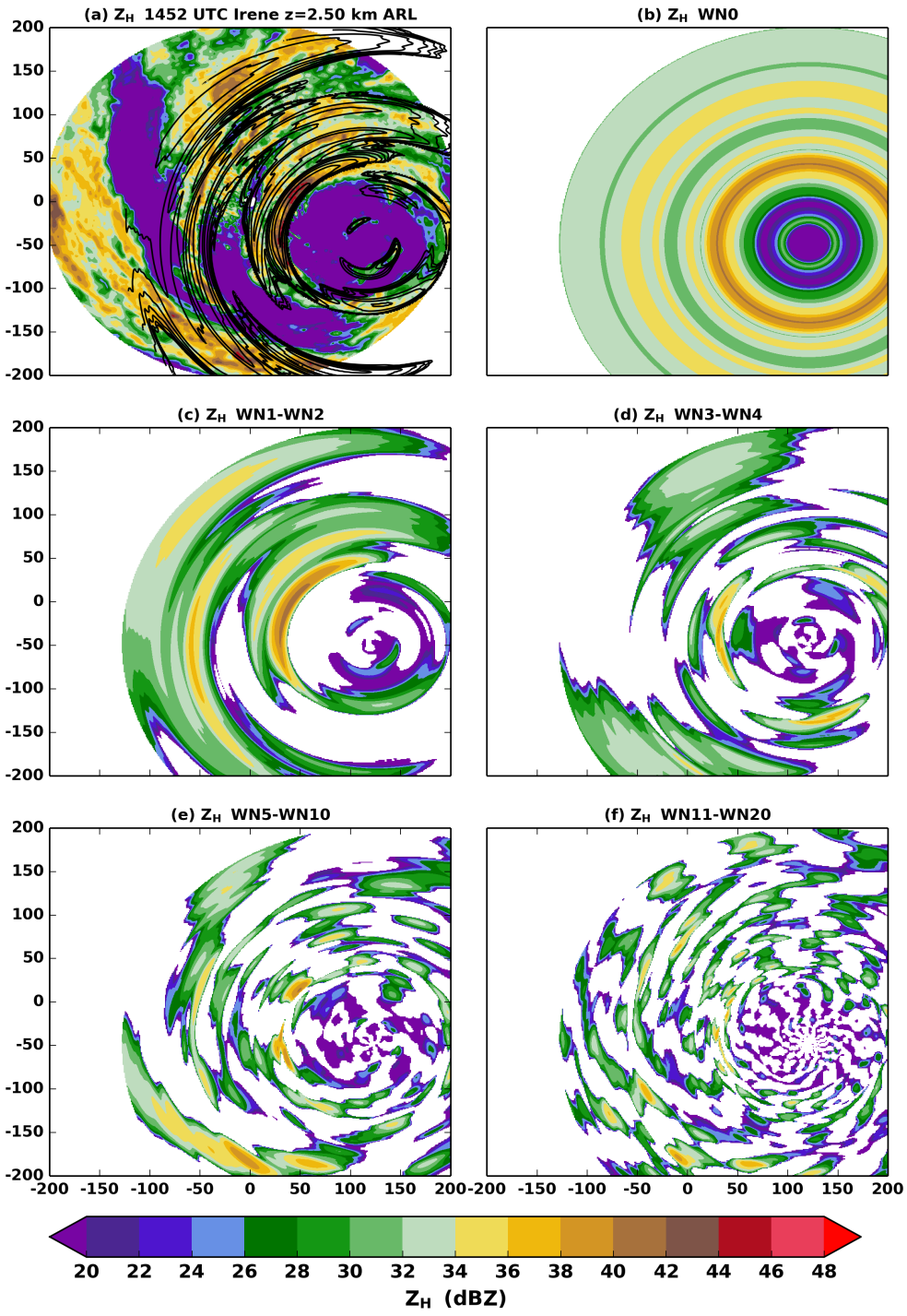


Fig. 8. Fourier decomposition of Z_H. (a) The total reflectivity is color contoured with sum of WN1 and WN2 components overlaid every 2 dB beginning with 20 dBZ. (b) The symmetric component of Z_H (WN0) is shown. (c) The sum of the WN1 and WN2 components of Z_H is displayed. (d) As in (c), but for the sum of WN3 and WN4 components. (e) As in (c), but for the WN5 through WN10 components. (f) As in (c), but for the WN11-WN20 components.

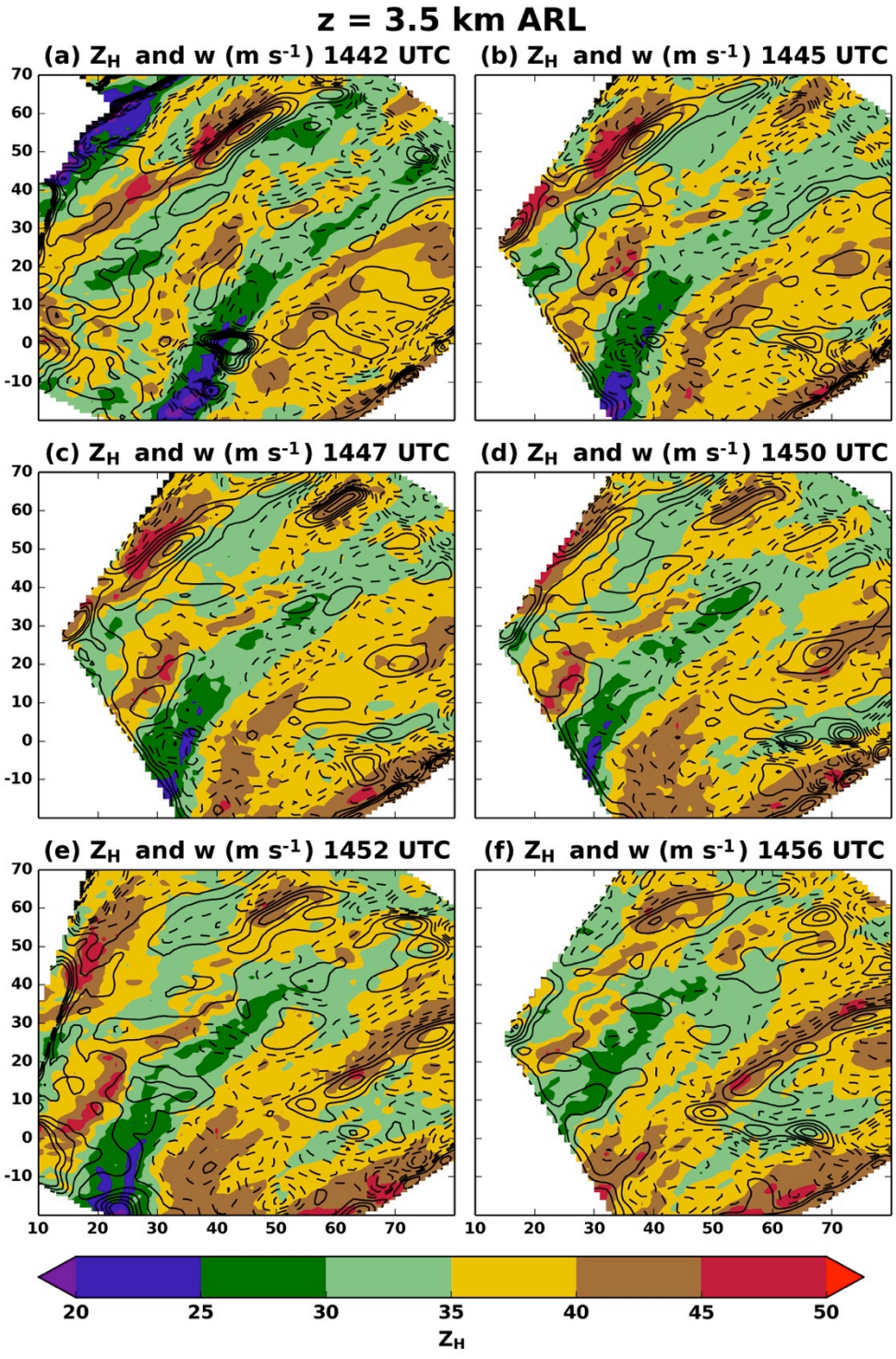


Fig. 9. Dual-Doppler analyses between 1440 UTC and 1500 UTC. Individual analysis times are shown above each plot. The filled contours represent the maximum radar reflectivity at the z = 3.5 km ARL analysis level. The black contours represent vertical velocity w every 0.5 m s^{-1}. The dashed contours represent $w < 0$ m s^{-1}, and the solid contours represent $w \geq 0$ m s^{-1}.

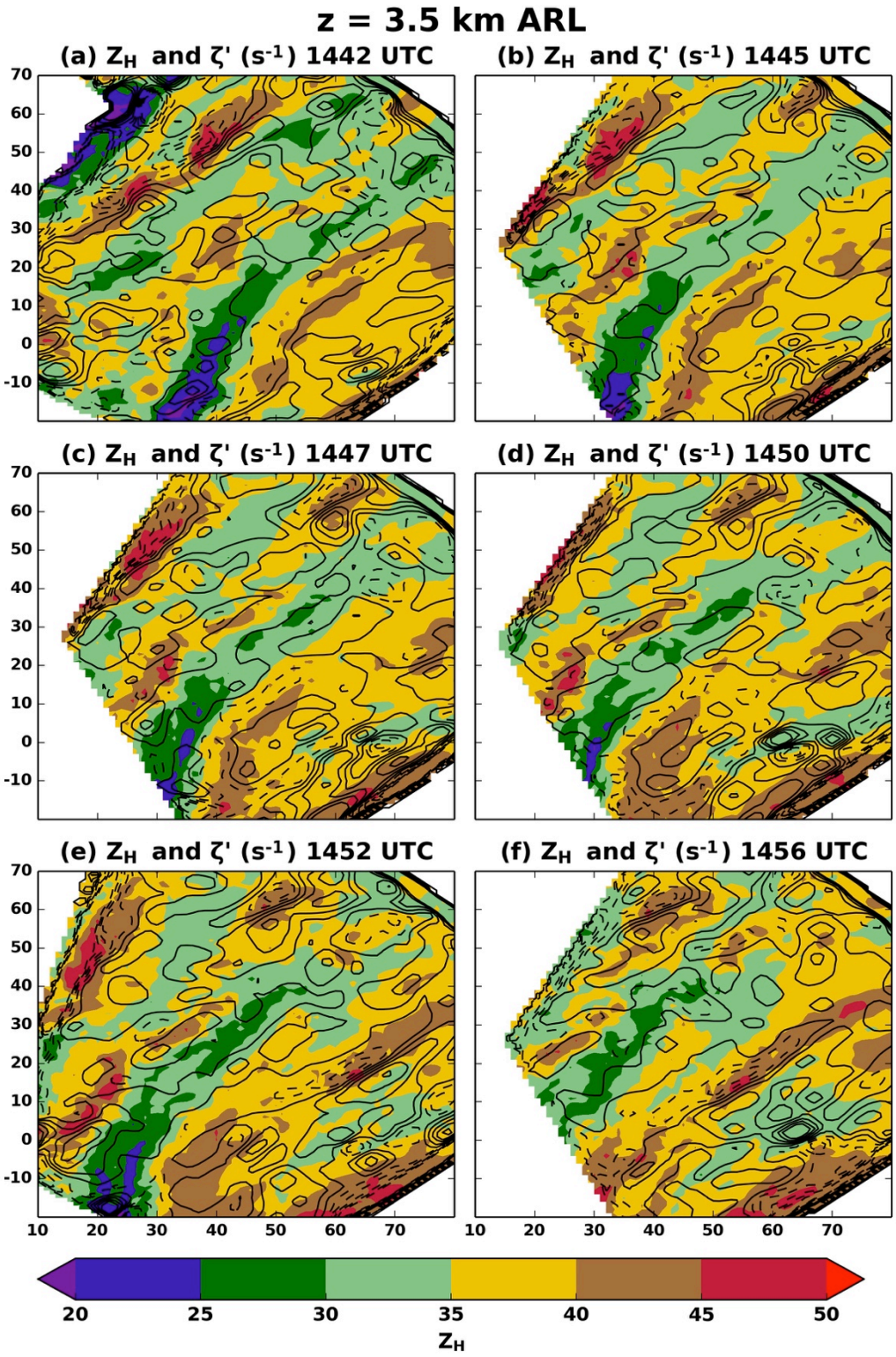


Fig. 10. As in Fig. 9, but the black contours are ζ ' every 4 ×10^{-4} s^{-1}. In this figure, the 0 s^{-1} line is omitted.

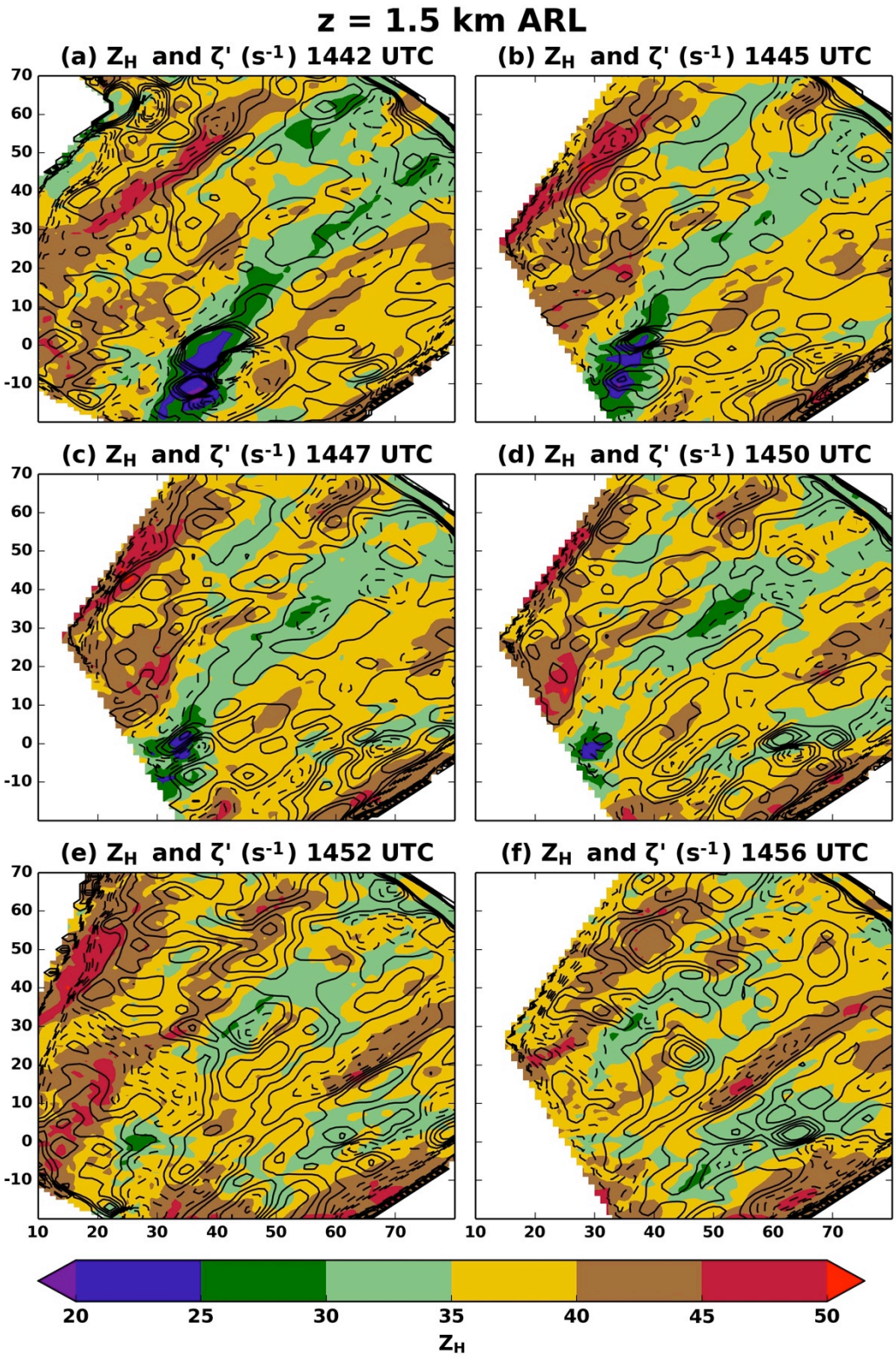


Fig. 11. As in Fig. 10, but for the 1.5 km ARL analysis level.

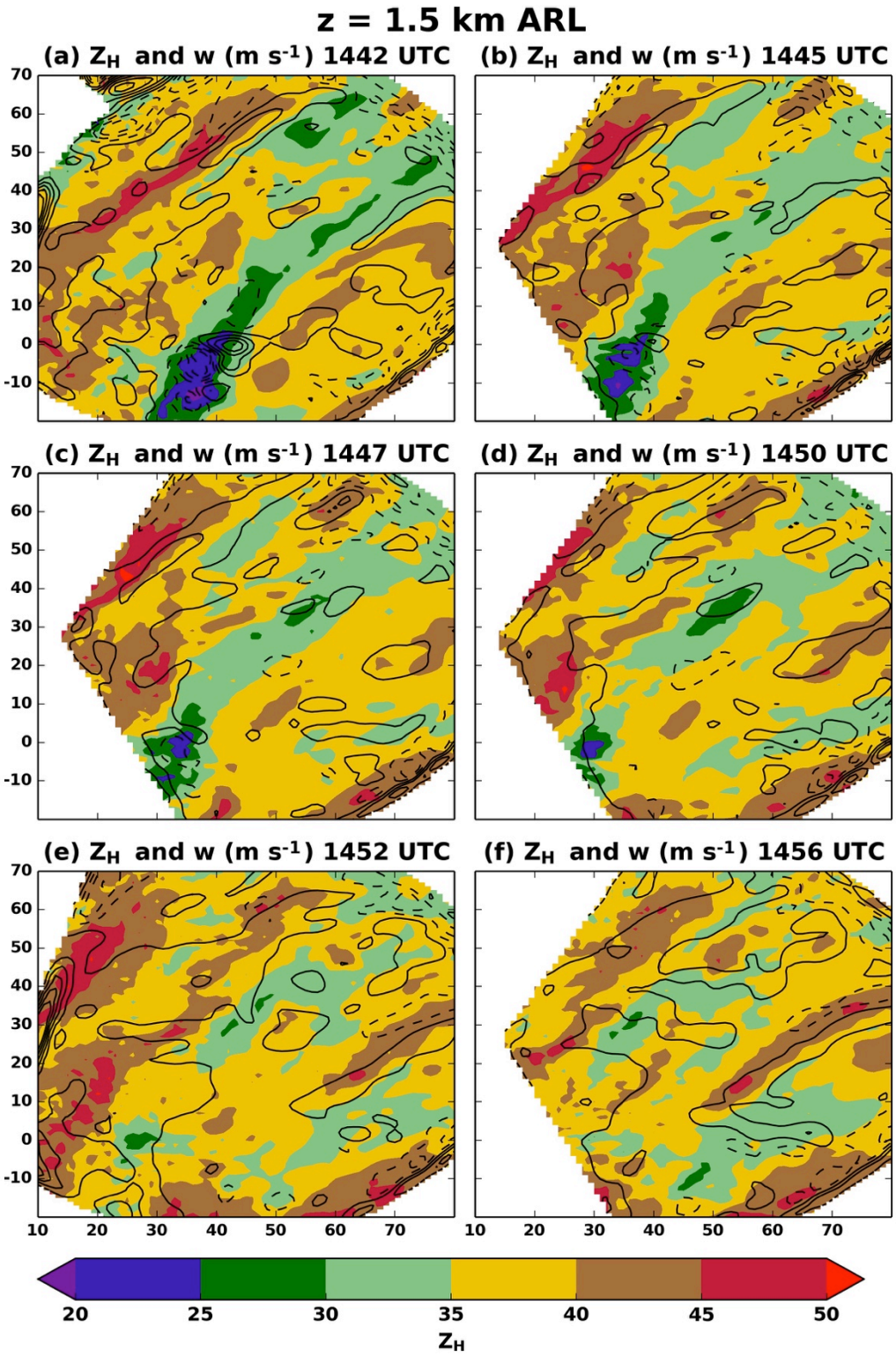


Fig. 12. As in Fig. 9, but for the 1.5 km ARL analysis level.

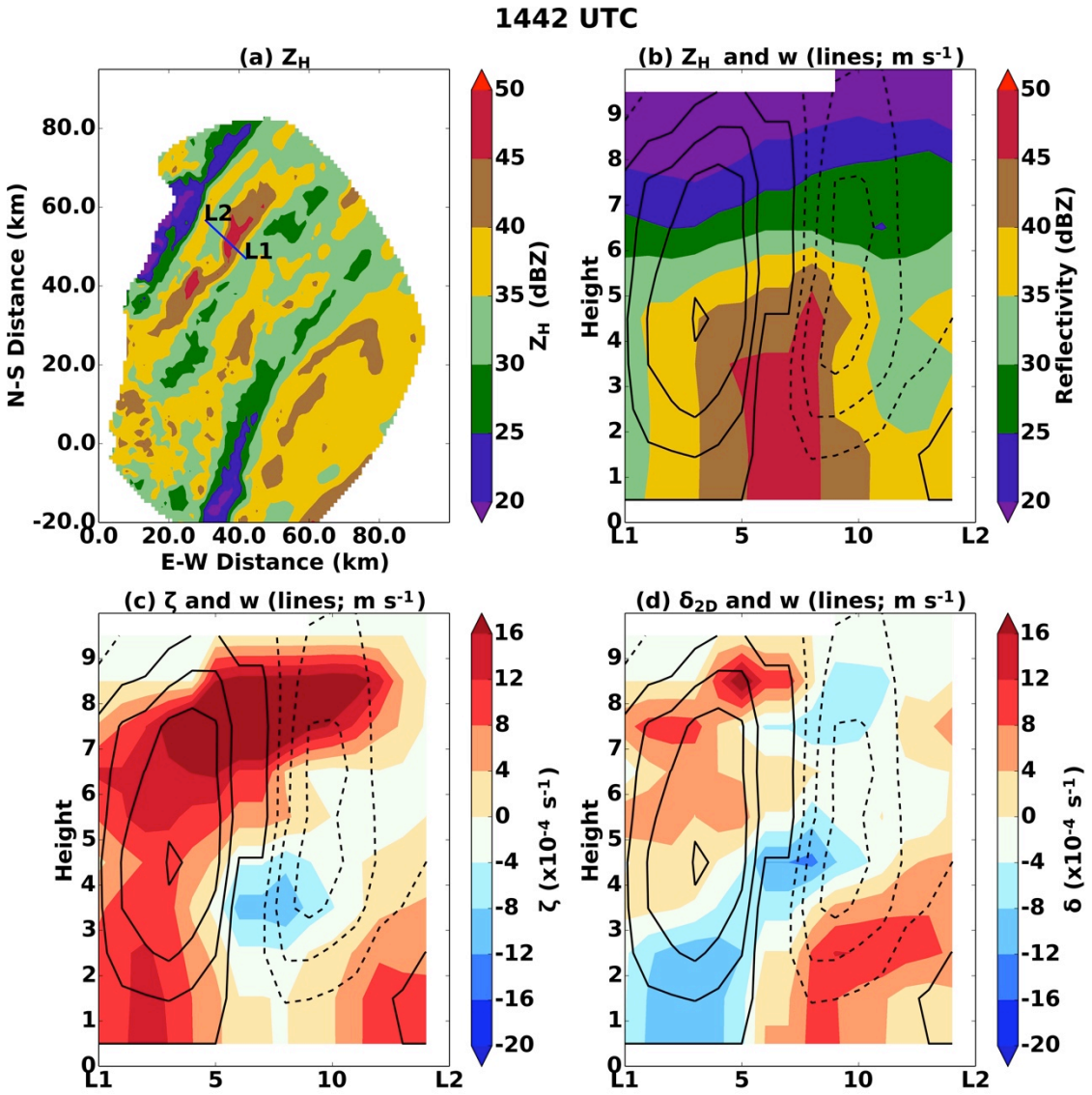


Fig. 13. The vertical cross section indicated by the line L1-L2 in (a) is shown for the 1442 UTC DDA. (a) Z_H is contoured at the 1.5 km ARL level with the blue line indicating the position of the vertical cross section. (b) Reflectivity is contoured in the vertical cross section, and contours (black) of vertical velocity are shown every 1 m s^{-1} with the first solid line being 0 m s^{-1}. (c) As in (b), but the filled contours display vertical vorticity ζ. (d) As in (c), but the filled contours indicate the magnitude of horizontal divergence δ_{2D}.

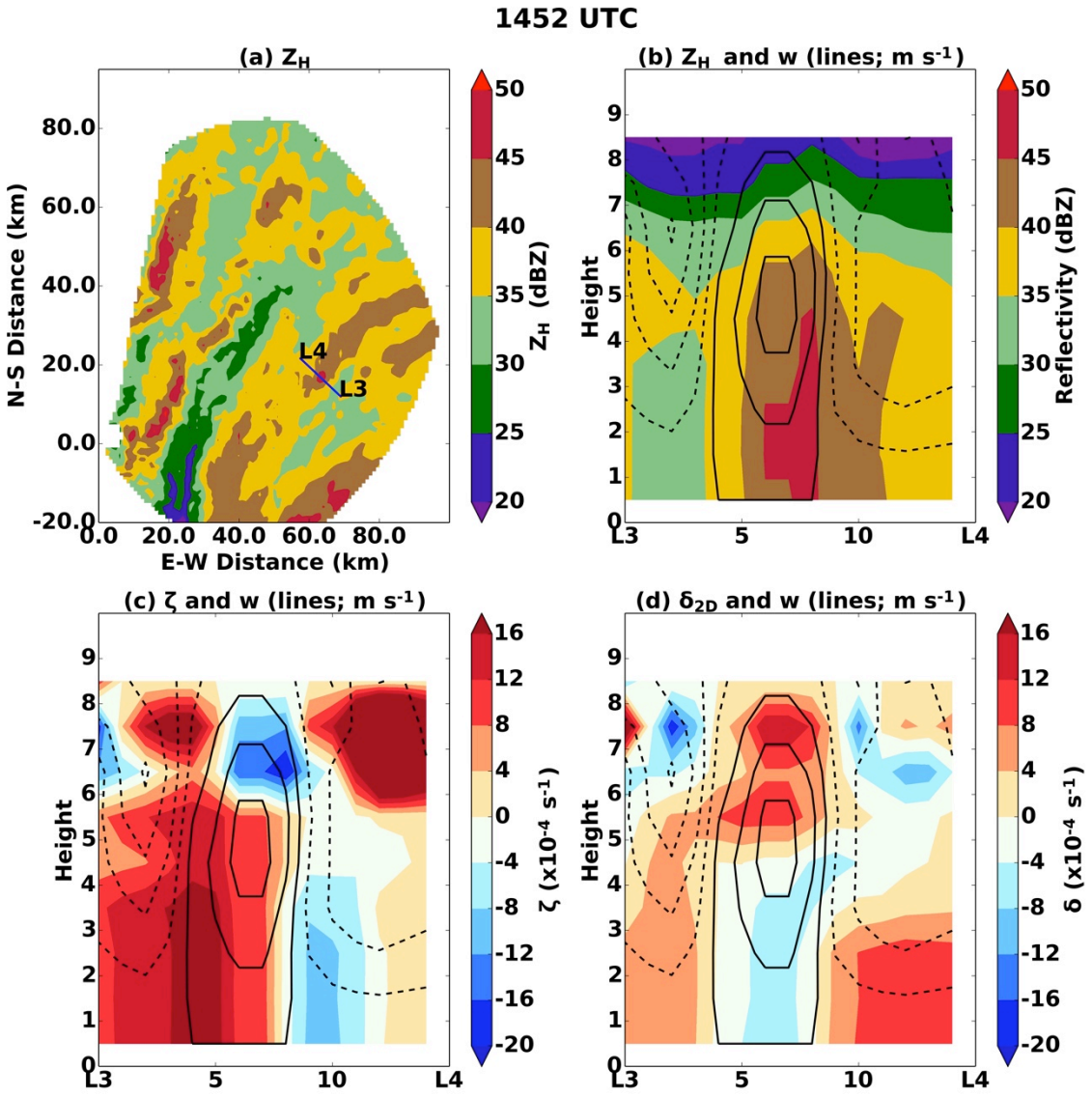


Fig. 14. As in Fig. 13, but for the 1452 UTC DDA through the line L3-L4.

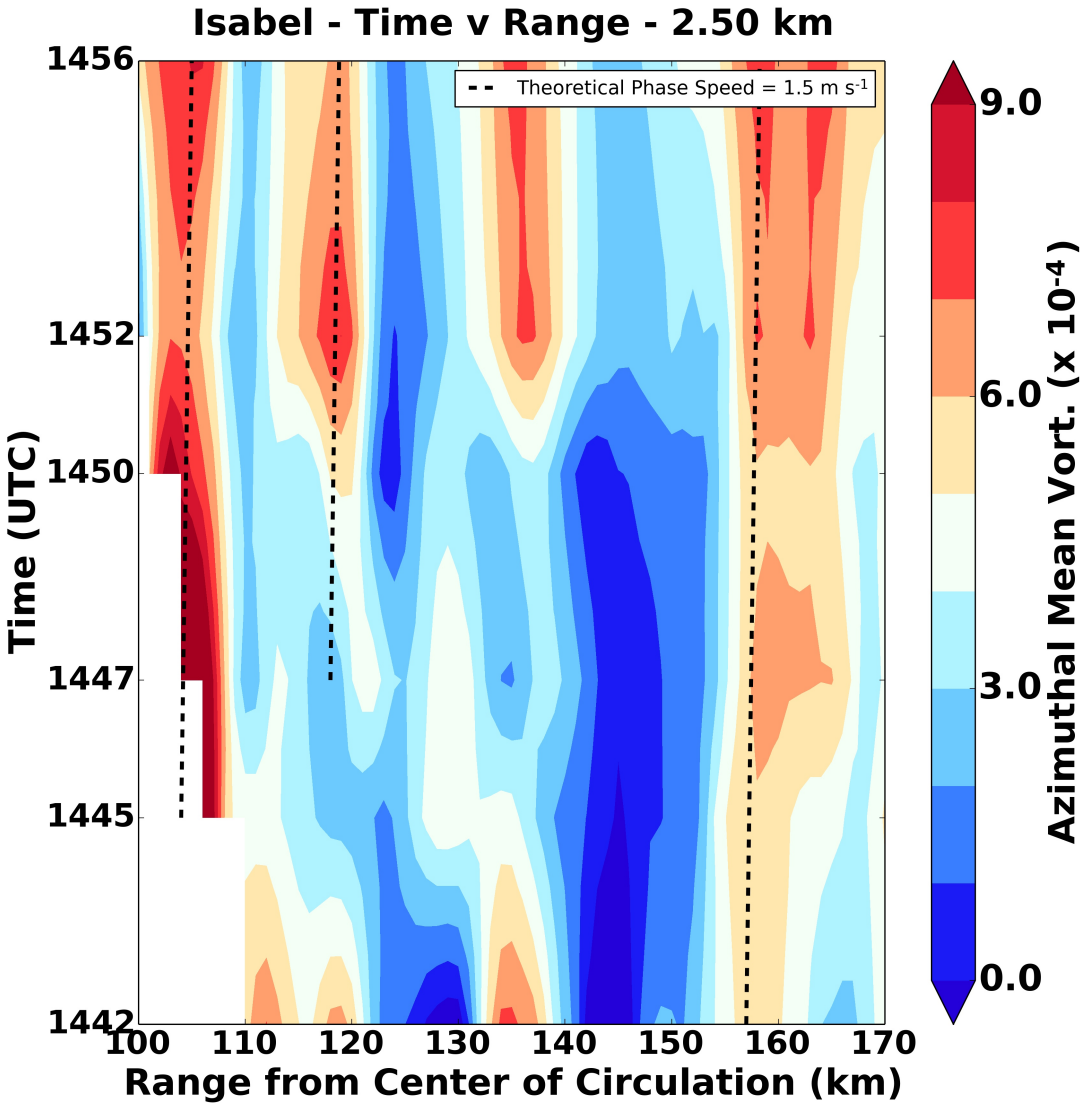


Fig. 15. Shown is a diagram similar to a Hovmoller diagram, except time is increasing in the positive y-direction. The filled contours represent the mean vertical vorticity in azimuth as a function of radius from the center of circulation. The dashed lines represent a hypothetical phase speed of 1.5 m s^{-1}.

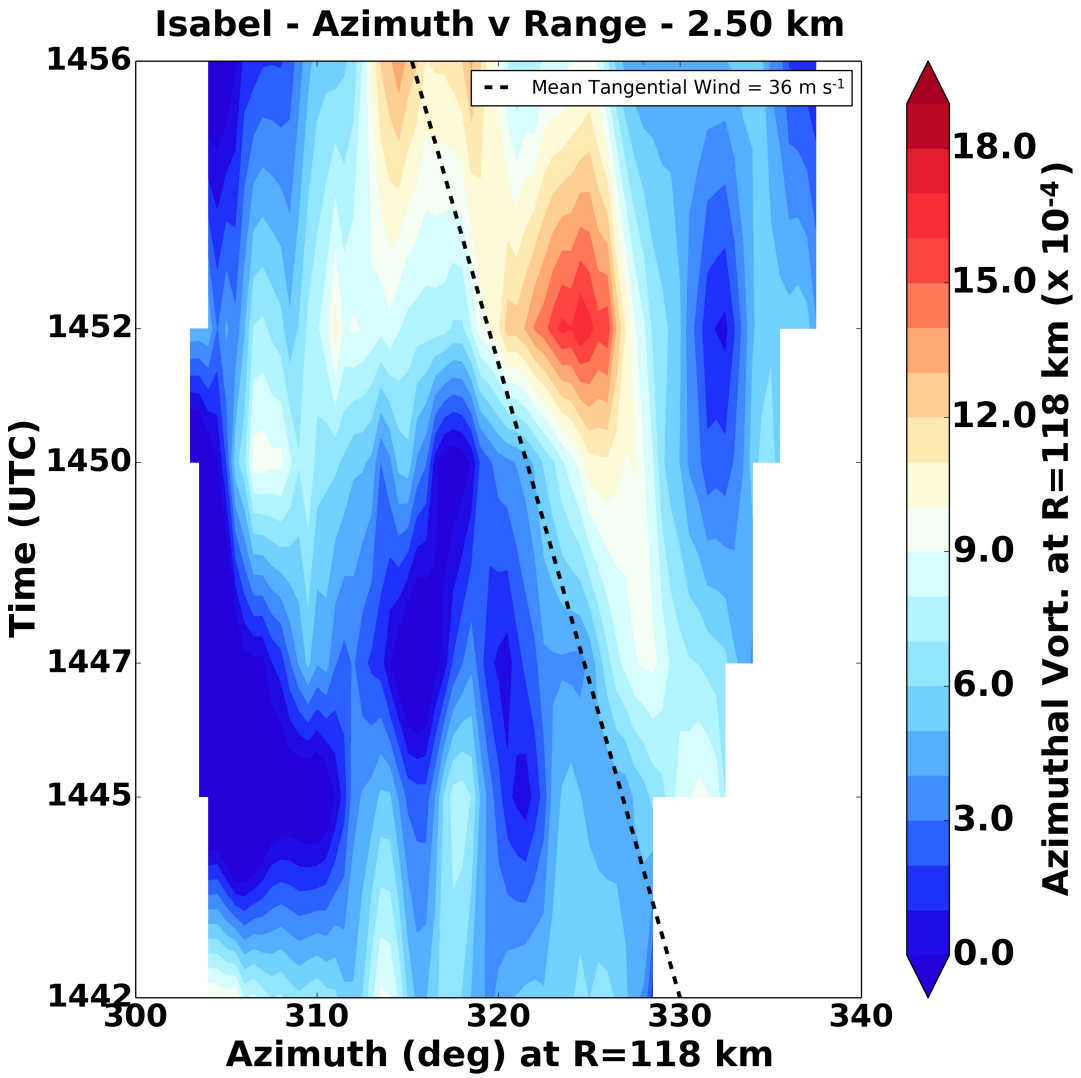


Fig. 16. Shown is an azimuth-time plot of vertical vorticity at a radius of 118 km from the center of Hurricane Isabel. The filled contours represent the azimuthal vorticity averaged over a 5 km radial window. The dashed line is the mean tangential wind of 36 m s^{-1} at the 118 km radius. The tangential wind is derived from the radial composite tangential winds generated from the DDAs performed in the inner core.

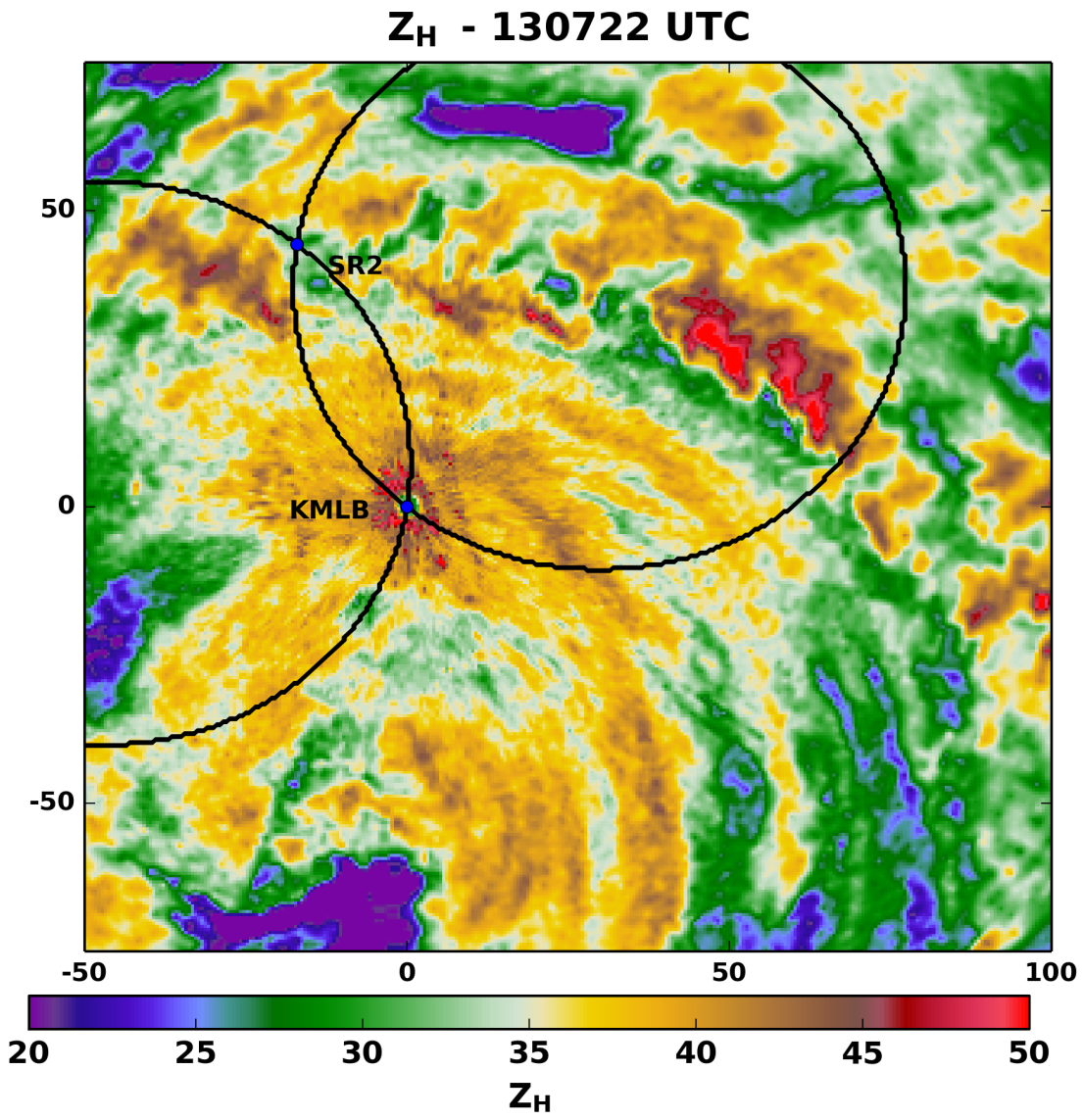


Fig. 17. As in Fig. 5, but for the inner core of Hurricane Frances with KMLB at the center of the domain.

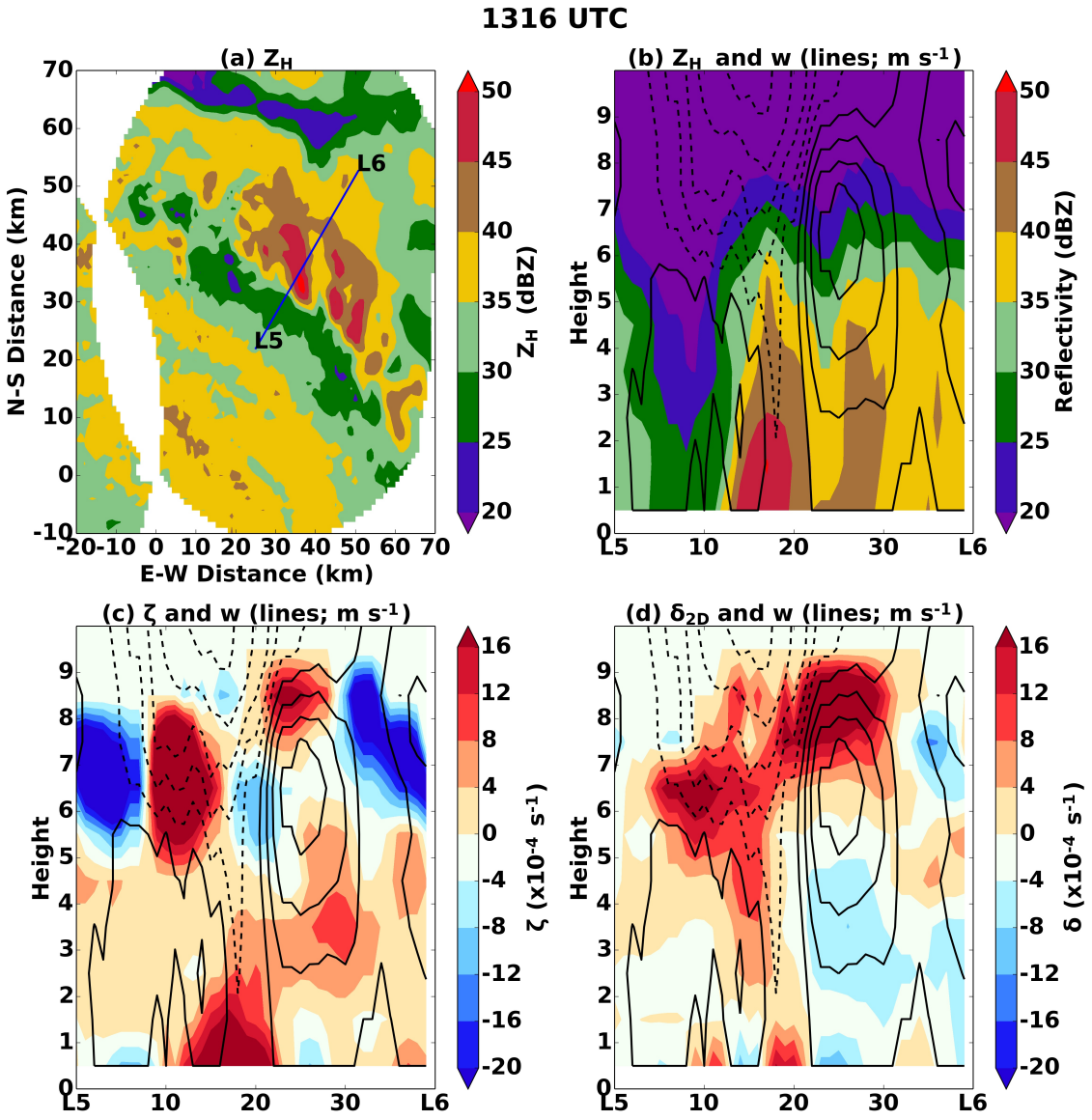


Fig. 18. As in Fig. 13, but for 1316 UTC analysis of Hurricane Frances through the line L5-L6.

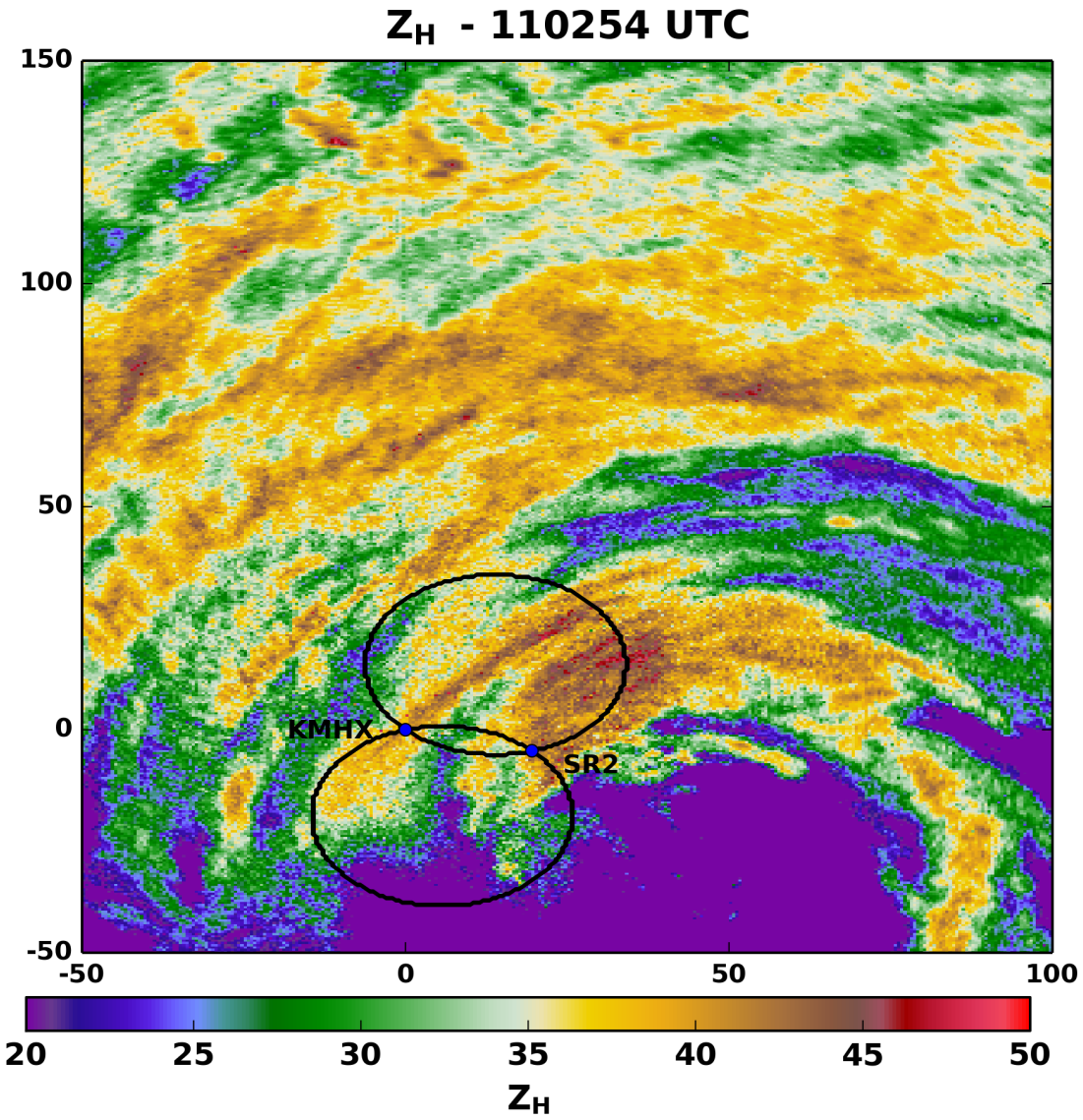


Fig. 19. As in Fig. 5, but for the landfall of Hurricane Irene. The center of the domain is KMHX.

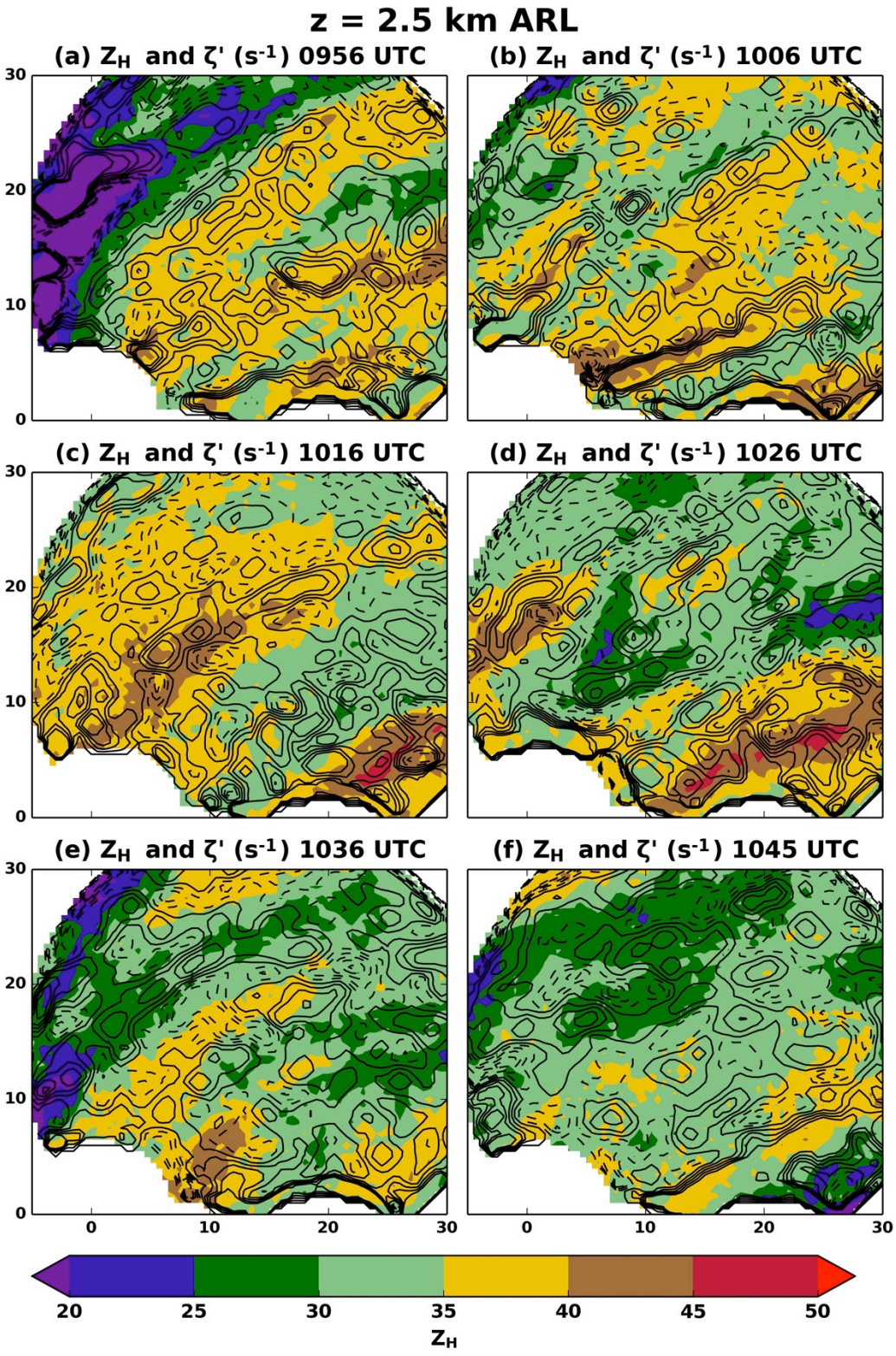


Fig. 20. As in Fig. 10, but for the 0936-1045 UTC DDAs in Hurricane Irene.

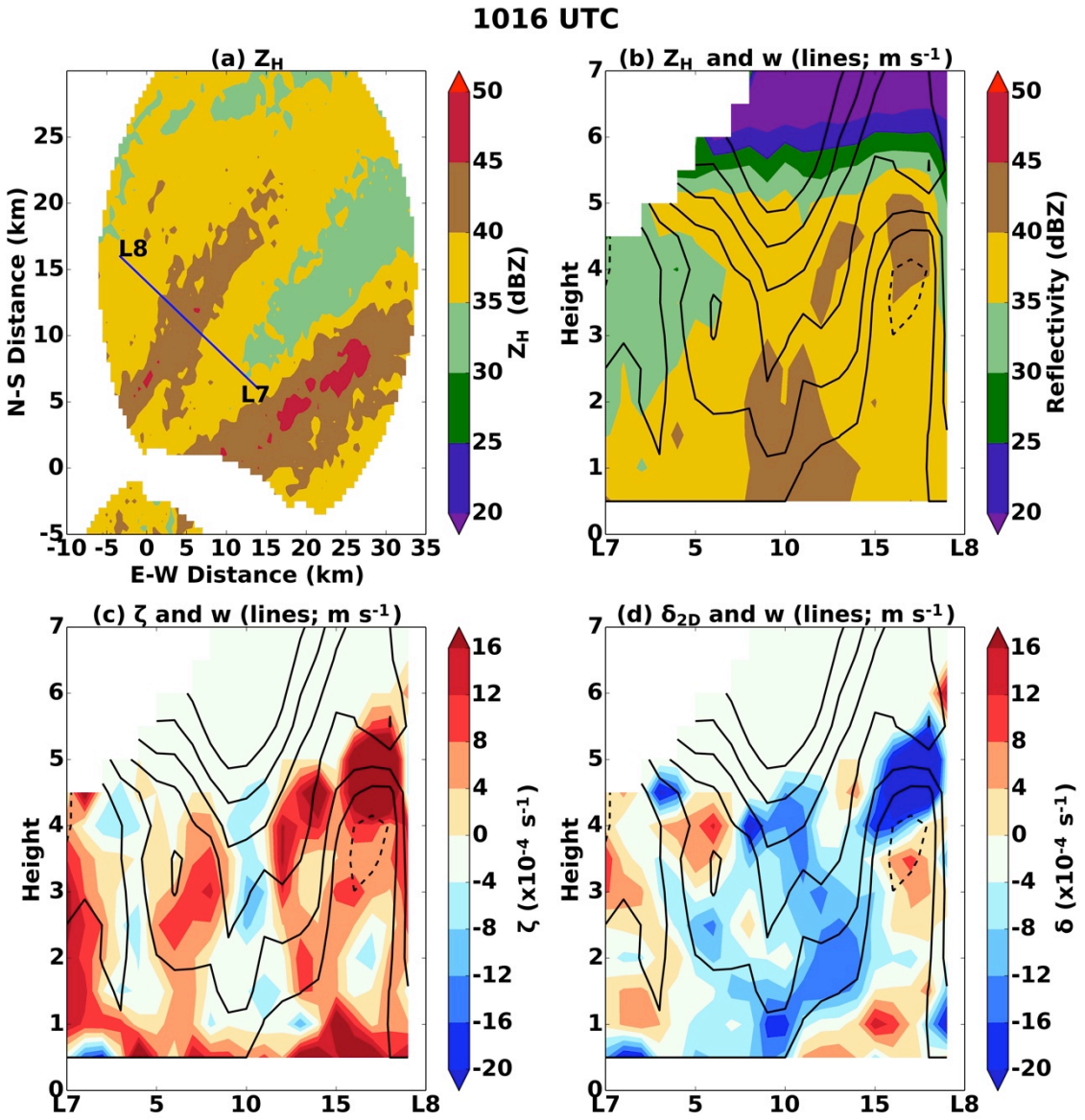


Fig. 21. As in Fig. 13, but for the 1016 UTC DDA in Hurricane Irene.

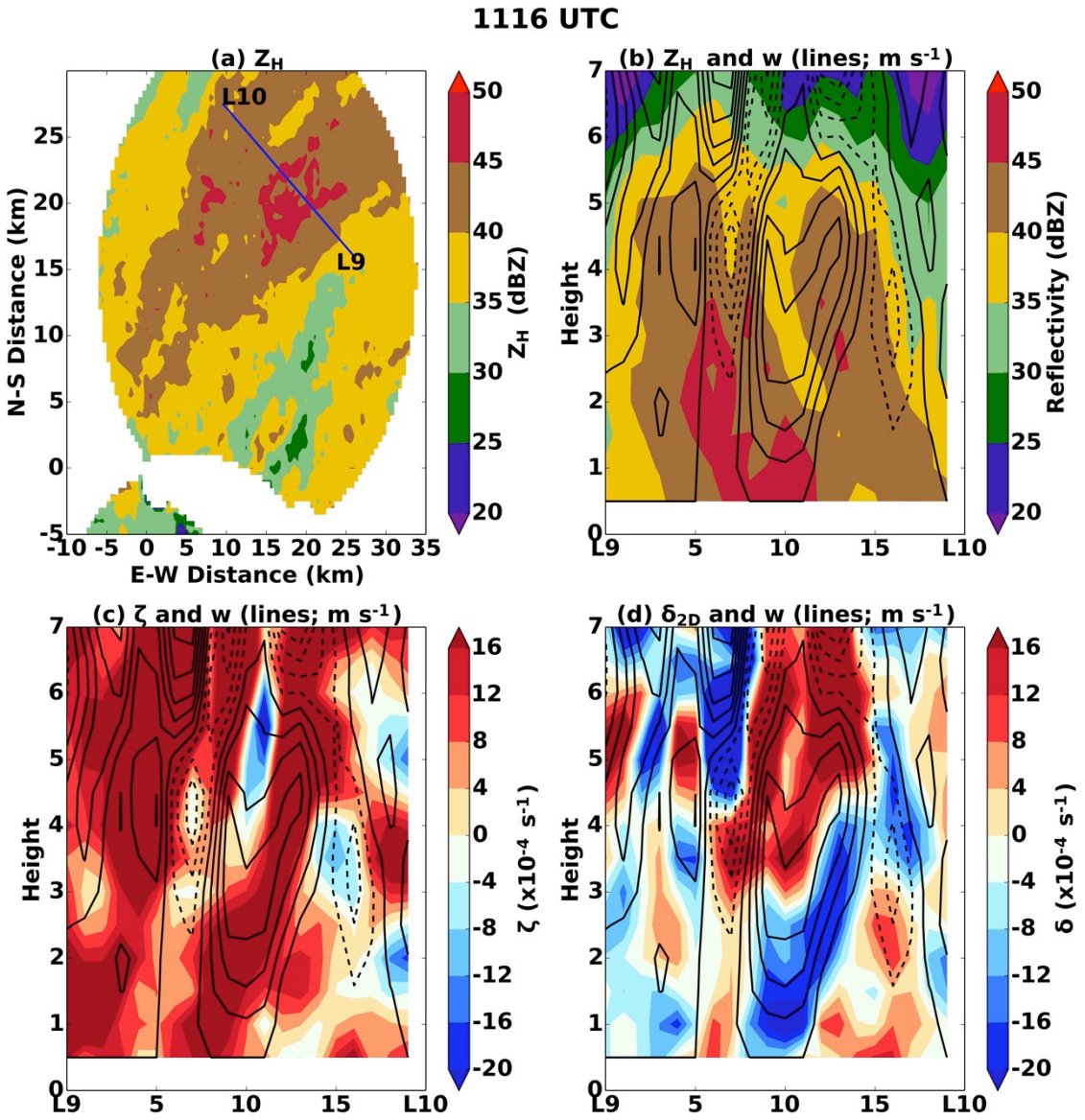


Fig. 22. As in Fig. 13, but for 1116 UTC analysis of Hurricane Irene through the line L9-L10.

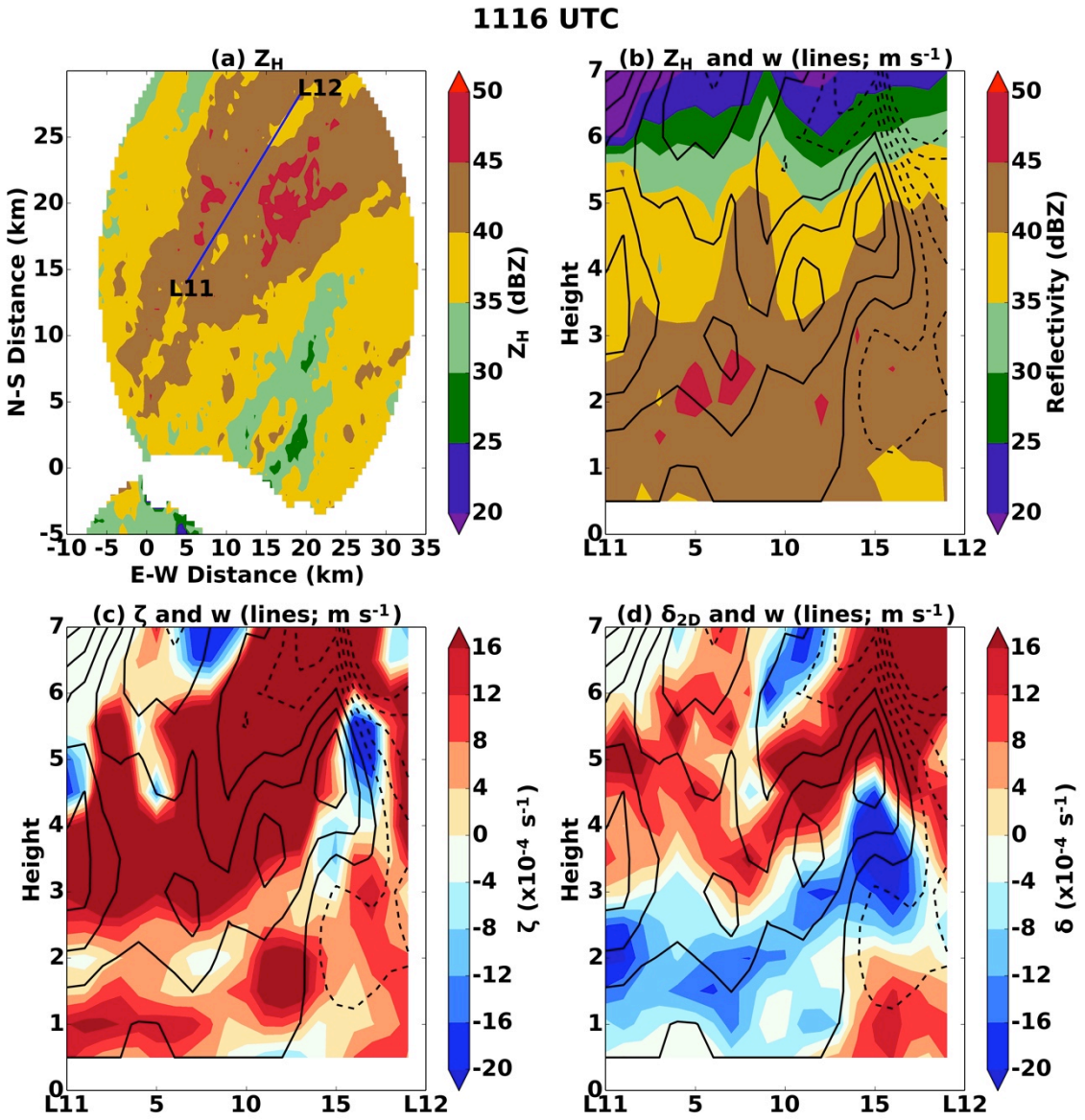


Fig. 23. As in Fig. 13, but for 1116 UTC analysis of Hurricane Irene through the line L11-L12.

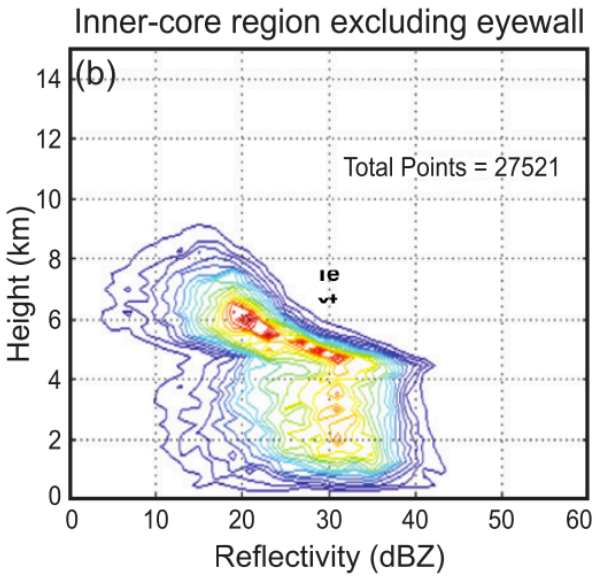


Fig. 24. CFAD courtesy of Houze (2010; see his Fig. 32b).

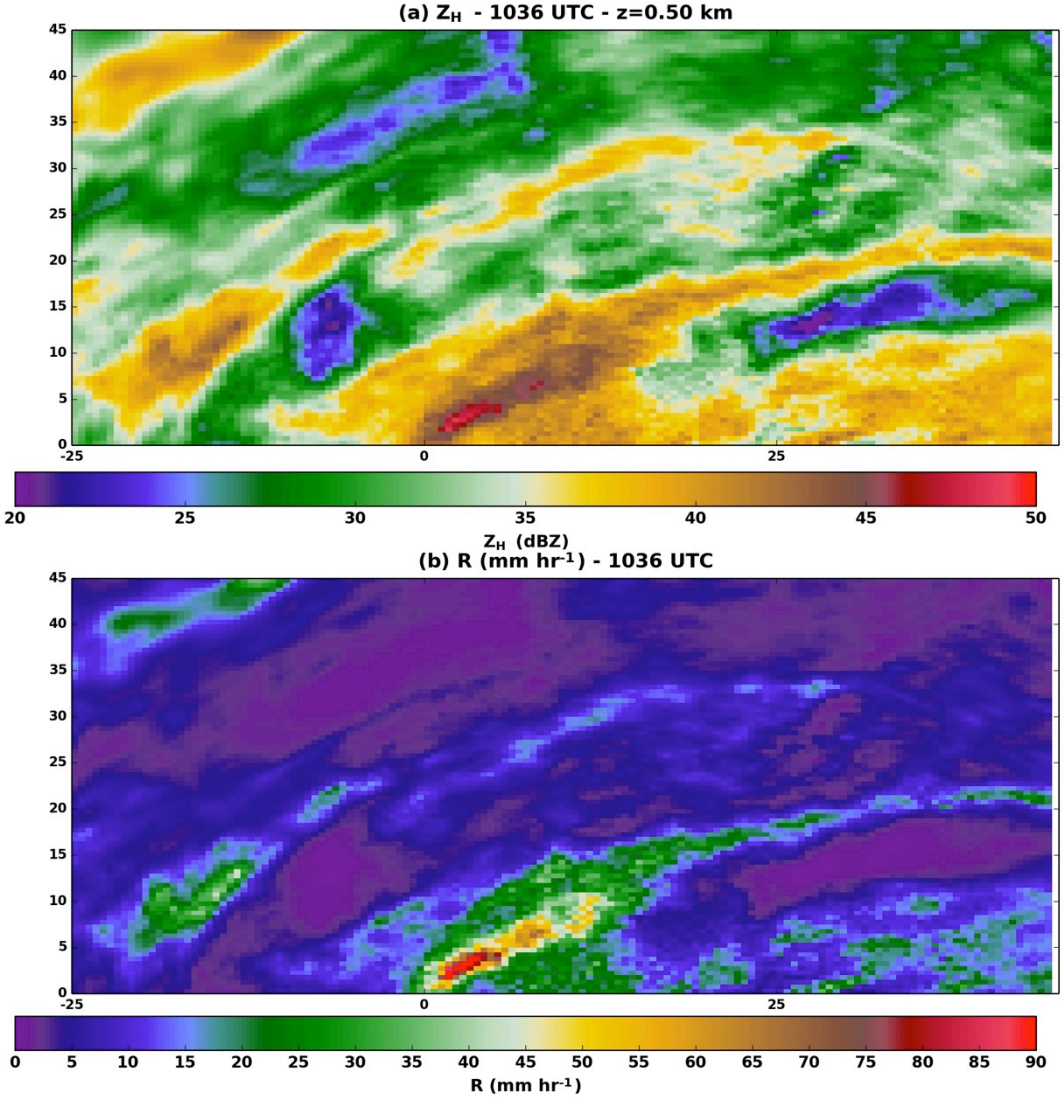


Fig. 25. (a) Radar reflecitivity from SMART radar 2 is gridded in dBZ at 1036 UTC during Hurricane Irene at z=0.5 km. (b) Rain rate (mm hr^{-1}) is derived using a Z-R relation of $Z_h = 250R^{1.2}$.

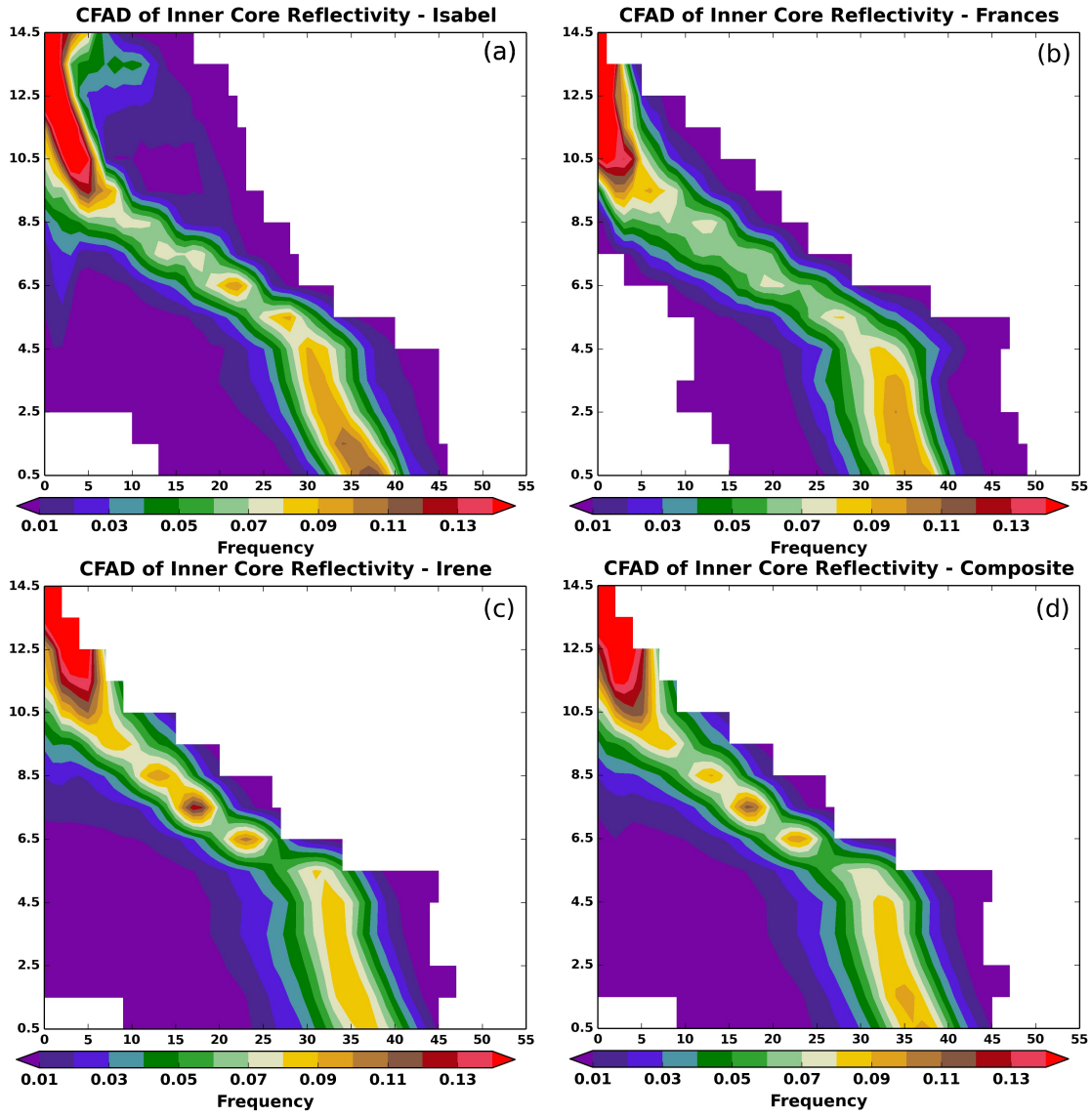


Fig. 26. Contoured frequency altitude diagrams for (a) Hurricane Isabel, (b) Hurricane Frances, (c) Hurricane Irene, and (d) a composite of all three cases. The filled contours represent the frequency of data per reflectivity bin (1 dBZ) per kilometer. So, the frequency can be read as 0.01 (or 1%) dBZ^{-1} km^{-1}.

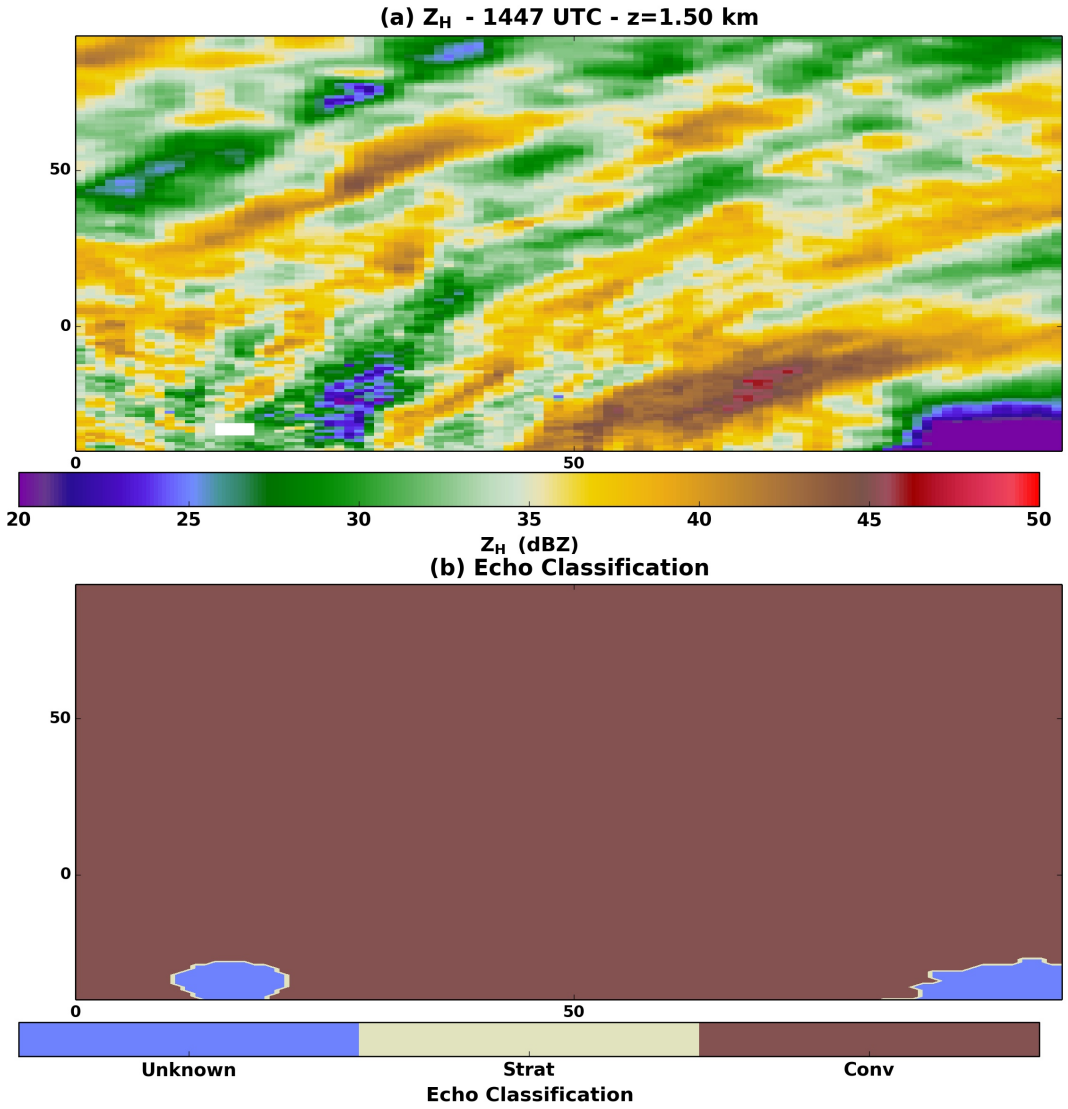


Fig. 27. Results of the stratiform-convective classification algorithm in the inner core of Hurricane Isabel at 1447 UTC. (a) Z_H is displayed at the 1.50 km altitude. (b) The echo classification is displayed with brown conveying convective echoes, tan showing stratiform echoes, and blue indicating an unknown classification.

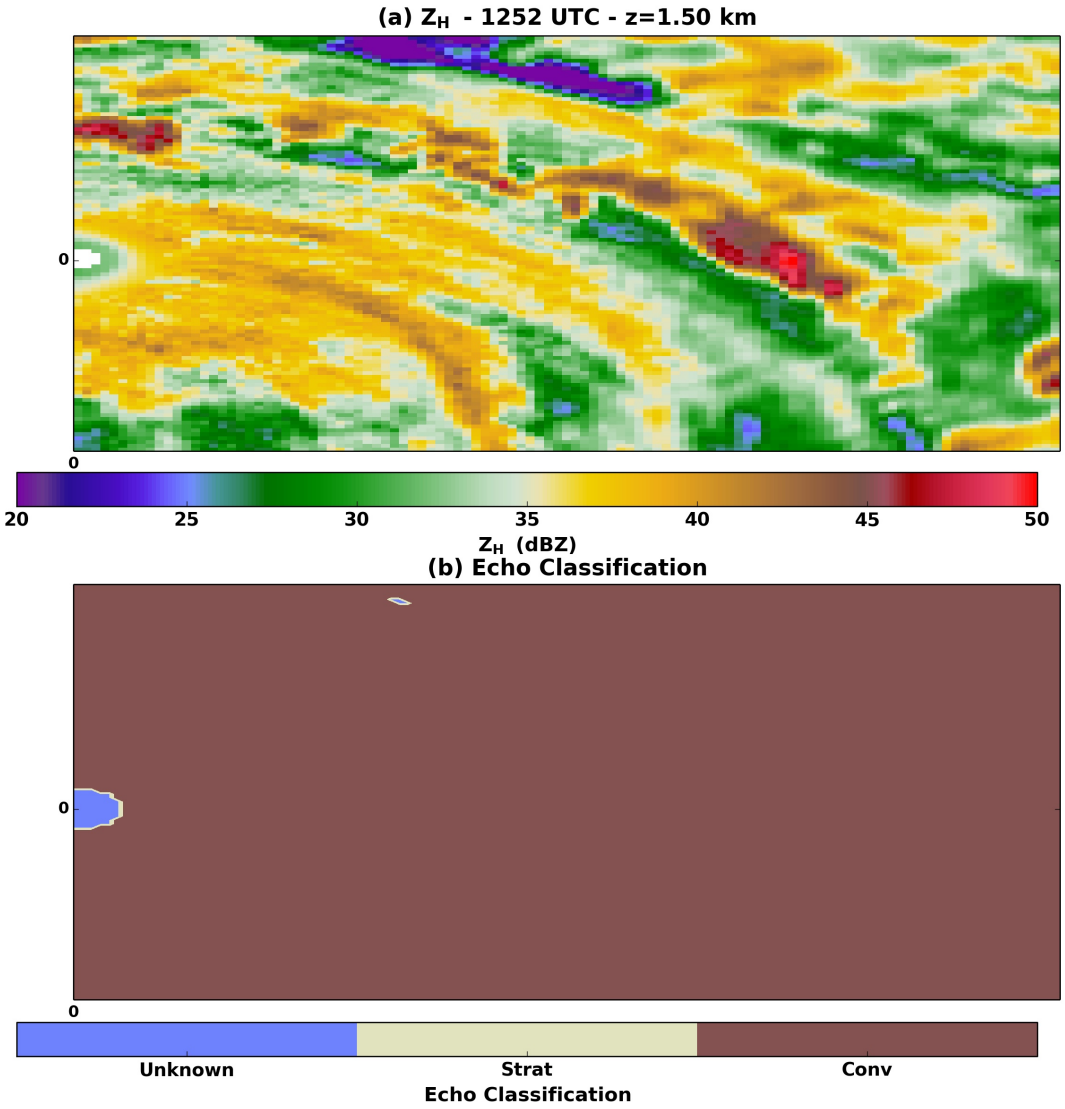


Fig. 28. As in Fig. 27, but for the 1252 UTC analysis of Hurricane Frances.

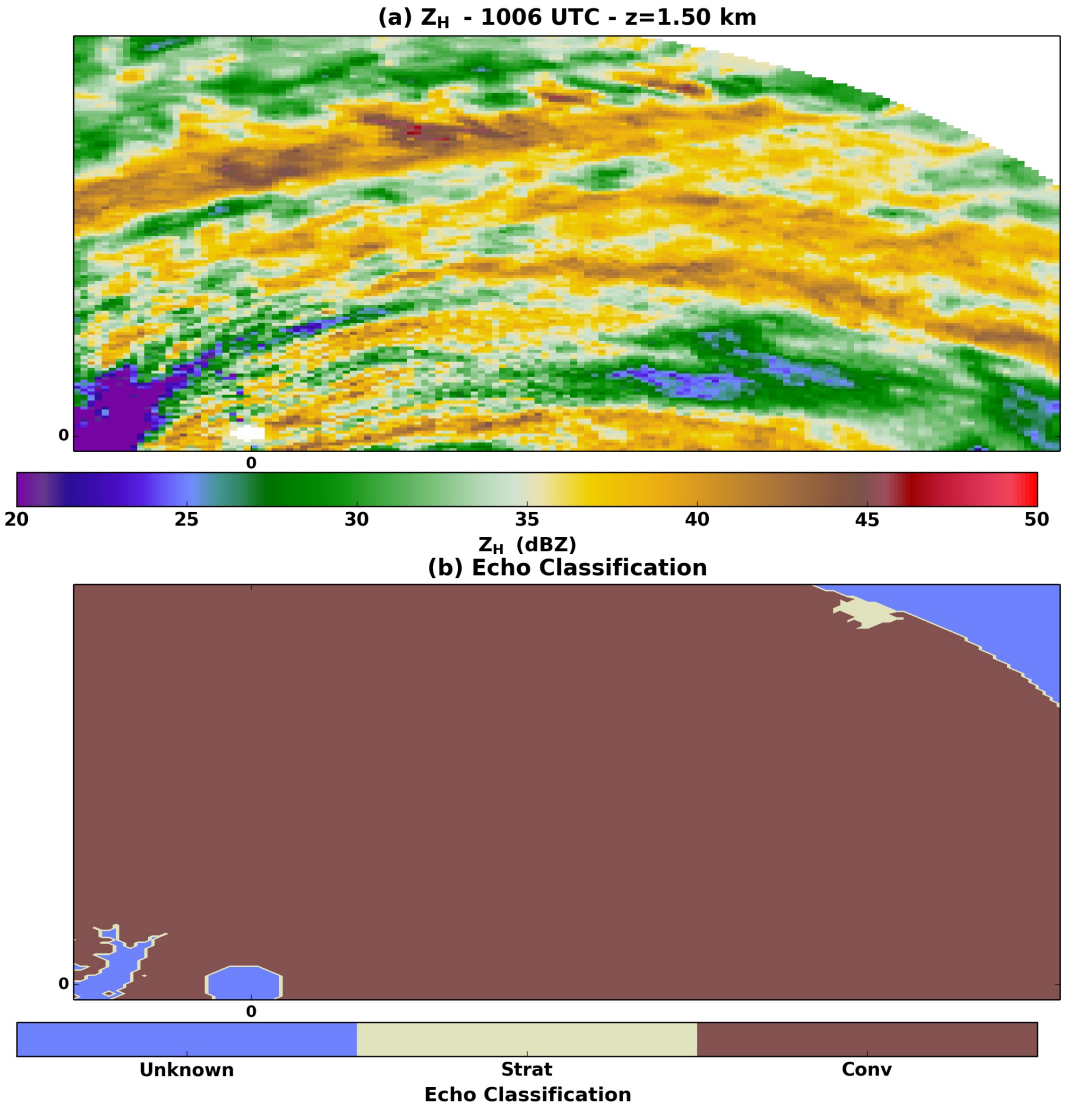


Fig. 29. As in Fig. 27, but for the 1006 UTC analysis of Hurricane Irene.

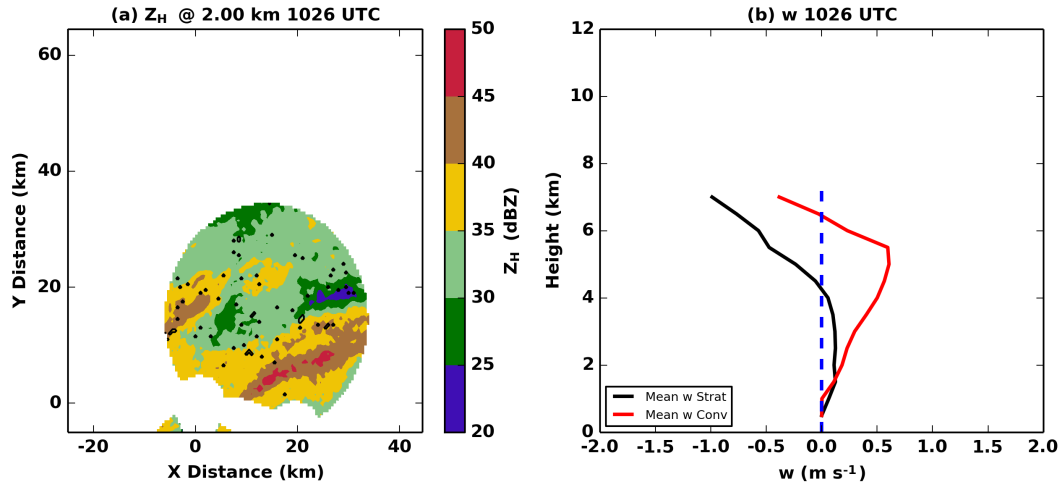


Fig. 30. An example of the vertical profile of vertical velocity in convective and non-convective echoes prior to the reclassification of the inner core to all convective echoes is shown for the 1026 UTC DDA of Hurricane Irene. (a) Z_H is contoured and filled in 5 dBZ increments and the echoes that were classified as stratiform are contoured in black. (b) The mean vertical velocity of convective and stratiform (i.e. non-convective) echoes is shown.

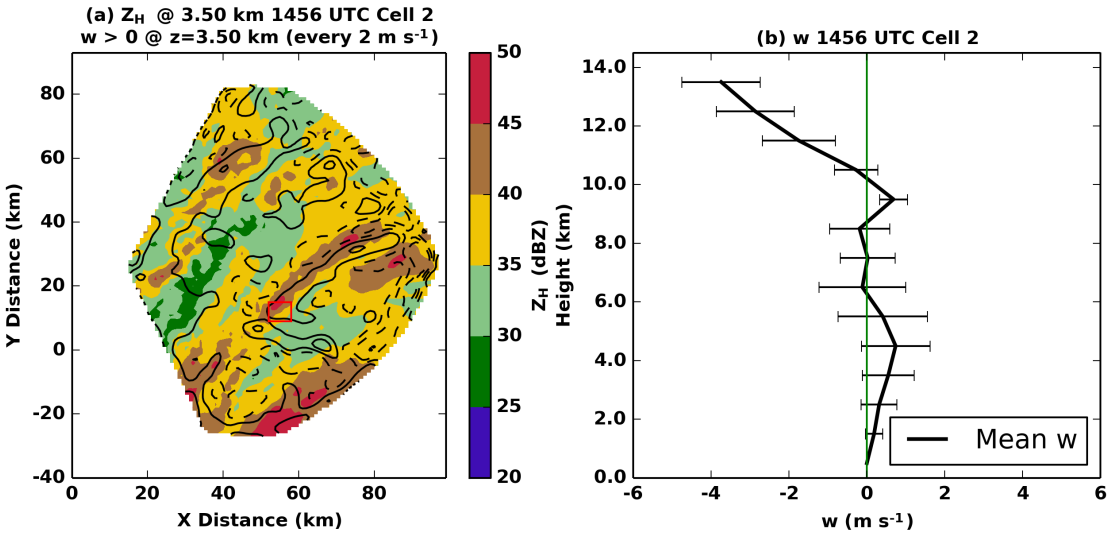


Fig. 31. Shown is a vertical velocity profile taken within a rainband [in red box in (a)] in the DDA at 1456 UTC in Hurricane Isabel. (a) Reflectivity is shaded every 5 dBZ with vertical velocity contoured every 2 m s^{-1}. The red box shows the area in which the vertical velocity statistics are calculated (b). (b) Mean vertical velocity is shown in the black line with height (y-axis) with one standard deviation indicated by the error bars. The green line indicates 0 m s^{-1}.

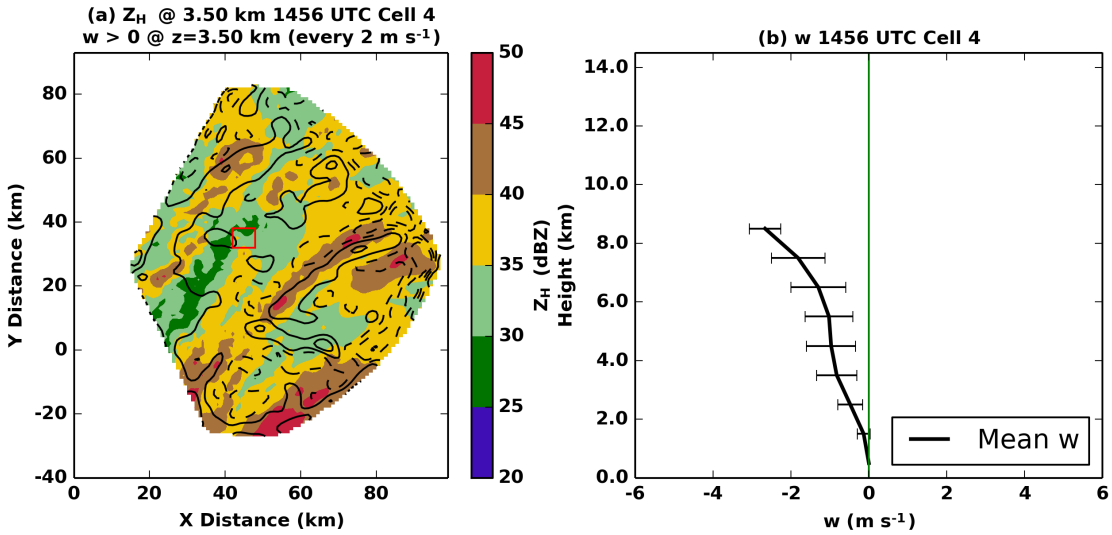


Fig. 32. As in Fig. 31, but for a non-rainband region of the 1456 UTC analysis. The red box in (a) indicates region over which the statistics in (b) are calculated.

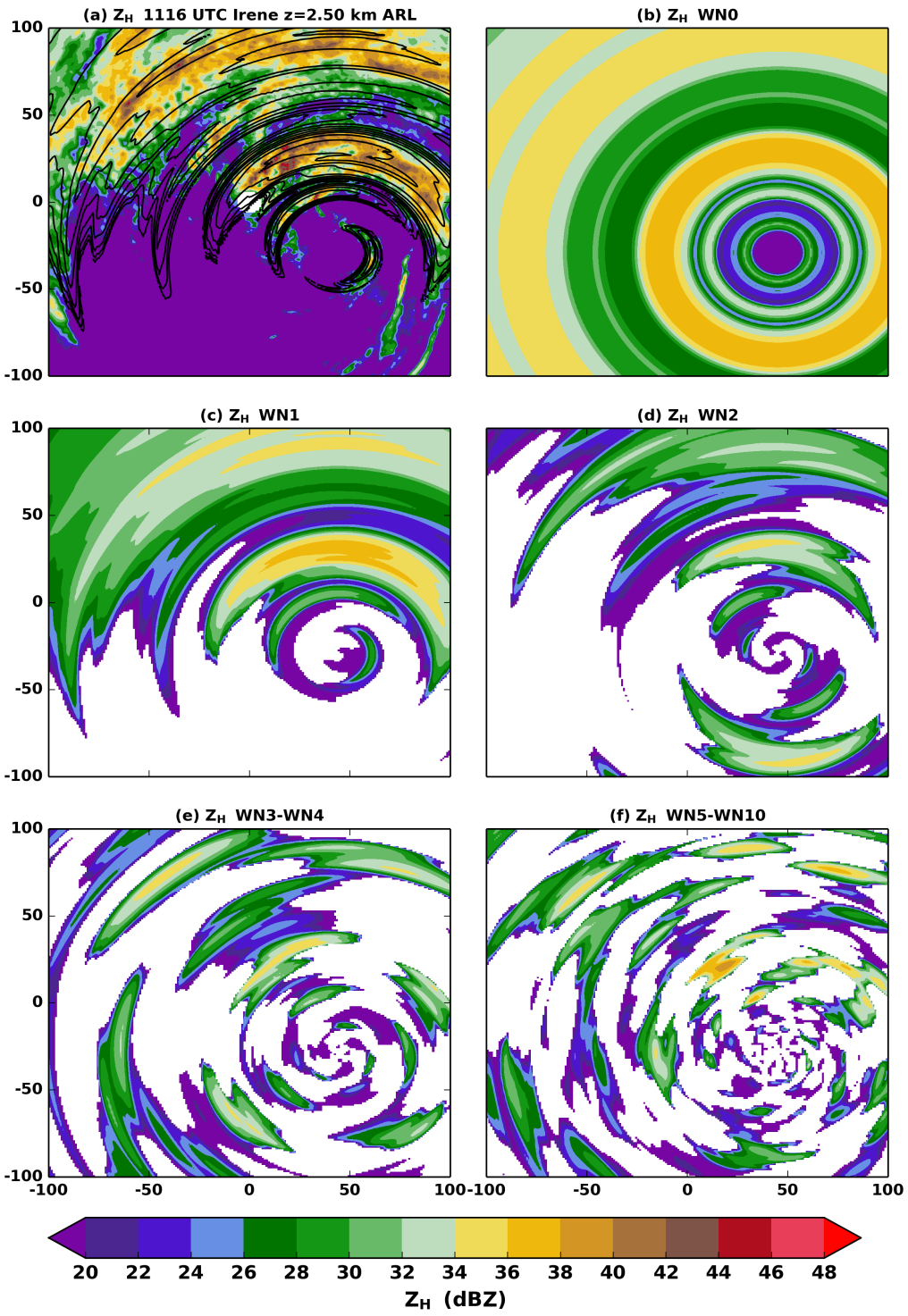


Fig. 33. As in Fig. 8, but (c) is WN1 only, (d) is WN2 only, (e) is WN3-WN4, and (f) is WN5-WN10.

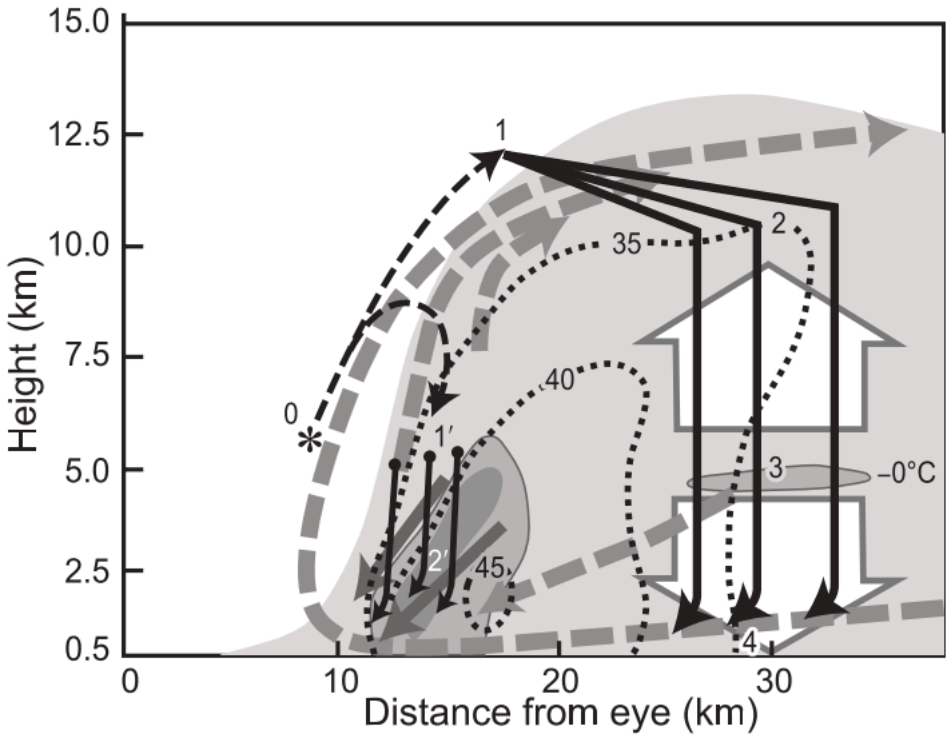


Fig. 34. Fig. 9 of (Marks and Houze 1987), showing a conceptual model the inner core stratiform structure of a mature TC.

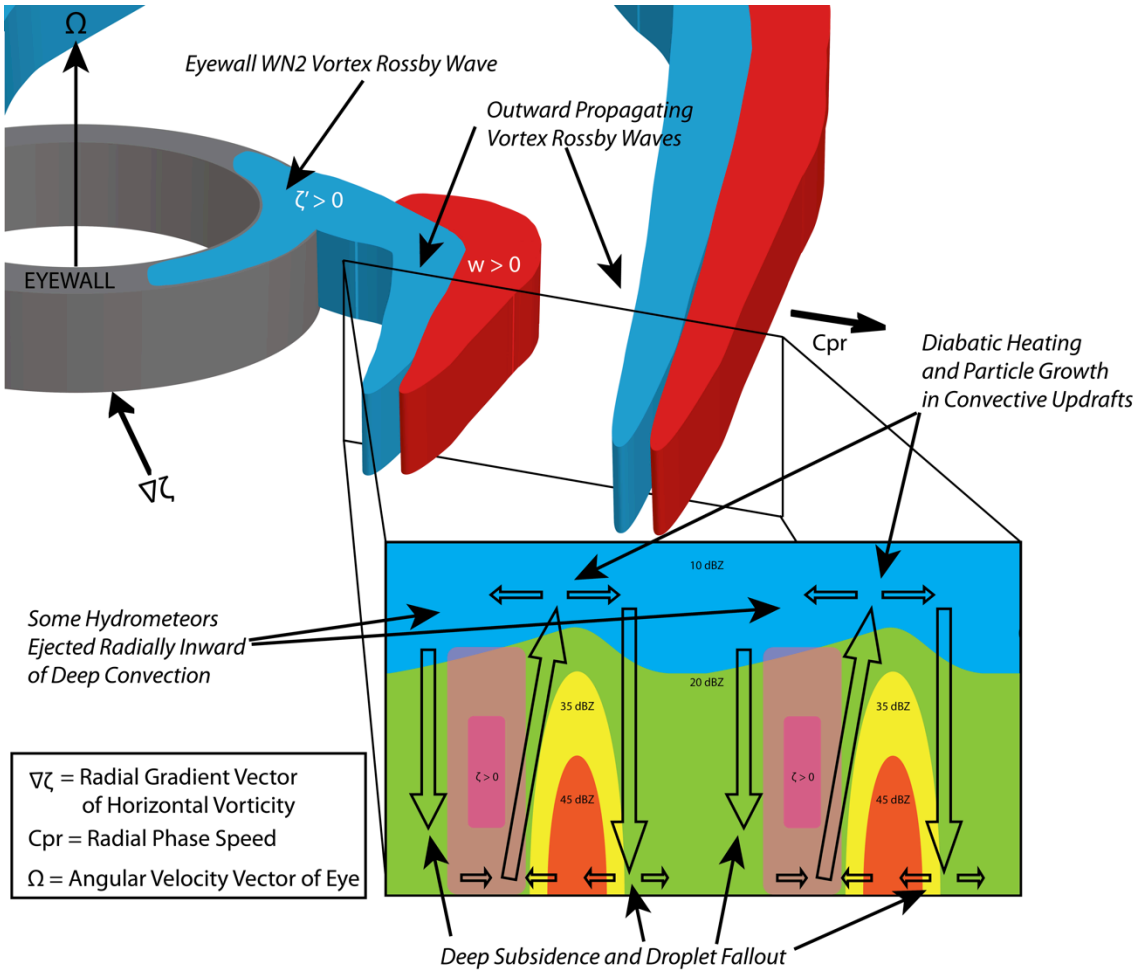


Fig. 35. A conceptual model of the inner core of a TC generated from observations presented herein. The dark grey annulus represents the eyewall, the blue structures represent VRWs beginning in the eyewall, extending radially outward into the inner core, and the red structures are the rising motion associated with the VRW. In the cross section through the VRW, radar reflectivity is shaded at intervals of 10 dBZ (blue), 20 dBZ (green), 35 dBZ (yellow), and 45 dBZ (orange). The VRWs are represented by the pink, translucent shading. The hollow black arrows show the rainband-relative flow. In addition, likely hydrometeor paths are indicated, showing the generation of particles in the convective updrafts and droplet fallout in the deep subsidence between the rainbands.

References

Abdullah, A. J., 1966: The Spiral Bands of a Hurricane: A Possible Dynamic Explanation. *J. Atmos. Sci.*, **23**, 367–375.

Anthes, R., 1972: Development of Asymmetries in a Three-Dimensional Numerical Model of the Tropical Cyclone 1. *Mon. Weather Rev.*, 461–476. http://journals.ametsoc.org/doi/abs/10.1175/1520-0493(1972)100<0461:DOAIAT>2.3.CO;2\nhttp://journals.ametsoc.org/doi/abs/10.1175/1520-0442(2001)014<4073:IVOTAS>2.0.CO;2.

Avila, L. A., and J. Cangialosi, 2012: *Tropical Cyclone Report: Hurricane Irene (AL092011)*. 45 pp. http://www.nhc.noaa.gov/data/tcr/AL092011_Irene.pdf.

Beven, J. L., 2004: *Tropical Cyclone Report: Hurricane Frances*. 30 pp. http://www.nhc.noaa.gov/data/tcr/AL062004_Frances.pdf.

——, and H. Cobb, 2003: *Tropical Cyclone Report: Hurricane Isabel*. 30 pp. http://www.nhc.noaa.gov/data/tcr/AL132003_Isabel.pdf.

Biggerstaff, M. I., and R. A. Houze, 1991: Midlevel Vorticity Structure of the 10–11 June 1985 Squall Line. *Mon. Weather Rev.*, **119**, 3066–3079, doi:10.1175/1520-0493(1991)119<3066:MVSOTJ>2.0.CO;2.

——, and S. A. Listemaa, 2000: An improved scheme for convective/stratiform echo classification using radar reflectivity. *J. Appl. Meteorol.*, **39**, 2129–2150, doi:10.1175/1520-0450(2001)040<2129:AISFCS>2.0.CO;2.

——, and Coauthors, 2005: The Shared Mobile Atmospheric Research and Teaching Radar: A Collaboration to Enhance Research and Teaching. *Bull. Am. Meteorol. Soc.*, **86**, 1263–1274, doi:10.1175/BAMS-86-9-1263.

http://journals.ametsoc.org/doi/abs/10.1175/BAMS-86-9-1263.

Böhm, H. P., 1989: A General Equation for the Terminal Fall Speed of Solid Hydrometeors. *J. Atmos. Sci.*, **46**, 2419–2427, doi:10.1175/1520-0469(1989)046<2419:AGEFTT>2.0.CO;2. http://journals.ametsoc.org/doi/abs/10.1175/1520-0469(1989)046<2419:AGEFTT>2.0.CO;2.

Braun, S. A., and R. A. Houze, 1994: The Transition Zone and Secondary Maximum of Radar Reflectivity behind a Midlatitude Squall Line: Results Retrieved from Doppler Radar Data. *J. Atmos. Sci.*, **51**, 2733–2755, doi:10.1175/1520-0469(1994)051<2733:TTZASM>2.0.CO;2. http://journals.ametsoc.org/doi/abs/10.1175/1520-0469(1994)051<2733:TTZASM>2.0.CO;2.

——, M. T. Montgomery, and Z. Pu, 2006: High-Resolution Simulation of Hurricane Bonnie (1998). Part I: The Organization of Eyewall Vertical Motion. *J. Atmos. Sci.*, **63**, 19–42, doi:10.1175/JAS3598.1. http://dx.doi.org/10.1175/JAS3598.1.

Carr, L. E., and R. T. Williams, 1989: Barotropic Vortex Stability to Perturbations from Axisymmetry. *J. Atmos. Sci.*, **46**, 3177–3191, doi:10.1175/1520-0469(1989)046<3177:BVSTPF>2.0.CO;2.

Cavallo, S. M., R. D. Torn, C. Snyder, C. Davis, W. Wang, and J. Done, 2012: Evaluation of the Advanced Hurricane WRF data assimilation system for the 2009 Atlantic hurricane season. *Mon. Weather Rev.*, 121017144007007, doi:10.1175/MWR-D-12-00139.1.

Chen, Y., and M. K. Yau, 2001: Spiral Bands in a Simulated Hurricane. Part I: Vortex

Rossby Wave Verification. *J. Atmos. Sci.*, **58**, 2128–2145, doi:10.1175/1520-0469(2001)058<2128:SBIASH>2.0.CO;2.

Chow, K. C., K. L. Chan, and A. K. H. Lau, 2002: Generation of Moving Spiral Bands in Tropical Cyclones. *J. Atmos. Sci.*, **59**, 2930–2950, doi:10.1175/1520-0469(2002)059<2930:GOMSBI>2.0.CO;2. \\IBSERVER\ID_enl\Journal_of_the_Atmospheric_Sciences\2002\059-20-2930.pdf.

Collins, S., K. North, and S. E. Giangrande, 2012: PyART: The Python ARM Radar Toolkit. Second Symposium on Advances in Modeling and Analysis Using Python, New Orleans, LA, Amer. Meteor. Soc., S2.2.

Corbosiero, K. L., and J. Molinari, 2002: The Effects of Vertical Wind Shear on the Distribution of Convection in Tropical Cyclones. *Mon. Weather Rev.*, **130**, 2110–2123, doi:10.1175/1520-0493(2002)130<2110:TEOVWS>2.0.CO;2. http://journals.ametsoc.org/doi/abs/10.1175/1520-0493(2002)130<2110:TEOVWS>2.0.CO;2.

——, ——, A. R. Aiyyer, and M. L. Black, 2006: The Structure and Evolution of Hurricane Elena (1985). Part II: Convective Asymmetries and Evidence for Vortex Rossby Waves. *Mon. Weather Rev.*, **134**, 3073–3091, doi:10.1175/MWR3250.1.

Crum, T. D., and R. L. Alberty, 1993: The WSR-88D and the WSR-88D Operational Support Facility. *Bull. Am. Meteorol. Soc.*, **74**, 1669–1687, doi:10.1175/1520-0477(1993)074<1669:TWATWO>2.0.CO;2.

Curry, R. A., 2010: Dual-Doppler analysis of Hurricane Isabel (2003) as it made landfall. M. S. Thesis, School of Meteorology, University of Oklahoma, 80 pp.

Didlake, A. C., and R. A. Houze, 2013a: Convective-Scale Variations in the Inner-Core Rainbands of a Tropical Cyclone. *J. Atmos. Sci.*, **70**, 504–523, doi:10.1175/JAS-D-12-0134.1. http://journals.ametsoc.org/doi/abs/10.1175/JAS-D-12-0134.1.

——, and R. a. Houze, 2013b: Dynamics of the Stratiform Sector of a Tropical Cyclone Rainband. *J. Atmos. Sci.*, **70**, 1891–1911, doi:10.1175/JAS-D-12-0245.1. http://journals.ametsoc.org/doi/abs/10.1175/JAS-D-12-0245.1.

Doviak, R. J., V. Bringi, a. Ryzhkov, a. Zahrai, and D. Zrnić, 2000: Considerations for polarimetric upgrades to operational WSR-88D radars. *J. Atmos. Ocean. Technol.*, **17**, 257–278, doi:10.1175/1520-0426(2000)017<0257:CFPUTO>2.0.CO;2.

Franklin, C. N., G. J. Holland, and P. T. May, 2006: Mechanisms for the generation of mesoscale vorticity features in tropical cyclone rainbands. *Mon. Weather Rev.*, **134**, 2649–2669, doi:10.1175/MWR3222.1. <Go to ISI>://000241361900001.

Guinn, T. A., and W. H. Schubert, 1993: Hurricane Spiral Bands. *J. Atmos. Sci.*, **50**, 3380–3403.

Hall, J. D., M. Xue, L. Ran, and L. M. Leslie, 2013: High-Resolution Modeling of Typhoon Morakot (2009): Vortex Rossby Waves and Their Role in Extreme Precipitation over Taiwan. *J. Atmos. Sci.*, **70**, 163–186, doi:10.1175/JAS-D-11-0338.1.

Halverson, J. B., J. Simpson, G. Heymsfield, H. Pierce, T. Hock, and L. Ritchie, 2006: Warm Core Structure of Hurricane Erin Diagnosed from High Altitude Dropsondes during CAMEX-4. *J. Atmos. Sci.*, **63**, 309–324, doi:10.1175/JAS3596.1. http://journals.ametsoc.org/doi/abs/10.1175/JAS3596.1.

Hirth, B. D., J. L. Schroeder, C. C. Weiss, D. a. Smith, and M. I. Biggerstaff, 2012:

Research Radar Analyses of the Internal Boundary Layer over Cape Canaveral, Florida, during the Landfall of Hurricane Frances (2004). *Weather Forecast.*, **27**, 1349–1372, doi:10.1175/WAF-D-12-00014.1. http://journals.ametsoc.org/doi/abs/10.1175/WAF-D-12-00014.1.

Hogsett, W., and D.-L. Zhang, 2009: Numerical Simulation of Hurricane Bonnie (1998). Part III: Energetics. *J. Atmos. Sci.*, **66**, 2678–2696, doi:10.1175/2009JAS3087.1.

Houze, R. A., 2010: Clouds in Tropical Cyclones. *Mon. Weather Rev.*, **138**, 293–344, doi:10.1175/2009MWR2989.1. http://journals.ametsoc.org/doi/abs/10.1175/2009MWR2989.1.

Jones, S. C., 1995: The evolution of vortices in vertical shear. I: Initially barotropic vortices. *Quart. J. Roy. Meteor. Soc.*, **121**, 821–851, doi:10.1002/qj.49712152406. http://dx.doi.org/10.1002/qj.49712152406.

Knupp, K. R., J. Walters, and M. Biggerstaff, 2006: Doppler Profiler and Radar Observations of Boundary Layer Variability during the Landfall of Tropical Storm Gabrielle. *J. Atmos. Sci.*, **63**, 234–251, doi:10.1175/JAS3608.1. http://journals.ametsoc.org/doi/abs/10.1175/JAS3608.1.

Kummerow, C., W. Barnes, T. Kozu, J. Shiue, and J. Simpson, 1998: The Tropical Rainfall Measuring Mission (TRMM) sensor package. *J. Atmos. Ocean. Technol.*, **15**, 809–817, doi:10.1175/1520-0426(1998)015<0809:TTRMMT>2.0.CO;2.

Lee, W., B. Jou, P.-L. Chang, and S.-M. Deng, 1999: Tropical cyclone kinematic structure retrieved from single-Doppler radar observations. Part I: Interpretation of Doppler velocity patterns and the GBVTD technique. *Mon. Weather Rev.*, **127**,

2419–2440, doi:10.1175/1520-0493(1999)127<2419:TCKSRF>2.0.CO;2. http://journals.ametsoc.org/doi/full/10.1175/1520-0493(1999)127<2419:TCKSRF>2.0.CO;2.

——,, and F. D. Marks Jr, 2000: Tropical cyclone kinematic structure retrieved from single-Doppler radar observations. Part II: The GBVTD-simplex center finding algorithm. *Mon. Weather Rev.*, **128**, 1925–1936, doi:10.1175/1520-0493(2000)128<1925:TCKSRF>2.0.CO;2. http://journals.ametsoc.org/doi/abs/10.1175/1520-0493(2000)128<1925:TCKSRF>2.0.CO;2\nhttp://journals.ametsoc.org/doi/pdf/10.1175/1520-0493(2000)128<1925:TCKSRF>2.0.CO;2.

Li, Q., and Y. Wang, 2012: A Comparison of Inner and Outer Spiral Rainbands in a Numerically Simulated Tropical Cyclone. *Mon. Weather Rev.*, **140**, 2782–2805, doi:10.1175/MWR-D-11-00237.1.

——, 2016: Outer rainband formation in a sheared tropical cyclone. 32nd Conf. on Hurricanes and Trop. Meteor., Amer. Meteor. Soc., 13B.3.

MacDonald, N. J., 1968: The evidence for the existence of Rossby-like waves in the hurricane vortex. *Tellus*, **20**, 138–150, doi:10.1111/j.2153-3490.1968.tb00358.x.

Marks, F. D., and R. A. Houze, 1987: Inner Core Structure of Hurricane Alicia from Airborne Doppler Radar Observations. *J. Atmos. Sci.*, **44**, 1296–1317, doi:10.1175/1520-0469(1987)044<1296:ICSOHA>2.0.CO;2. http://journals.ametsoc.org/doi/abs/10.1175/1520-0469(1987)044<1296:ICSOHA>2.0.CO;2.

McWilliams, J. C., L. P. Graves, and M. T. Montgomery, 2003: A Formal Theory for

Vortex Rossby Waves and Vortex Evolution. *Geophys. Astrophys. Fluid Dyn.*, **97**, 275–309, doi:10.1080/0309192031000108698.

Menelaou, K., and M. K. Yau, 2014: On the role of asymmetric convective bursts to the problem of hurricane intensification. Radiation of vortex Rossby waves and wave-mean flow interactions. *J. Atmos. Sci.*, 140212115924008, doi:10.1175/JAS-D-13-0343.1. http://journals.ametsoc.org/doi/abs/10.1175/JAS-D-13-0343.1.

Montgomery, M. T., and R. J. Kallenbach, 1997: A theory for vortex Rossby-waves and its application to spiral bands and intensity changes in hurricanes. *Quart. J. Roy. Meteor. Soc.*, **123**, 435–465, doi:10.1002/qj.49712353810. http://dx.doi.org/10.1002/qj.49712353810.

——, and R. K. Smith, 2016: Recent developments in the fluid dynamics of tropical cyclones. 1–23.

Moon, Y., and D. S. Nolan, 2010: Do Gravity Waves Transport Angular Momentum away from Tropical Cyclones? *J. Atmos. Sci.*, **67**, 117–135, doi:10.1175/2009JAS3088.1.

——, and ——, 2015: Spiral Rainbands in a Numerical Simulation of Hurricane Bill (2009). Part II: Propagation of Inner Rainbands. *J. Atmos. Soc.*, 141016121051006, doi:10.1175/JAS-D-14-0056.1. http://journals.ametsoc.org/doi/abs/10.1175/JAS-D-14-0056.1.

Naftel, J. C., 2009: *NASA Global Hawk: A New Tool for Earth Science Research*. 13 pp. http://ntrs.nasa.gov/archive/nasa/casi.ntrs.nasa.gov/20090023138.pdf.

Oye, R. C., C. Mueller, and S. Smith, 1995: Software for radar translation, visualization, editing, and interpolation. 27th Conference on Radar Meteorology,

Vail, CO, Amer. Meteor. Soc., 359–361.

Potvin, C. K., D. Betten, L. J. Wicker, K. L. Elmore, and M. I. Biggerstaff, 2012a: 3DVAR vs. traditional dual-Doppler wind retrievals of a simulated supercell thunderstorm. *Mon. Weather Rev.*, 120525114116000, doi:10.1175/MWR-D-12-00063.1.

——, L. J. Wicker, and A. Shapiro, 2012b: Assessing errors in variational Dual-Doppler wind syntheses of supercell thunderstorms observed by storm-scale mobile radars. *J. Atmos. Ocean. Technol.*, **29**, 1009–1025, doi:10.1175/JTECH-D-11-00177.1.

Rappaport, E. N., 2014: Fatalities in the United States from Atlantic Tropical Cyclones: New Data and Interpretation. *Bull. Am. Meteorol. Soc.*, **95**, 341–346, doi:10.1175/BAMS-D-12-00074.1. http://journals.ametsoc.org/doi/abs/10.1175/BAMS-D-12-00074.1.

Reasor, P. D., M. T. Montgomery, F. D. Marks, and J. F. Gamache, 2000: Low-Wavenumber Structure and Evolution of the Hurricane Inner Core Observed by Airborne Dual-Doppler Radar. *Mon. Weather Rev.*, **128**, 1653–1680, doi:10.1175/1520-0493(2000)128<1653:LWSAEO>2.0.CO;2.

Rogers, R., S. Lorsolo, P. Reasor, J. Gamache, and F. Marks, 2012: Multiscale Analysis of Tropical Cyclone Kinematic Structure from Airborne Doppler Radar Composites. *Mon. Weather Rev.*, **140**, 77–99, doi:10.1175/MWR-D-10-05075.1.

Sibson, R., 1981: Interpreting Multivariate Data, chap. A brief description of natural neighbor interpolation, 21–36. John Wiley.

Steiner, M., R. A. Houze, and S. E. Yuter, 1995: Climatological characterization of

three-dimensional storm structure from operational radar and rain guage data. *J. Appl. Meteorol.*, **34**, 1978–2007.

Wang, X., Y. Ma, and N. E. Davidson, 2012: Secondary Eyewall Formation and Eyewall Replacement Cycles in a Simulated Hurricane: Effect of the Net Radial Force in the Hurricane Boundary Layer. *J. Atmos. Sci.*, 121008093205006, doi:10.1175/JAS-D-12-017.1.

Wang, Y., 2002a: Vortex Rossby Waves in a Numerically Simulated Tropical Cyclone. Part II: The Role in Tropical Cyclone Structure and Intensity Changes*. *J. Atmos. Sci.*, **59**, 1239–1262, doi:10.1175/1520-0469(2002)059<1239:VRWIAN>2.0.CO;2.

——, 2002b: Vortex Rossby Waves in a Numerically Simulated Tropical Cyclone. Part I: Overall Structure, Potential Vorticity, and Kinetic Energy Budgets*. *J. Atmos. Sci.*, **59**, 1213–1238, doi:10.1175/1520-0469(2002)059<1239:VRWIAN>2.0.CO;2.

——, 2008: Rapid Filamentation Zone in a Numerically Simulated Tropical Cyclone*. *J. Atmos. Sci.*, **65**, 1158–1181, doi:10.1175/2007JAS2426.1.

Wei, Z., L. Han-Cheng, and D. Zhang, 2010: Mesoscale Barotropic Instability of Vortex Rossby Waves in Tropical Cyclones. *Adv. Atmos. Sci.*, **27**, 243–252, doi:10.1007/s00376-009-8183-7.1.Introduction. http://link.springer.com/article/10.1007/s00376-009-8183-7.

Willoughby, H. E., 1977: Inertia buoyancy waves in hurricanes. *J. Atmos. Sci.*, **34**, 1028–1039. http://adsabs.harvard.edu/abs/1977JAtS...34.1028W.